Full 3D Motion Control for Programmable Bevel-Tip Steerable Needles

Author Abdulhamit Donder
Submitted October 25th 2021

Supervisor Prof. Ferdinando Rodriguez y Baena

A thesis submitted in fulfilment of the requirements for the degree of Doctor of Philosophy

The Mechatronics in Medicine Laboratory,
Department of Mechanical Engineering,
Imperial College London

The Mechatronics in Medicine Laboratory,
Department of Mechanical Engineering,
Imperial College London,
South Kensington Campus,
London, SW7 2AZ - UK

Dedicated to my wife and my parents, whose support made this thesis possible.

Declaration

I hereby declare that the work presented in this thesis is my own, except where stated otherwise by reference or acknowledgement.

Chapter 1.1 and Chapter 2 are from edited versions of the articles [25] and [26]. Chapter 3.2 and Chapter 5 are from an edited version of the article [25]. Similarly, an edited version of Chapter 4 forms a part of [106]. Lastly, Chapter 6 is from an edited version of [26].

The paper [25] has been accepted to IEEE Transactions on Robotics, and [26] has been submitted to the same journal and was under review at the time of thesis submission. Lastly, [106] was under revision for the same journal.

The illustrations figure 2.1 on page 33, figure 2.2 on page 35, and figure 2.3 on page 36 are reprinted with permissions from the copyright holders as seen in the figure captions. The obtained permissions are given in Chapter 7.3.

This submission is in fulfilment of the requirements for the PhD degree at Imperial College London only. The work in this thesis has not been submitted for any other degree or professional qualification.

The formatting for this thesis is taken from the Thesis Template by R. Robinson at https://github.com/mlnotebook/thesis_template [90] with changes, such as font, page margins, and line spacing.

Copyright

Acknowledgements

I would like to thank the individuals whose kind support and help made this PhD thesis a reality and brought my research to a meaningful conclusion.

First of all, I would like to express my sincerest gratitude to my supervisor Professor Ferdinando Rodriguez y Baena, for his generous guidance, continuous personal and professional support, and motivation throughout my PhD. I could not have imagined having a better supervisor for my PhD experience. His vision, endless energy, and scientific approach have helped me to a very great extent to accomplish this task. It was a true privilege to complete my PhD under his supervision and in the Mechatronics in Medicine Lab (MiM Lab), the perfect research environment that he created.

I profusely thank all of the MiM Lab members for their support. I am grateful to Thomas Watts for sharing his theoretical and practical experience about PBNs and his valuable feedback regarding my shape sensing algorithm, as well as Stefano Galvan for teaching me critical points in coding, Enrico Franco for his valuable feedback regarding my control paper and my early work on my PhD, Riccardo Secoli for his valuable comments on my tracking algorithm and teaching me about the actuation of PBNs.

It was a privilege to be in such a motivating and supportive research environment, and I will always carry positive memories from our times together. To this end, I would also like to thank Vani Virdyawan, Eloise Matheson, Stephen Laws, Arnau Garriga Casanovas, Zejian Cui, Ayhan Aktaş, Xue Hu, Fabio Tatti, He Liu, Hadi El Daou, Marlene Pinzi, Hisham Iqbal, Sukhpreet Singh, Daniel Bautista Salinas, Shen Treratanakulchai, and Spyridon Souipas.

It has also been a true honour to pursue my PhD by witnessing the scientific enthusiasm of Professor Brian Davies, a pioneer in medical robotics, whose energy and wisdom has always

been a true inspiration and motivation.

Additionally, I would like to thank Dr Mihailo Ristic and Dr Richard Jan van Arkel for their valuable feedback in my Early-Stage Review and Late-Stage Assessment.

I gratefully acknowledge the financial support provided for my PhD work by the Ministry of National Education of the Republic of Turkey.

This work was supported by the European Union's Horizon 2020 Research and Innovation Programme under Grant 688279 (EDEN 2020).

Last but not least, I express my profound gratitude to my beloved wife, Bükre Şeyma, for providing me with constant motivation and unfailing support, to my parents, Nurhan Dönder and Yaşar Sabri Dönder, for their endless encouragement and unwavering confidence in me, and my brother, Mustafa, for his constant companionship through the process of researching and writing this thesis.

Abstract

Minimally invasive surgery has been in the focus of many researchers due to its reduced intra- and post-operative risks when compared to an equivalent open surgery approach. In the context of minimally invasive surgery, percutaneous intervention, and particularly, needle insertions, are of great importance in tumour-related therapy and diagnosis. However, needle and tissue deformation occurring during needle insertion often results in misplacement of the needles, which leads to complications, such as unsuccessful treatment and misdiagnosis. To this end, steerable needles have been proposed to compensate for placement errors by allowing curvilinear navigation. A particular type of steerable needle is the Programmable Bevel Tip Steerable Needle (PBN), which is a bio-inspired needle that consists of relatively soft and slender segments. Due to its flexibility and bevel-tip segments, it can navigate through three dimensional (3D) curvilinear paths.

In PBNs, steering in a desired direction is performed by actuating particular PBN segments. Therefore, the pose of each segment is needed to ensure that the correct segment is actuated. To this end, in this thesis, proprioceptive sensing methods for PBNs were investigated. Two novel methods, an Electromagnetic (EM)-based tip pose estimation method and a Fibre Bragg Grating (FBG)-based full shape sensing method, were presented and evaluated. The error in position was observed to be less than 1.08 mm and 5.76 mm, with the proposed EM-based tip tracking and FBG-based shape reconstruction methods, respectively.

Moreover, autonomous path-following controllers for PBNs were also investigated. A closed-loop, 3D path-following controller, which was closed via feedback from FBG-inscribed Multi-core Fibres (MCFs) embedded within the needle, was presented. The

Nonlinear Guidance Law (NLGL), which is a well-known approach for path-following control of aerial vehicles, and Active Disturbance Rejection Control (ADRC), which is known for its robustness within hard-to-model environments, were chosen as the control methods. Both linear and nonlinear ADRC were investigated, and the approaches were validated in both ex vivo brain and phantom tissue, with some of the experiments involving moving targets. The tracking error in position was observed to be less than 6.56 mm.

Contents

List of Figures

List of Tables

Acronyms

2D two dimensional. 15, 16, 36, 39, 40, 48, 49, 107, 109, 115, 130, 134

3D three dimensional. 8, 13, 15–17, 24–27, 29, 30, 38–40, 42, 45, 49–52, 54, 58, 59, 63–65, 67, 76, 88, 92, 96, 117, 121, 123, 124, 128, 130, 132–135, 143, 144, 148, 151, 156–161

ADRC Active Disturbance Rejection Control. 9, 27, 131, 137, 139, 140, 151, 156, 159, 161

BIBO Bounded-Input Bounded-Output. 183, 184

CT Computed Tomography. 33, 45

DDRA Data-driven Regression Approach. 12, 44, 105

DoF Degree of Freedom. 15, 26, 32, 33, 36, 46, 59, 74, 76, 78, 80, 94, 157, 160

DS Diagonal Segment. 77–79, 81, 83, 94, 141, 157, 160

DTG Draw Tower Gratings. 62, 63, 128, 161

EDEN2020 An Enhanced Delivery Ecosystem for Neurosurgery in 2020. 15, 41, 42, 75

EM Electromagnetic. 8, 11, 15–17, 19, 26, 29, 30, 33, 42, 45–47, 49, 52, 54, 56, 59, 60, 73, 75, 77, 89, 94–96, 121, 123, 125, 127, 157–160

ESO Extended State Observer. 132, 138–140, 143, 183

FBG Fibre Bragg Grating. 8, 12, 15–17, 26, 27, 30, 42–45, 47, 54, 56, 61–63, 66, 69, 73, 94–102, 105–112, 114–121, 125, 127, 128, 130, 132, 143, 146–148, 150, 156–161, 163, 164

FSF Frenet-Serret Frame. 12, 44, 102, 104, 133

GUI Graphical User Interface. 16, 56, 70–73

HLC High-Level Controller. 11, 17, 18, 27, 30, 48–51, 53, 54, 132, 136–138, 150, 153

KF Kalman Filter. 13, 26, 30, 46, 47, 92, 96, 108, 109, 112, 118, 127, 130, 158, 160

LADRC Linear Active Disturbance Rejection Control. 14, 132, 139, 145–147, 154, 155, 182–184

LLC Low-Level Controller. 11, 17, 27, 30, 48, 51–54, 75, 131, 136–138, 143, 150

LS Leading Segment. 12, 74, 77–79, 81–85, 87, 94, 112, 141, 142, 154, 157, 160

MCF Multi-core Fibre. 8, 15, 16, 19, 26, 27, 42–44, 54, 61–64, 98, 99, 106, 109, 112, 118, 119, 121, 125, 128, 130, 132, 146, 148, 150, 156, 159–161, 163

MIMO Multi-Input and Multi-Output. 137, 156, 183

MRI Magnetic resonance imaging. 33, 38, 45, 46, 58, 95, 158

NADRC Nonlinear Active Disturbance Rejection Control. 132, 139, 145–147, 154, 155

NLGL Nonlinear Guidance Law. 9, 17, 27, 51, 132, 136, 137, 145–148, 154, 156, 159

PBN Programmable Bevel Tip Steerable Needle. 8, 11–13, 15–17, 23–27, 30, 35, 36, 38–42, 45, 46, 48–52, 54–59, 61, 62, 64–68, 70, 73–78, 81, 83–88, 90–92, 94, 96, 111–114, 120–125, 127–137, 139–144, 146–151, 153, 155–161, 163, 164

PD Proportional Derivative. 48, 52

PID Proportional Integral Derivative. 51–53

PTF Parallel Transport Frame. 12, 16, 44, 103, 104, 114, 116, 124, 133

SCF Single-core Fibre. 43, 44, 54

SQP Sequential Quadratic Programming. 137, 140

UAV Unmanned Aerial Vehicle. 27, 49, 51, 132

US Ultrasound. 33, 45, 47, 163

Chapter 1

Introduction

1.1 Motivation

Minimally invasive surgical methods aim to perform surgical procedures quickly and safely through small openings in the skin or skull, as in the cases of laparoscopy and keyhole surgery. Research into these methods has been growing significantly in the last few decades due to improved clinical outcomes, such as quicker recovery, reduced infection, better cosmesis, and lower patient trauma and pain [27], [11].

In addition to their advantages, minimally invasive surgical methods present their own difficulties. The surgeon training duration is prolonged, and higher investment is necessary for the equipment required to conduct the procedure as open surgery counterparts. Moreover, access to target tissues can be challenging through small openings in some procedures, necessitating an open approach that is more invasive but allows better access, vision, and tissue manipulation [121].

In order to eliminate the challenges with minimally invasive surgical methods and allow clinicians to regain their two main senses, touch and sight, which are available in open surgeries but not satisfactorily available in conventional minimally invasive surgical methods, robotic surgical systems that provide dexterity, haptics, and visual-motor coordination have been in the focus of many researchers [120].

Percutaneous intervention is a type of minimally invasive surgery. A typical example of it is needle insertion, which is used extensively, for instance, in brachytherapy [122], drug delivery [86], biopsy, [130] and thermal ablation [95]. A promising tool for needle insertion is steerable

needles, which have been studied widely by many researchers over the last two decades. A steerable needle is one that is able to steer during navigation in soft tissue, such as the brain and liver, to avoid specific anatomical features (obstacles), such as veins and arteries. When compared to conventional rigid needles, their ability to steer enables successful operations, even in the absence of a suitable straight path to the target tissue, which makes steerable needles a potential game-changer in many surgical procedures. In addition to obstacle avoidance, steerable needles are also useful when the target tissue moves due to tissue deformation during the insertion process. In such cases, steerable needles provide the possibility to manoeuvre towards the new location of the target tissue. Therefore, they decrease (i) the need for reinsertion, which increases tissue trauma [23], and (ii) the risk of false diagnosis and ineffective therapy due to, for example, a biopsy being collected from, or a drug being delivered to, the wrong location [84].

To safely navigate instruments in complex anatomy, a number of steerable needles have been proposed. These types of needles enable steering during navigation into soft tissue to avoid critical anatomical features. Many studies have been conducted to investigate the potential of this promising tool. Different types of steerable needle designs were discussed in [119] and [100], with likely the most widely studied example, the bevel-tip needle, shown in figure 1.1.

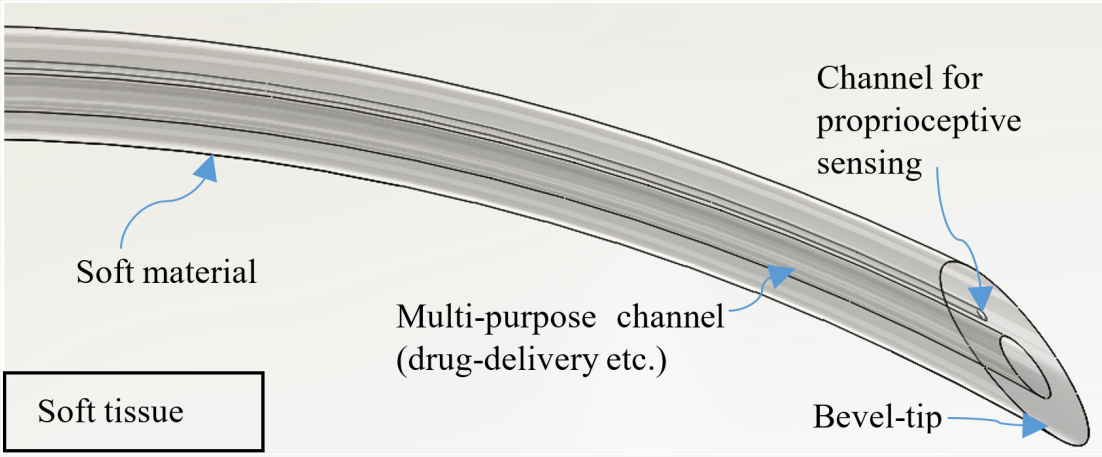

Figure 1.1: A bevel-tip steerable needle

At the Mechatronics in Medicine Laboratory at Imperial College London, studies on the bio-inspired Programmable Bevel Tip Steerable Needle (PBN) have been continuing for about a

decade. The PBN is a bio-inspired steerable needle based on ovipositing wasps' egg-laying channel structure, through which they can lay their eggs, for example, within wood by penetrating and steering into it [15]. Similar to this structure, the PBN consists of relatively soft and slender segments that are held together via an "interlocking mechanism", which constrains the relative transverse motion of the segments. Each segment can be driven independently at the proximal end to achieve relative axial motion, which "programs" the shape of the bevel-tip; thus, the needle can steer through interaction with the surrounding tissue. It has already been shown that PBNs can steer in full three dimensional (3D) space [105], and supervisory navigation of it was shown in [71].

One of the leading open challenges for steerable needles to achieve precise targeting in soft tissue is the need for effective real-time needle tip tracking/shape sensing, which is one of the motivations behind this thesis. The complications caused by poor needle placement include tissue damage, misdiagnosis, under/overdosing therapy, and unsuccessful treatment [84]. Therefore, needle tracking remains a critical focus area for many researchers in this field [113].

In order to account for soft tissue movements and possible target migration, it is also necessary for a modality such as a medical imaging method to be in place, as this behaviour of the tissue is one of the reasons for needle misplacement [3].

In addition to needle tracking and the detection of tissue deformation, another important research challenge in this field is the motion control of steerable needles. Although they provide the ability to steer, this is insufficient for accurate needle tip placement. Efficient guidance control, either by a human or a computerised controller, must also be in place. Although it was shown that PBNs can be guided to target tissues by human controllers [71], computerised controllers seem to be more advantageous, as they eliminate the errors caused by hand tremors, fatigue, and problems in hand-eye coordination, and increase the accuracy and precision of needle insertions [3].

1.2 Aim and Objectives

This thesis aims to explore shape sensing and autonomous 3D path-following methods for a biologically inspired flexible needle for soft tissue intervention.

Hence, the research objectives were as follows:

1. To identify a suitable and robust means for complete PBN tip pose estimation with sensors embedded in one or more of the needle segments
2. To explore full shape estimation during continuous PBN insertion by means of proprioceptive sensing along the PBN segments to improve trajectory tracking
3. To achieve complete, autonomous 3D steering of a PBN along arbitrary curvilinear trajectories within a substrate
4. To validate the controller within a suitable experimental setup under controlled conditions

1.3 Contributions

This study covers the proprioceptive sensing and path-following control of steerable needles. First, it focuses on Electromagnetic (EM) tip tracking methods. Then, it continues with Fibre Bragg Grating (FBG)-based shape sensing. Finally, the path-following control methods, including the lower-level curvature tracking methods, are covered. The contributions can be summarised as follows:

1. EM Pose Estimation for PBNs

A novel algorithm based on 5-Degree of Freedom (DoF) EM sensors was developed for the first time to estimate the full pose of the PBN tip. This algorithm enables tip pose reconstruction for all of the possible tip configurations of PBNs including the case in which the PBN segments are not aligned at the tip, a configuration necessary to create curvature. Additionally, for the first time, all 4 segments of a PBN were instrumented with EM sensors, and their sensory information was able to be fused using the proposed algorithm to construct the overall PBN full pose.

2. Kalman Filter (KF)-Based, Dynamic 3D Shape Reconstruction for Steerable Needles with FBGs in Multi-core Fibres (MCFs)

Another novel algorithm based on FBG-inscribed optical fibres was developed for the full-shape reconstruction of steerable needles. When used in PBNs, it allows tip pose reconstruction for all of the possible tip configurations and it was a first in terms of several aspects: (i) It allows the shape reconstruction of steerable needles, even in the presence of only one FBG set, and it suggests a novel method to integrate other sets if available; (ii) it removes the limit wherein the reconstruction length can only be as long as the length of the sensorised region; (iii) this was the first study offering a method to dynamically fuse FBG-based shape information of PBN segments, which are not necessarily aligned at the tip, to reconstruct the overall PBN shape.

3. 3D Path-Following Control for Steerable Needles with FBGs in MCFs

A novel design and implementation approach for path-following controllers of steerable needles was presented. To handle the needle-tissue interaction uncertainties, Active Disturbance Rejection Control (ADRC) was used as a Low-Level Controller (LLC) (curvature tracking), and accounting for the same nonholonomic constraints as steerable needles, Nonlinear Guidance Law (NLGL), originally developed for Unmanned Aerial Vehicles (UAVs), was implemented as the High-Level Controller (HLC) (path-following controller). Both of these control approaches were used for the first time in steerable needle control. In addition, this study is novel in terms of three more aspects: (i) A method for systematic tip programming for PBNs while observing the permissibility condition, was offered for the first time. (ii) This study is the first path-following steerable-needle study to use MCFs with FBGs. (iii) Finally, this study is the first experimental 3D path-following study of PBNs.

1.4 Publications

Over the course of this thesis, the following papers were completed. The first has already been published. The second one has been accepted and the others were under review (or revision where specified) at the time of thesis submission.

1. Khan, F., **Donder, A.**, Galvan, S., Rodriguez y Baena, F., Misra, S. (2020). Pose Measurement of Flexible Medical Instruments using Fiber Bragg Gratings in Multi-Core Fiber. IEEE Sensors Journal [54]

   The contribution of A. Donder is as follows: Assisting the first author in the development of experimental methods, conducting experiments with the other authors, the production of the guides used in the experiments, reviewing and editing the manuscript, and the preparation of some of the figures.

2. **Donder, A.**, Rodriguez y Baena, F. Kalman Filter-Based, Dynamic 3-D Shape Reconstruction for Steerable Needles with Fiber Bragg Gratings in Multi-Core Fibers. Accepted to IEEE Transactions on Robotics [25]

   The contribution of A. Donder is as follows: The development of all the methods, analyses, and software, conducting the experiments, the design and production of the mechanical components (except for the white actuation unit shown in the paper), writing the original draft, and the preparation of all of the figures.

3. **Donder, A.**, Rodriguez y Baena, F. (**Under Review**). 3-D Path-Following Control of Steerable Needles with Fiber Bragg Gratings in Multi-Core Fibers. Submitted to IEEE Transactions on Robotics [26]

   The contribution of A. Donder is as follows: The development of all the methods, analyses, and software, conducting the experiments, the design and production of the mechanical components (except for the white actuation unit shown in the paper), writing the original draft, and the preparation of all of the figures.

4. Secoli, R., Matheson, E. W., Pinzi, M., Galvan, S., Watts, T. E., **Donder, A.**, Rodriguez y Baena, F. (**Under Revision**). A Modular Robotic Platform for Precision Neurosurgery with a PBN. Submitted to IEEE Transactions on Robotics [106]

   The contribution of A. Donder is the Tracking and Sensor Fusion and Appendix sections: Developing the methods and software regarding EM tracking, conducting the EM-based tracking experiments, designing the 3D guides used in the EM-tracking experiments, writing the original draft of the sections, and the preparation of all of the figures used in the sections.

5. Cui, Z., **Donder, A.**, Rodriguez y Baena, F. (**Under Review**). Nonlinear Trajectory Following Control for a Bio-Inspired Steerable Needle. Submitted to IEEE International Conference on Robotics and Automation (ICRA) [19]

   The contribution of A. Donder is assistive supervision.

1.5 Structure of the Thesis

This thesis is structured as follows.

Chapter 2: Literature about the topics covered in the thesis are reviewed: Early studies with rigid needles for accurate needle placement are presented. Previous research about steerable needle designs, with a focus on PBNs, is given. Literature about shape reconstruction and tip tracking methods are outlined by stating their advantages and disadvantages. Finally, control methods for steerable needle guidance are outlined by splitting the literature into two: HLCs and LLCs.

Chapter 3: The experimental setup used in the validation tests is explained. The PBN, sensors, actuation unit, and the graphical user interface, which are used for the validation experiments, are detailed.

Chapter 4: The EM pose estimation algorithm, from data acquisition till the full pose estimation, is given. Experimental methods and results are presented and discussed.

Chapter 5: The dynamic 3D shape reconstruction algorithm developed for steerable needles with FBGs, is presented. First, the FBG theory and the background about FBG-based shape reconstruction are provided. Then, the proposed shape reconstruction approach is introduced together with the KF-based fusion algorithm. After that, the simulation methods are outlined together with their results. Experimental methods are explained, and results are given. Finally, the results and possible sources of error are discussed.

Chapter 6: The 3D path-following control algorithm, developed for PBNs, is presented after the 3D kinematic modelling of PBNs is given. Both the path-following methods and curvature-tracking methods are covered. Then, a novel method for PBN tip programming is presented. This is followed by a subsection in which a simulation study and parameter tuning are explained. In the next section, the experimental methods are described. Finally, results are presented and discussed.

Chapter 7: The conclusion about the thesis is given. The achievements of the thesis are summarised, and the limitations are presented. Finally, the future work is outlined.

Chapter 2

Literature Review

2.1 Introduction

Needles are extensively used in surgical interventions, as they are minimally invasive and simple to use. Needle placement consists of two parts: 1) placing the needle on the skin with appropriate orientation, and 2) inserting the needle into the target tissue. The skills of the operator play an important role in performing these tasks accurately [32].

In order to place rigid needles to the correct position on the skin and drive them in a controlled manner, several mechanical systems have been proposed. Fichtinger *et al.* proposed a 7-Degree of Freedom (DoF) robotic system [31] for accurate and consistent needle placement in prostate surgery, as shown in figure 2.1 on the next page. Smith *et al.* proposed another system for accurate targeting in breast biopsy [115]. Although these systems aided in the targeting and decreased the targeting error, they did not account for the tissue deformation. It was shown in [21] that there is a considerable possibility of the needle missing the target as the depth of the target increases due to tissue movements. Moreover, it is not guaranteed that there is always an available straight path from the needle entry location on the skin to a target tissue, given that there could be an important anatomical structure in between them. To this end, needle steering systems have been proposed. The evolution of this concept is reviewed in Chapter 2.2.

One of the senses that is very limited in minimally invasive surgery when compared to open surgery is vision. In percutaneous interventions, the interaction of the tip of the medical instrument with the tissue is not seen by the eye. Therefore, an imaging or sensing method

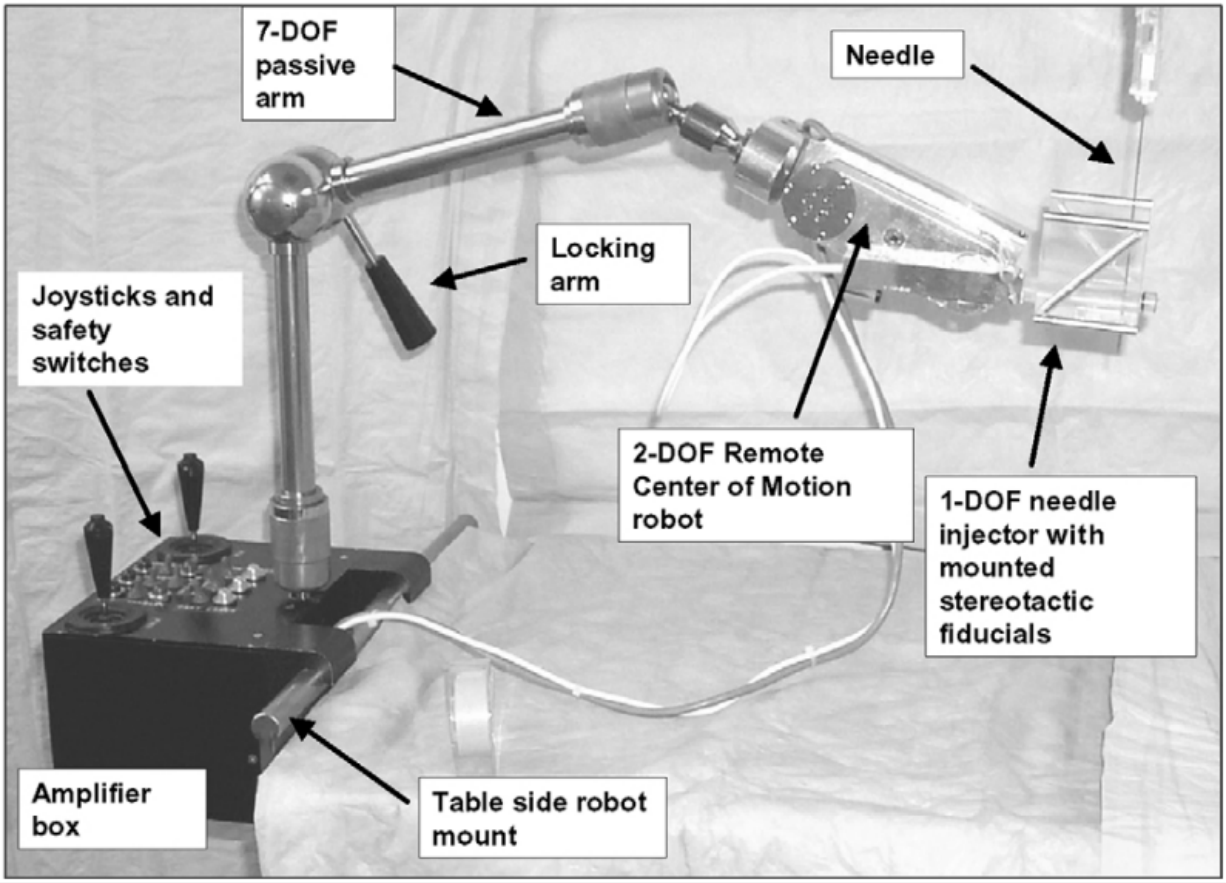

Figure 2.1: 7 DoF robotic system for needle placement developed by Fichtinger *et al.* Reprinted from [31] ©2002, with permission from Elsevier

must be in place for accurate intervention. It is crucial to know either the full pose of the needle tip or the full shape of the needle accurately in real-time during a medical operation to implement robust feedback control. Thus, proprioceptive tracking methods, such as optical fibre-based shape sensing methods [73], Electromagnetic (EM) sensor-based tracking methods [34], and intraoperative medical imaging modalities, such as Ultrasound (US) [112], [2], fluoroscopy [42], Computed Tomography (CT) [111], and Magnetic resonance imaging (MRI) [22] have been studied extensively. Amongst these, the advantages of optical fibres, which are non-ferromagnetic [117], lightweight, small in size, suitable for dynamic-real-time applications, flexible, and radiation-free, make them a promising technology for medical localisation. The literature about these methods is reviewed in Chapter 2.3.

Another aspect that is required for precise needle placement is guidance control, which can be

provided by a human or a computerised controller. Robotic navigation systems have been shown to be advantageous over manual systems due to their abilities in terms of high repeatability, accuracy, and programmability [10]. Therefore, automated and semi-automated navigation systems have been researched extensively [94]. The literature about control methods is reviewed in detail in Chapter 2.4.

2.2 Steerable Needles

In this section, steerable needle designs, particularly Programmable Bevel Tip Steerable Needles (PBNs), are reviewed.

2.2.1 Steerable Needle Designs: An overview

The "needle steering" concept was introduced by DiMaio *et al.*, who presented a method to steer flexible needles to reach specified targets within soft tissue [23]. This method was based on manipulating the needle base and the tissue to direct the needle tip to a desired direction, as shown in figure 2.2. However, one of the significant disadvantages of this method is that it becomes ineffective as the insertion depth increases.

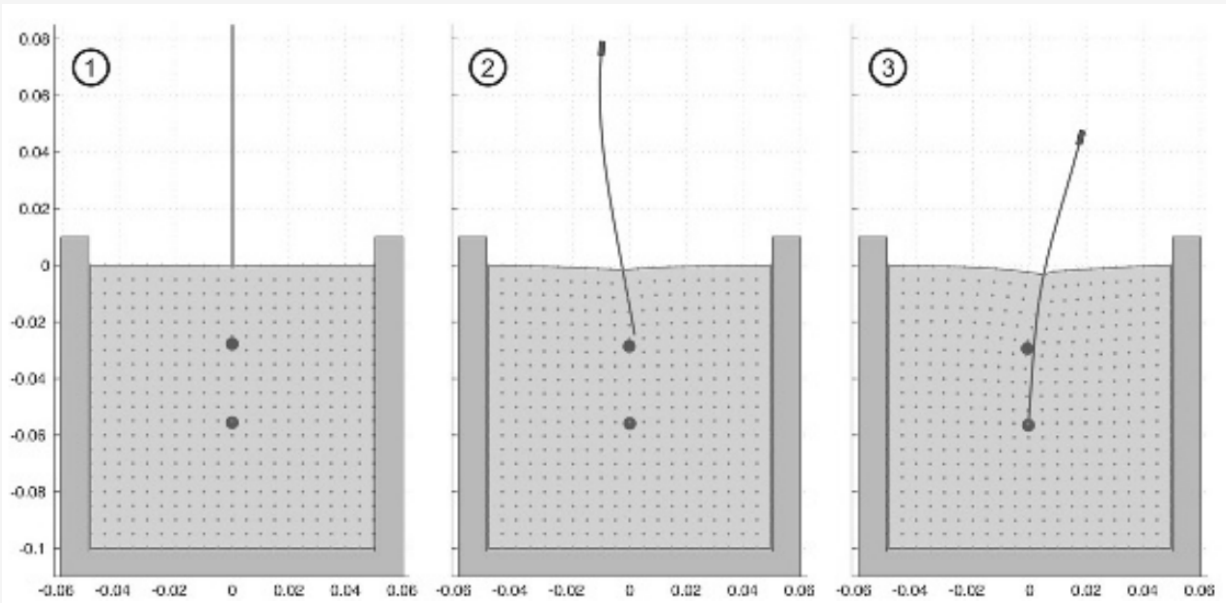

Figure 2.2: Base manipulation-based needle steering.
Reprinted by permission from Springer Nature, [21], ©2003

Studies addressing needle steering continued with [76], in which Okazawa *et al.* introduced a new design for needle steering. They presented a hand-held device with a needle that consisted of a rigid cannula and a pre-curved stylet, which can be rotated within the cannula to set the steering direction and extended from the cannula tip for steering. Research into steerable needles accelerated with [125], in which Webster *et al.* showed the potential that a flexible

needle with a bevel tip could be steered to reach a specified target in soft tissue.

Several steerable needle designs have been proposed to date (figure 2.3), such as bevel-tip steerable needles [72], concentric tube needles [102], tendon-driven steerable needles [91], and PBNs [124].

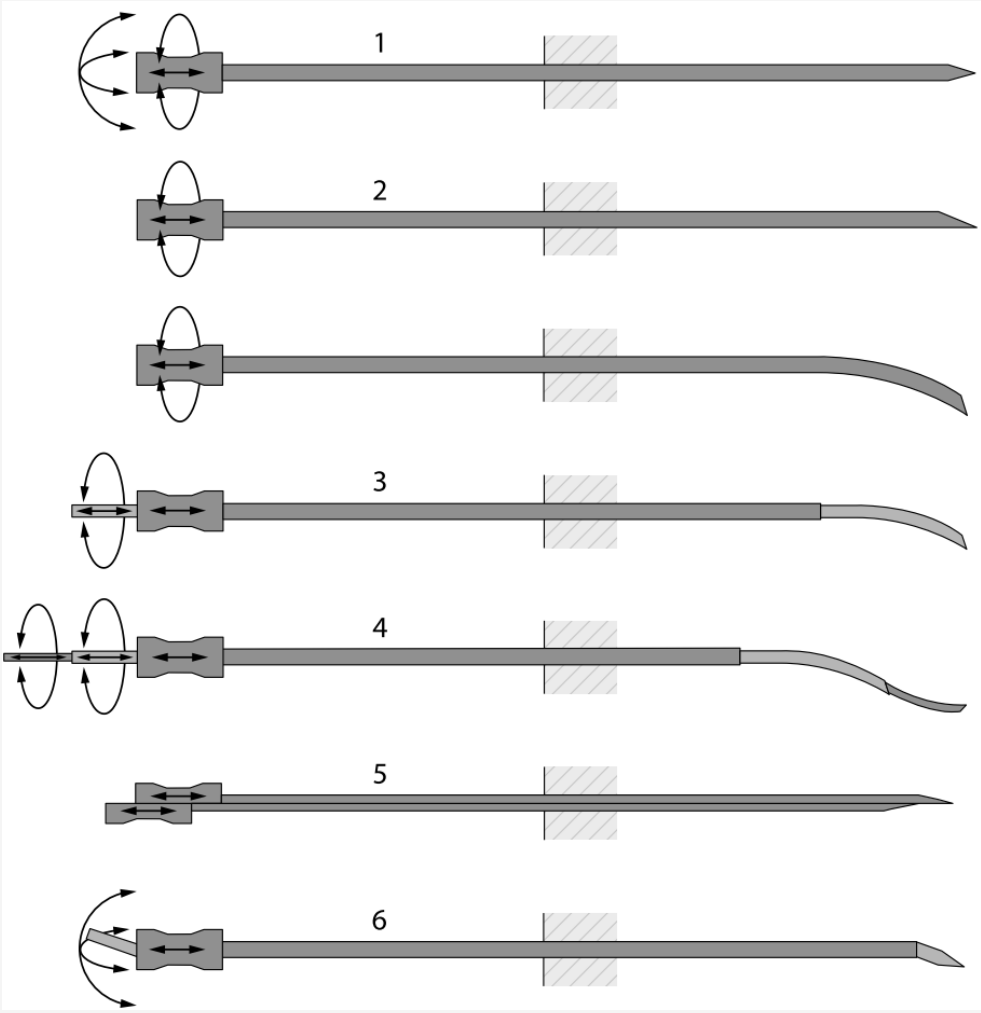

Figure 2.3: Two dimensional (2D) illustration of various steerable needle designs and their DoF in actuation.
(1) base manipulation, (2) bevel tip (with and without precurve), (3) precurved stylet, (4) Active cannula, (5) PBN, and (6) tendon actuated tip steering - Reprinted, with permission, from [119] © 2015 IEEE

Bevel-tip steerable needles, which are often made of flexible materials, are the earliest type of steerable needle and have a fixed bevel-tip angle to steer with constant curvature. The steering is achieved as a result of the asymmetric forces that are exerted on the tip, as shown in figure 2.4.

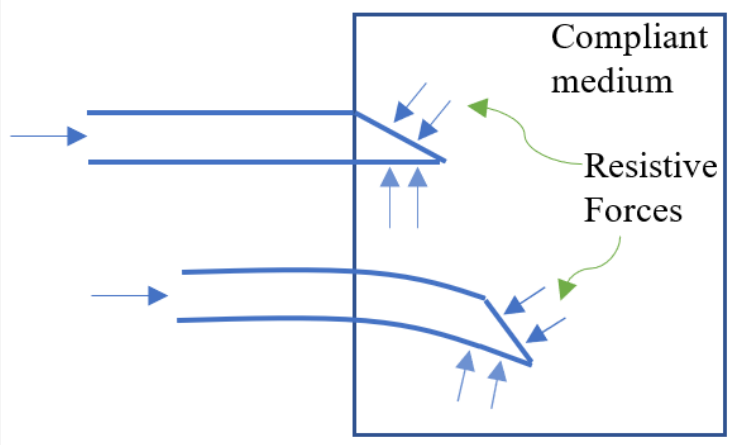

Figure 2.4: Asymmetric forces experienced by a bevel-tip steerable needle

Despite being simple to use on a fixed bending plane, bevel-tip steerable needles require the entire needle body to rotate around the insertion axis to steer in another plane, which causes a torsional moment on the surrounding tissue [68]. Although some variants decrease the possible tissue damage due to this effect via a flexible cannula over the stylet body [76], this type of needle still requires constant rotation to achieve a straight path [7], which may result in helical paths and increased tissue damage. Additionally, in bevel-tip steerable needles, the magnitude of curvature is set by duty-cycled spinning [7], which limits the tools that the needle can be instrumented with, such as optical fibres, because the continuous rotation of the needle body causes cable/fibre wind-up issues. To limit this disadvantage, the curvature-controllable bevel-tip steerable needle was proposed [9]. This needle consists of a bevel-tip stylet and a cannula. These two parts can move axially with respect to each other to control the offset between the bevel-tip and the cannula so that the needle's curvature can be controlled. However, this design also requires constant rotation for straight navigation.

Second, concentric tube needles are telescopically-combined elastic tubes, which do not require the rotation of the needle body in contact with the tissue. However, since the tubes are pre-curved, and there is not much room to update the pre-planned path, they are not tolerant to tissue movements and target tissue migration. Tendon driven steerable needles possess an active tip driven from the base via tendons. To change the steering direction, these needles require their articulated tip to move, which causes tissue displacement and might result in trauma.

On the other hand, the PBN, which is a bio-inspired soft needle (and used in this study), was inspired by wasps, which use their slender ovipositors to penetrate into and steer through some substrates, such as wood, to lay their eggs [15]. Its soft, slender segments are interlaced together via an interlocking mechanism. The PBN is detailed in the following section.

2.2.2 PBNs

The PBN consists of at least 3 segments that can be driven independently to "program" the needle's tip in order to achieve the desired curvature vector, i.e. the curvature value and bending direction, by exploiting the interaction forces with tissue. The main advantages of PBNs over the other well-known steerable needles can be summarised as follows:

- PBNs can be made to be MRI compatible.
- The steering direction can be set to any direction in the three dimensional (3D) space without the need to rotate the entire needle body [105].
- The reciprocal motion of the PBN segments decreases tissue deformation at the needle-tissue interface [78], [70].
- The steering ability can be increased with compliant PBN materials due to the absence of the need for the transmission of torque from the base to the tip, as in the case of duty cycle spinning [7].

However, since the PBN needs to include more than one segment, its diameter is expected to be greater than that of bevel-tip steerable needles with the same properties because a single PBN segment could be considered an independent bevel-tip steerable needle. Therefore, for example, the diameter of a 4-segment PBN is two times that of a bevel-tip steerable needle, equivalent to one of its segments. In addition, the working channel diameter of PBNs are expected to be smaller than other type of steerable needles with the same outer diameter as the PBN's working channels cannot be larger than its segments. However, depending on the application, this limitation could be compensated for by using all the working channels simultaneously. Even if some channels are used for proprioceptive sensing, the sensors could be removed when

the needle tip reaches the targeted tissue so that the channels could also be used for other purposes, such as drug delivery.

A 4-segment PBN is shown in figure 2.5.

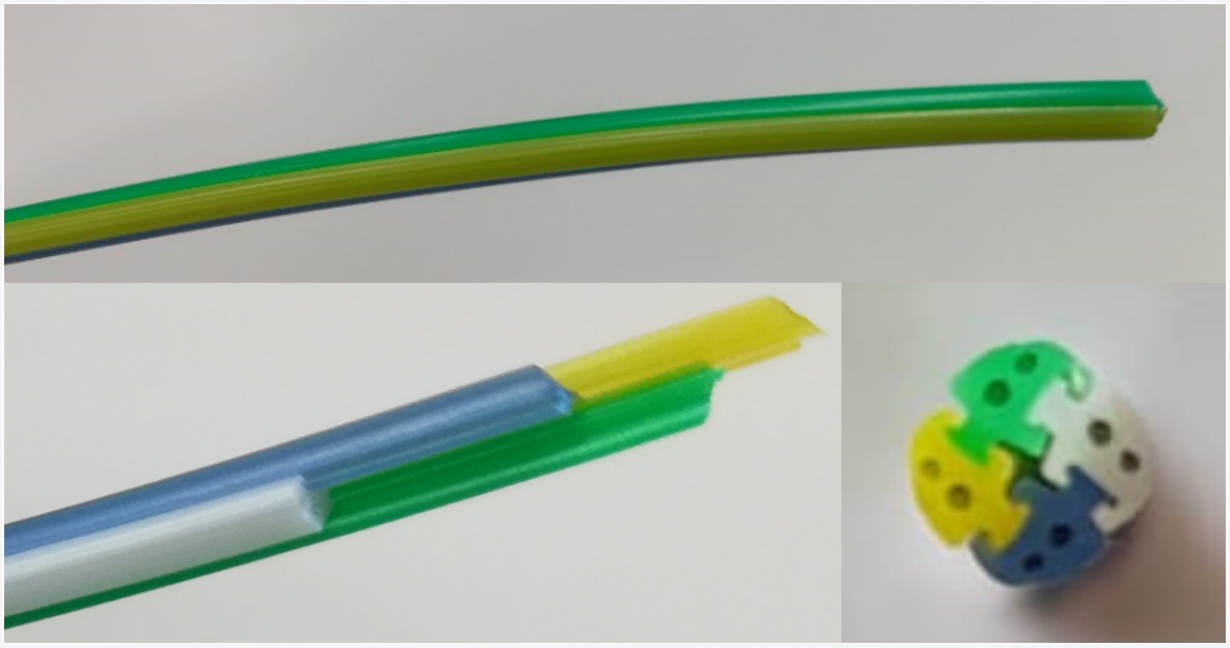

Figure 2.5: A 4-segment PBN. Top: Overall appearance with zero relative offsets between PBN segments, Bottom left: PBN tip close-up with non-zero relative offsets between PBN segments, Bottom-right: PBN front-view, illustrating two hollow lumens per segment

The modelling studies in the PBN steering mechanism are analysed in two groups: 2D steering modelling and 3D steering modelling.

To begin with, Ko *et al.* proposed the implementation of the bicycle model, which was originally developed for car-like steering, into the PBN 2D steering modelling in [55], [56], [57] based on the similar nonholonomic constraints of both systems. They replaced the steering angle with "steering offset", which was defined as the distance between the segment tips and presented the nonlinear PBN planar steering model. Another approach, which offers a finite element modelling of PBNs, was presented in [77] by Oldfield *et al.* The authors proposed to use a cohesive approach to estimate strain energy release rate during crack formation, and they modelled the cutting process in this way. It was shown that with this approach, the characteristics of PBN-tissue interaction was significantly captured. A similar approach was proposed by

Terzano *et al.* in [118], where an adaptive finite element model for PBNs was proposed. In this study, the fracture that happens during the needle's penetration was described by again a cohesive zone model. Leibinger *et al.* presented a PBN-tissue interaction study using a scanning laser-based image correlation technique [61]. The authors proposed placing fluorescent melamine resin beads into the soft tissue phantom to detect the tissue movements by optical measurements.

The first method for the kinematic modelling of the PBN 3D steering was developed by Secoli *et al.*, by assuming a similarity with underactuated underwater vehicles [103]. The concepts presented in this simulation study were based on the similar nonholonomic constraints of both of the systems and were proven *in vitro* in [12]. Finally, Watts *et al.* presented a comprehensive 3D steering model with the utilisation of a multi-beam approach based on the Euler-Bernoulli beam theory [124]. In their paper, the needle curvature was estimated according to the needle tip displacement, and the developed methods were validated with gelatine experiments.

Additionally, in order to understand the relationship between the steering offset and the curvature, several 2D and 3D studies were conducted. This was first studied in [55] and [56], in which simple least-squares fitting was used to fit circles to PBN paths to calculate the average curvature. Based on the 2D experiments, it was shown that the steering offset was proportional to the curvature. This has also been confirmed by Terzano *et al.* with a finite element study in [118]. Burrows *et al.* enhanced this relationship to 3D and demonstrated that the linear relationship assumption between the steering offset and curvature was also valid in 3D [12]. In their study, circles were fit to the paths of the PBN tips that were created in gelatine with constant offsets to estimate the average curvature.

The effect of the PBN's stiffness to the curvature was studied in [118]. It was shown how the PBN stiffness reduces the curvature of its path with a finite element study.

Finally, Frasson *et al.* investigated the curvature's relationship with the bevel angle and outer diameter of the needle in [35]. They conducted gelatine experiments using PBNs with different bevel-angles and outer diameters, and showed that if the bevel angle and/or needle outer

diameter was increased, larger curvatures were achieved.

An Enhanced Delivery Ecosystem for Neurosurgery in 2020 (EDEN2020): The PBN was the core of the European Research Council's EDEN2020 project, which continued from 2016 to 2021 and aimed for the gold standard for neurosurgical diagnosis and therapy. In this project, several *ex vivo* and *in vivo* trials were made that utilised the tracking and shape reconstruction methods developed in this thesis. These trials were not in the scope of this thesis, but the full surgery system is explained here briefly for completeness and to create a better picture of state of the art regarding PBNs.

The full surgery system (figure 2.6) for the delivery of the PBN was developed by the EDEN2020 team, and its main components were as follows:

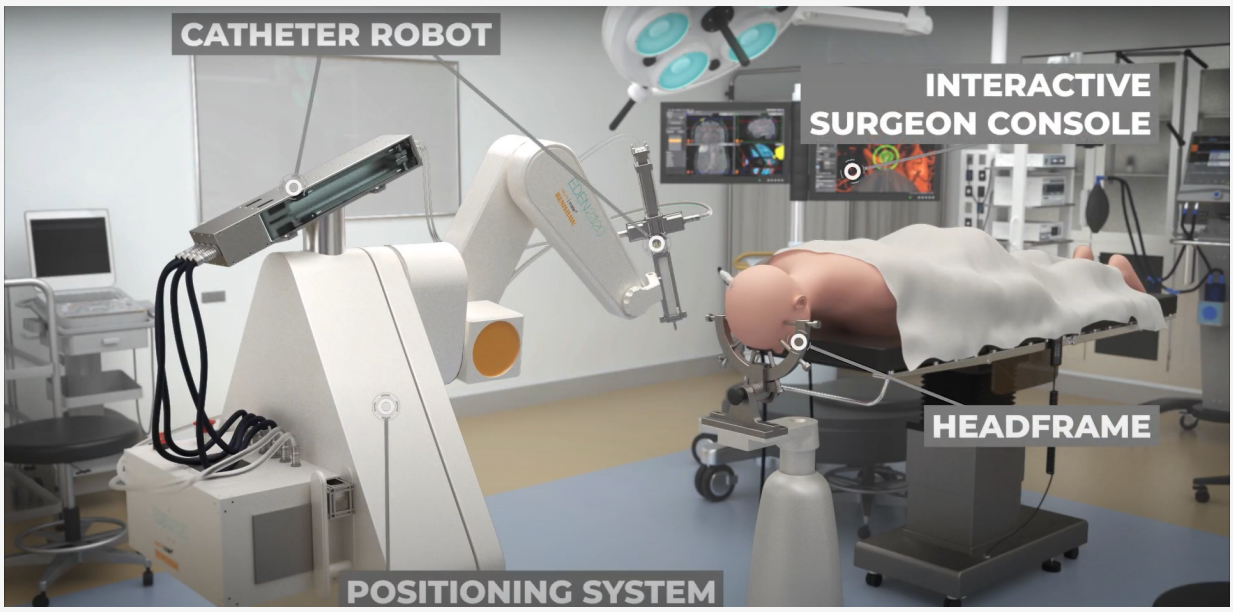

Figure 2.6: EDEN2020 - Fully functional technology platform for precision neurosurgery - www.eden2020.eu

1. The PBN: A 4-segment PBN was used in the experiments, which was equivalent to the one used in this thesis.

2. The gross positioning robot (Renishaw neuromate): This robot was used to position the PBN on the skull to the needle entry location.

3. The actuation unit with flexible transmission: In order to reduce the weight that the

positioning robot needs to carry, only the delivery unit was fixed to the robot arm, and it was connected to the actuation unit, which was fixed to the robot base, via a flexible transmission. The design of the delivery unit allowed the accommodation of the shape sensing hardware required for EM and Fibre Bragg Grating (FBG)-based reconstruction (Multi-core Fibres (MCFs) and EM sensors).

4. The interactive surgeon console: This included a visual interface and master device to control the needle.

The EDEN2020 system used quaternions for communications and 3D transformations. Therefore, after the PBN tip transformation matrix was calculated using the proposed tracking and reconstruction algorithms given in Chapter 4 and Chapter 5, it was converted to quaternions. For completeness, the method used for this calculation is given here. Assuming that $\boldsymbol{R}_{Tip} \in \mathbb{R}^{3\times3}$ is the catheter-tip-frame rotation matrix, the rotational transformation of the PBN tip with respect to the inertial reference frame in quaternions is:

$$\boldsymbol{q}_{Tip} = \begin{bmatrix} q_{w,Tip} & q_{x,Tip} & q_{y,Tip} & q_{z,Tip} \end{bmatrix} \tag{2.1}$$

where,

$$q_{w,Tip} = \frac{\sqrt{1 + \boldsymbol{R}_{Tip}(1,1) + \boldsymbol{R}_{Tip}(2,2) + \boldsymbol{R}_{Tip}(3,3)}}{2} \tag{2.2}$$

$$q_{x,Tip} = \frac{\boldsymbol{R}_{Tip}(3,2) - \boldsymbol{R}_{Tip}(2,3)}{4q_{w,Tip}} \tag{2.3}$$

$$q_{y,Tip} = \frac{\boldsymbol{R}_{Tip}(1,3) - \boldsymbol{R}_{Tip}(3,1)}{4q_{w,Tip}} \tag{2.4}$$

$$q_{z,Tip} = \frac{\boldsymbol{R}_{Tip}(2,1) - \boldsymbol{R}_{Tip}(1,2)}{4q_{w,Tip}} \tag{2.5}$$

The detailed explanation of the system is given in [106].

2.3 Shape Reconstruction and Tip Tracking

Shape reconstruction methods based on FBG-inscribed optical fibres have been introduced for about a decade [81], [45], [92], [16]. The FBG working principle is shown in figure 2.7. A part of the light spectrum generated by an optical spectrum interrogator is reflected back by FBGs etched on the optical fibre. This reflected wavelength is called the Bragg wavelength. Change in the strain or temperature causes the Bragg wavelength to shift, which, therefore, enables them to be measured.

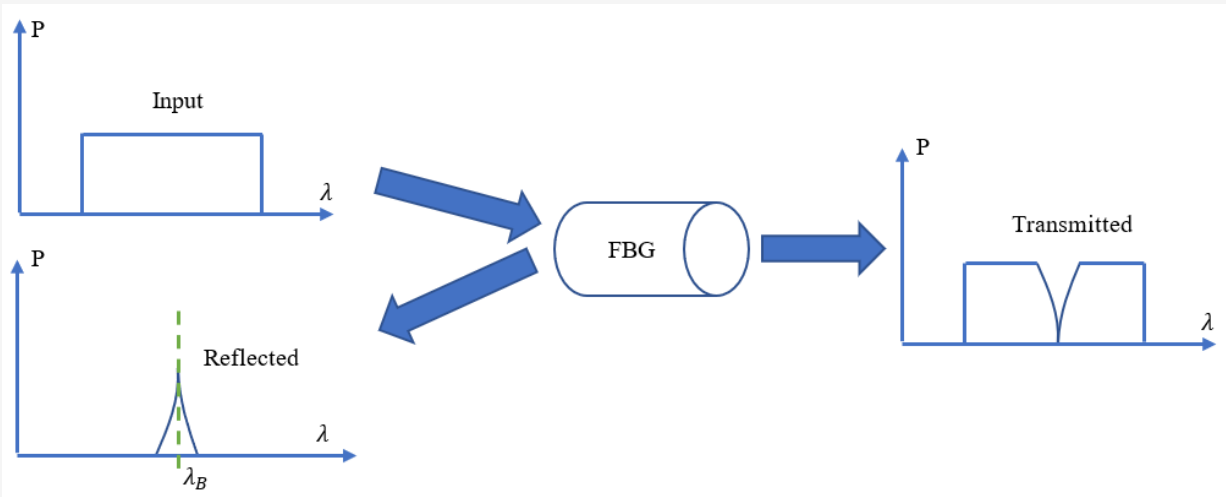

Figure 2.7: Illustration of the FBG working principle

Shape sensing with FBG sensors requires at least 3 cores with several FBG sensors in each core [46]. This could be achieved either by using 3 Single-core Fibres (SCFs) or 1 MCF with 3 cores, as shown in figure 2.8 on the following page.

SCFs are generally used as bundles that are held together via a supporting structure such as epoxy [74]. Alternatively, they could be placed along the grooves of a cylindrical tool [63]. However, one of the most important challenges with SCFs is that they need to be precisely placed with respect to each other. The positioning and alignment difficulties encountered with SCFs were discussed in [83]. Nonetheless, improvements arising with the use of MCFs [54] have eliminated the positioning and alignment difficulties encountered with SCFs and have enabled the spread of FBG-based shape reconstruction methods. One of the other challenges with

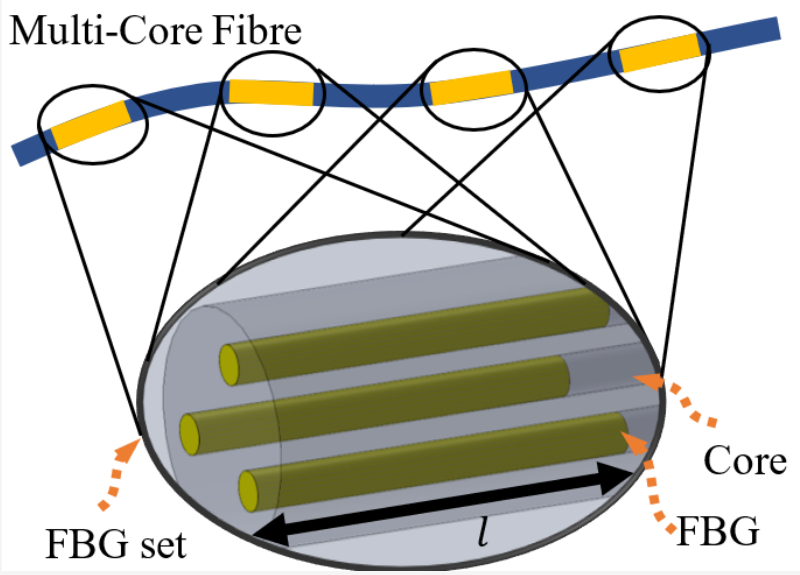

Figure 2.8: Illustration of an MCF with three cores

FBG-based reconstruction is the measurement of torsion, as it is not possible to distinguish wavelength shifts caused by bending and torsion in the configuration in which the fibres lie along the tool. To this end, the helical configuration of MCFs was proposed in [4]. The authors proposed twisting MCFs helically during draw. Similarly, Xu *et al.* proposed fixing SCFs along helical grooves over a cylindrical tool [127].

FBG-based reconstruction methods in the literature can be grouped into 5 main categories: Frenet-Serret Frame (FSF)-based methods [75], [53], Parallel Transport Frame (PTF)-based methods [18], [54], piecewise constant curvature methods [92], [79], polynomial shape-based methods [109], [63], [81] and Data-driven Regression Approachs (DDRAs) [107]. Given that the spacing between consecutive FBG sets along an MCF can only be so small, all of these methods suffer from the limited number of discrete measurement locations along an MCF.

To address this drawback, interpolation or curve fitting techniques have been suggested to estimate the intermediate curvature vectors in all of the methods, except for DDRA. These techniques bring along with them inherent approximation inaccuracies. Similarly, in DDRA, regression performance is a function of the number of measurement locations. Specifically, in all of these methods, as the FBG sets become sparse along the fibre, the shape reconstruction accuracy becomes increasingly susceptible to the relative position of the bending direction

discontinuities with respect to the gratings, as investigated in this study. One way to increase the accuracy is to increase the number of FBG sets along the fibre. However, this comes at the expense of higher manufacturing costs, higher calibration complexity, and the increased probability of fibre damage and malfunction [109].

Another medical imaging method that is used to localise medical tools is US imaging. Due to its clinical advantages, such as its high update rate, being easy to use, and not emitting ionising radiation, US has been widely used in medical localisation. In [2], Abayazid *et al.* used 3D US scanning as feedback to automatically steer a bevel-tip steerable needle. However, using only US is not always sufficient due to its low signal-to-noise ratio and resolution [20]. Therefore, Shahriari *et al.* suggested fusing the reconstructed needle shape from FBG measurements with the one from US measurements, which resulted in a more robust reconstruction [112]. US can also be employed to reconstruct the shape of anatomical features [41].

MRI is also a commonly used modality in medical imaging [67]. Henken *et al.* used MRI as feedback for steerable needle navigation. Although its advantage of providing high resolution images makes it a considerable imaging and localisation option, it comes with the cost of high maintenance expenses. Moreover, the medical instruments, including flexible catheters and needles, must be non-ferromagnetic in order not to affect the generated magnetic field, which limits the variety of the available medical tools.

On the other hand, fluoroscopy and CT are the two imaging modalities that generate high doses of X-rays, which are harmful to both patients and clinicians. In [42], Glozman *et al.* used fluoroscopy to detect a flexible needle shape, which was used for accurate navigation. Moreover, CT was used in [111] to track and guide a flexible biopsy needle.

Camera systems are used generally for needle tracking in experiments under controlled conditions. Watts *et al.* used a stereo camera pair to track the 3D tip position of a PBN in gelatine phantom [124]. A similar system was used in [126] to track a bevel-tip needle. The limitation of this method is that it requires line of sight, and thus, has limited usage in clinical settings.

Finally, EM tracking systems are also one of the proprioceptive tracking modalities that have

commonly been used in steerable needle tracking [34] due to their advantages in clinical settings, as listed below:

1. EM sensors are small enough to be embedded within the needles.
2. They do not require the presence of line of sight.
3. They cause a decrease in the fluoroscopy times [101].
4. They do not affect the mechanical properties of needles due to their compliance.

In addition to the positive sides of the EM tracking systems, their disadvantages can be given as follows:

1. The EM field is sensitive to other magnetic substances in the vicinity of the EM field generator. Due to this, EM tracking systems are not compatible with MRI [34].
2. The accuracy of the sensors is not uniform throughout the EM field. The best quality is generally achieved at the field centre [88].
3. The smallest commercially available EM sensors, which are suitable for the segments of the clinically sized 4-segment-PBN [124], are not 6-DoF but they are 5-DoF.
4. In the case of shape estimation, several EM sensors can be used along a needle. However, the physical connection between the sensors and the processor would increase the needle thickness [113].

EM-based methods were also used extensively in PBN studies which are initiated with [56], in which an EM sensor was embedded within one of the segments of a 2-segment PBN. In the following PBN papers using EM sensors, instrumentation of only one of the PBN segments continued [57], [58]. As best as is known, the only study that used a PBN with more than one EM sensor was [105], in which only two of the segments of 4-segment PBN contained EM sensors.

In order to increase the tracking accuracy, sensory information from various modalities can be fused. Kalman Filter (KF) is one of the most extensively used methods for sensor fusion

[20], [5], [28]. The reason for this is that it is well-suited for real-time applications with a stochastic nature. In [20], it was used to combine a flexible catheter tip position obtained using both US-based and FBG-based tracking methods. Similarly, to increase the needle tip position tracking accuracy, in [50], a KF was used to fuse the information from an optical tracker and an EM sensor. Another study about needle insertion was [99], in which the needle tip tracking accuracy was increased by fusing the tip position information from a less accurate but smaller EM sensor at the needle tip and a more accurate but bigger EM sensor at the needle base together with a deflection model.

2.4 Control Methods

The controllers used in steerable needle navigation can be grouped into two categories, as High-Level Controllers (HLCs) and Low-Level Controllers (LLCs). Closed-loop HLCs are designed to generate high-level commands for LLCs by utilising feedback from sensing modalities. Then, the LLCs apply the inputs to actuators to track the commands. For example, in a path-following task, a closed-loop HLC evaluates the error between the reference path and the needle pose, and the commands it generates for the LLC could be curvatures, which are then tracked by the LLC by generating commands directly for the actuators.

In both of the following subsections, which include the literature review about steerable needle HLCs and LLCs, the focus is given to PBNs, and the studies including them are presented first. The studies related to the other steerable needles are covered afterwards. The HLC methods also include a brief overview of the control methods used in other nonholonomic systems.

2.4.1 HLCs for Steerable Needles

Initial attempts in HLC designs for PBNs started in 2D almost a decade ago. In [36], Frasson *et al.* investigated the planar trajectory tracking capabilities of PBNs with a Proportional Derivative (PD) controller in a simulation environment. The smooth convergence of the curvature-based algorithm was shown under a synthetic Gaussian noise that replicated positional sensor error and LLC error.

In another study about path-following HLC designs for PBNs, Ko *et al.* [55] adapted a closed-loop control algorithm [65], which was originally developed for car-like robots, to follow 2D trajectories. The methods in this study were also tested in a simulation environment by assuming (i) that there was zero friction between the PBN segments, and (ii) that the PBN was very flexible while being stiff in tension and in compression.

The first attempt in which controller performance was tested *in vitro* was in [56], in which Ko *et al.* used a 4-segment PBN for the first time, although only two of the segments were used

actively to track planar trajectories in gelatine phantom. An EM sensor was placed in one of the active segments for position feedback, and a similar method to the one in [55] was used for the control law. A kinematic model of the PBN was derived, and the path-following HLC was implemented through approximate linearisation.

In a similar study [58], Ko *et al.* analysed the trajectory tracking performance of the controller presented in [56] through *in vitro* experiments, again over planar trajectories using a 2-segment PBN. In this study, the controller was integrated with a smooth path planner, and the study showed the PBN's first integrated planning and execution trial, which was an important step towards a fully automated PBN system.

In the final PBN study in 2D [57], an alternative closed-loop control approach using model predictive control for steerable needle trajectory following was developed by Ko *et al.*. In this study, the nonlinear kinematic model of the PBN presented in [56] was modified to have a linear tracking error model. Therefore, the linearised model was used to optimise the future output of the system by reducing the computational load. With this method, more robust performance was obtained when compared to the previous trials of the PBN path-following controllers.

After all of these studies in 2D, the first study about 3D motion control of PBNs was presented by Secoli *et al.* in [103], in which the authors validated a closed-loop trajectory-tracking controller's performance in simulation. In this study, kinematic modelling of the PBN based on an underactuated underwater vehicle was presented for full 3D motion for the first time, and an HLC was designed to generate angular velocities around the lateral axes of the PBN tip frame. The simulation results confirmed the 3D path-following potential of PBNs.

After that, an adaptive controller that was able to deal with the unmodelled dynamics of the tissue-needle interaction was presented in [104]. This study proposed an HLC for 3D trajectory tracking that was adapted from a controller designed for Unmanned Aerial Vehicles (UAVs) [51], [116] due to the similar nonholonomic constraints in both systems. The needle tip was considered as a point mass in the 3D space, and the controller's performance was tested in simulation.

It was also shown that PBNs could be guided to target tissues effectively by a human controller when accompanied by a suitable human-machine interface. In [71], Matheson *et al.* presented a human-machine visual interface for neurosurgical steerable needle guidance. It was shown that it is possible for PBNs to be guided by a human operator with a millimetre range accuracy.

In addition to the studies including PBNs, Rucker *et al.* [97] developed a model-independent HLC with sliding mode control based on a generalised unicycle model [125] for a flexible asymmetric-tipped needle to follow a predefined 3D trajectory. The performance of the controller was shown with experiments in phantom tissue and *ex vivo* liver tissue, with some of the experiments including moving targets.

Xu *et al.* developed a 3D trajectory-following controller using fuzzy logic, which did not require an exhaustive mathematical derivation, for a curvature-controllable steerable needle [126]. This type of controller was proven to be effective in hard-to-model environments [60]. In [126], the reference path was constructed as piecewise planar, and two planes, namely *in-plane*, which includes one planar segment of the trajectory, and *off-plane*, which is orthogonal to *in-plane*, were defined. The experiments in gelatine showed that the designed fuzzy controller is capable of correcting the errors in both of the planes with high accuracy.

Rossa *et al.* developed a haptic device for physicians and a robotic brachytherapy needle to work in tandem [93]. The haptic feedback from a wristband including a vibrating actuator was used to help surgeons control the needle's trajectory. Another example to this concept is [63], in which Li *et al.* suggested providing clinicians with visual feedback about the required control action to deliver the tip of a bevel-tip steerable needle to a desired point.

On the other hand, Patil *et al.* designed an optimal linear quadratic Gaussian feedback controller for steerable needles to navigate around obstacles [82] by considering the uncertainty in time-dependent, large deformations. The method developed in this study estimated state distributions based on uncertainties, which were used to select the safest navigation plan. This study was validated through a finite element method-based simulation.

In [64], Li *et al.* proposed a discrete path-following algorithm for a bevel-tip needle based on

duty-cycle spinning and the Lie group theory. The path-following HLC was designed in such a way that it corrected for the heading error and the cross-track error of the needle tip. The controller's performance was tested via simulations and gelatine experiments.

Abayazid *et al.* developed a controller for the same type of needles based on constructing a conical-shaped "reachable region" and always keeping the target in this region by controlling the needle's bending direction [1]. Although this concept is capable of guiding a needle from the entry point to the target, it cannot follow a specific path.

Despite the growing amount of research over the last decade, accurate guidance of steerable needles is still an open research challenge. Moreover, with regards to the path-following controllers of PBNs, despite the above references, there are still no studies presenting a complete 3D path-following controller with experimental validation.

In addition to the aforementioned control methods, the controllers developed for other nonholonomic systems could also be used in steerable needle systems due to having the same constraints. For example, the vector-field algorithm presented in [52], the nonlinear model predictive controller given in [89] and the fuzzy controller outlined in [96], which were used for path-following controls of mobile robots, are also suitable for steerable needles. Finally, as reviewed in [116], the algorithms developed for UAV control, such as carrot-chasing algorithm and Nonlinear Guidance Law (NLGL), could also be used in steerable-needle path-following control studies.

2.4.2 LLCs for Steerable Needles

PBN LLCs are based on arranging the PBN segment offsets to achieve a path-following performance in the higher level. Some of the LLC designs for PBNs are based on open-loop control, in which the inputs are determined according to the kinematic model of the PBN. In the first study about PBN LLCs [55], the bicycle model of the 2-segment PBN was converted into a single chained form, and based on this model, an open-loop LLC was developed. The performance of the controller was verified with simulations along with the developed HLC.

In another similar PBN study, Proportional Integral Derivative (PID) control was used for a

closed-loop LLC, which was designed to control the segment lengths. It was tested *in vitro*, [56] and its feedback loop was closed with the actuator encoders.

LLC studies including an optimal controller started with [103], in which the controller minimised the relative change in segment velocities with respect to the overall needle insertion speed. This simulation study was also the first study that considered the needle navigation in 3D. Later on, the 3D manoeuvrability capabilities of the needle were tested *in vitro* in [12] with an open-loop LLC, which controlled the segment velocities. Secoli *et al.* continued these studies, including an optimal controller with a simulation study [104], in which the optimal LLC controller was minimised the relative offsets of the segments as opposed to [103], in which the controller was minimised the relative change in the segment velocities with respect to the overall needle insertion speed. In [104], an LLC was structured with a PD controller and an adaptive sliding mode controller, of which the contributions were summed to form the control input. According to the simulation results presented in this study, although the steady-state error is almost none, the settling time is relatively high ($\sim$50 seconds), which is not ideal depending on the procedure duration and needle insertion length. In [105], Secoli *et al.* implemented the LLC presented in [104] *in vitro* after updating the adaptive controller in such a way that it directly affected the PID controller gains instead of its output being added to the output of the PD controller. This study also included an optimal controller in which the optimal LLC controller minimised the relative offsets of the segments. Finally, in [105], Secoli *et al.* presented a controller based on radial basis function neural network and PID controller combination for curvature tracking. This closed-loop controller was tested *in vitro* with two EM sensors placed at the tips of the two segments of the 4-segment PBN.

In addition to the studies mentioned above, there are also some studies focusing on reducing tissue deformation by using a different strategy in the LLC design. Matheson *et al.* suggested a cyclic motion control approach in [69], [70], in which the motion profiles of the LLC were optimised to minimise the tissue deformation. They showed that the cyclic motion LLC had better results in terms of tissue deformation despite its negative effect in 3D trajectory tracking.

The LLC methods of other steerable needles were based on their mechanisms. Bevel tip steer-

able needles require rotational actuation to change the steering direction and linear actuation for insertion. In [63], Li *et al.* used a human controller to guide the needle. In their study, the LLC was for rotational actuation. The control idea was to always keep the target in a region that was accessible by the needle by rotating the needle when required. Therefore, the operator was expected to intervene in this way to respond to the HLC. On the other hand, for the same LLC concept and to control the needle in a similar way, Abayazid *et al.* developed an automatised LLC in [1].

Likewise, a PID controller was used in [126] as the LLC of a bevel-tip curvature-controllable steerable needle to control its control offset and steering direction. Finally, a position controller was presented in [91] for a tendon-driven actuated-tip needle, but this time, to control the tendons, which actuated the needle tip to set the steering angle and direction.

2.5 Conclusion

In this chapter, the literature about steerable needles, shape reconstruction methods, tip tracking methods, and control methods were reviewed. First, examples of the studies offering mechanical system designs for accurate needle placement were given. One of the most important drawbacks of such systems is that they do not take into account the tissue and needle deformation that might occur during needle insertion. Moreover, these systems assume that there is always an available straight path between the entry point and the target tissue, as opposed to steerable needles, which can avoid "obstacles" by steering in the tissue. Therefore, the literature about steerable needles was given, and the advantages of different designs were outlined with a particular focus on PBNs and their modelling.

A modality providing vision or sensing must be in place for accurate needle guidance. The methods addressing this were given along with a discussion about their advantages and disadvantages. Among many, FBG-based reconstruction methods draw attention due to their advantages over the other modalities. However, they suffer from a limited number of discrete measurement locations. The difficulties encountered with SCFs in FBG-based shape sensing and the advantages that come along with MCFs were given. Although FBG inscribed MCFs are becoming more and more popular in the shape sensing of needles, they have not been used to provide feedback for a path-following controller. EM-based sensing methods are also common, but it might not be possible to use several of them for shape reconstruction of a thin cylindrical medical tool, as each EM sensor has its own wiring limiting the minimum tool thickness. Furthermore, there were no studies in the literature on the EM-based full-tip pose reconstruction of PBNs.

Finally, the literature about the control methods of the steerable needles was outlined. The methods in the literature were presented by grouping them into two categories: HLCs and LLCs. Although the path-following controllers developed for many types of steerable needles were tested experimentally, there were no studies in the literature about an experimental 3D

path-following study of PBNs.

In the next chapter, the components of the experimental setup, used in the validation experiments of the methods proposed in this thesis, are presented.

Chapter 3

Steerable Needle Sensing and Actuation - Experimental Setup

3.1 Introduction

In this section, the experimental setup, which was used to conduct the validation experiments under controlled conditions, is introduced. The setup consisted of the following components:

- Programmable Bevel Tip Steerable Needle (PBN): The steerable needle used in the experiments to validate the developed methods.
- Electromagnetic (EM) sensor setup: These sensors were used as tip tracking modality for the algorithm explained in Chapter 4, and as ground truth to validate the methods given in Chapter 5.
- Fibre Bragg Grating (FBG)-inscribed optical fibre setup: This setup was used for shape sensing in the validation experiments given in Chapters 5 and 6.
- Actuation unit: This unit was used to drive the PBN segments back and forward with a desired velocity in controlled manner in validation experiments.
- Graphical User Interface (GUI): For the sake of simple management of the entire setup, a GUI was developed and integrated with the actuation and sensing programmes developed in this study.

Detailed information about these components is given in the following subsections.

3.2 Programmable Bevel Tip Steerable Needle

In this study, validation experiments were performed using a PBN. Illustrations of a 4-segment PBN, which was developed previously as part of the EU Horizons project entitled "An Enhanced Delivery Ecosystem for Neurosurgery in 2020" and used in this study, are shown in figure 3.1. It had 0.25 mm and 0.3 mm outer-diameter lumens through each segment for (i) surgical interventions, such as drug delivery, and (ii) proprioceptive sensing.

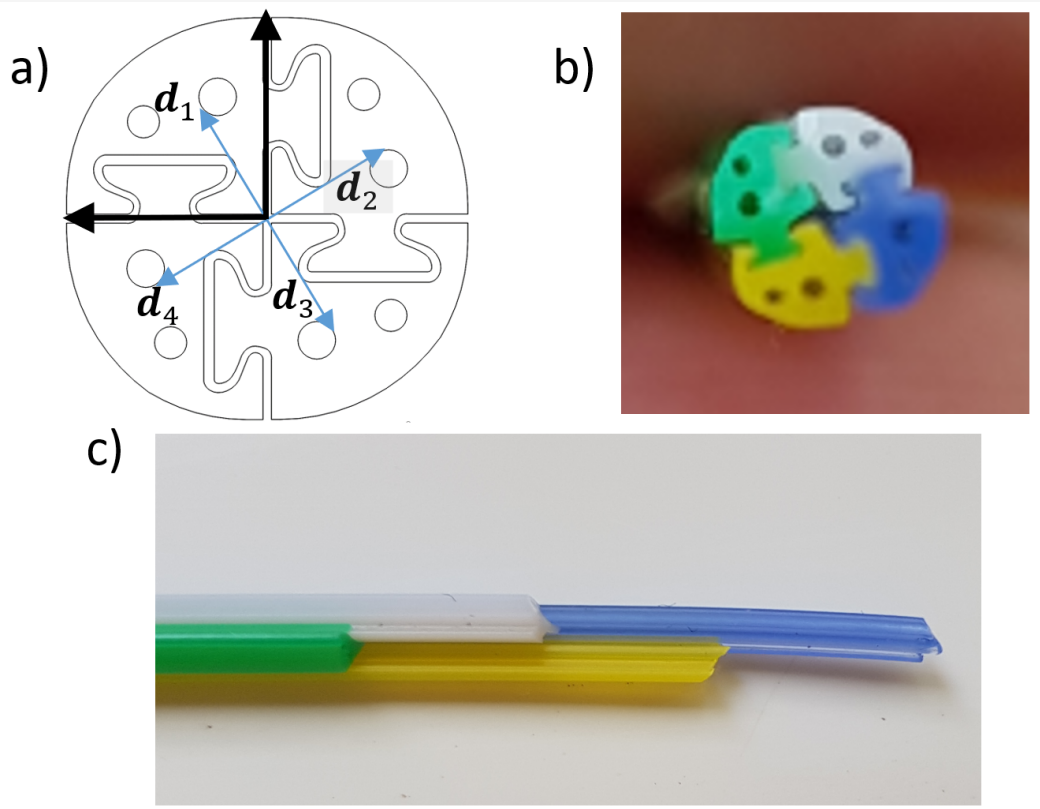

Figure 3.1: 4-segment PBN a) Illustration of the cross-section and interlocking segments. The circles represent the working channels that can be used for sensor placement or drug delivery etc. $\boldsymbol{d}_h \in \mathbb{R}^{2\times 1}$ is the neutral axis discrepancy of the hth segment, $h \in \{1, 2, 3, 4\}$. b-c) 4-segment PBN.

Each PBN segment also had a "wing" used for actuation. They were glued to nitinol rods whose other ends were connected to the actuation unit, as detailed in Chapter 3.5. The wings are shown in figure 3.2.

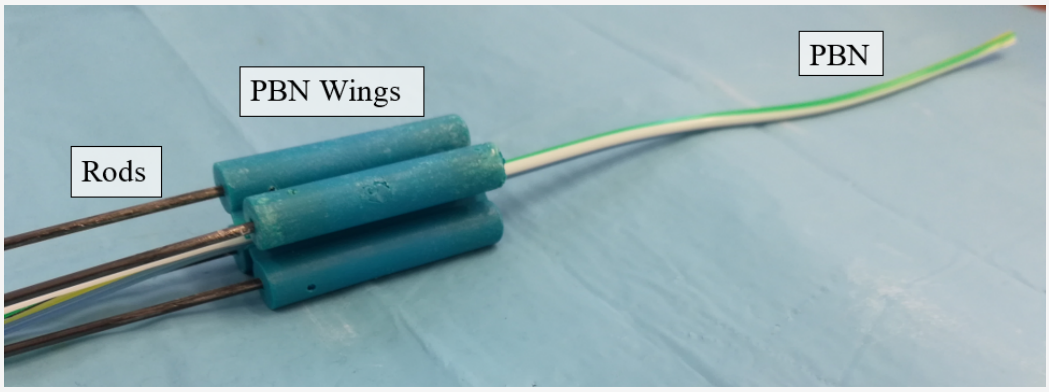

Figure 3.2: PBN wings and nitinol rods

Some of the advantages associated with the PBN design are as follows: (i) tissue deformation is decreased due to the reciprocal motion of the PBN segments [78], [70], (ii) PBNs can be made Magnetic resonance imaging (MRI) compatible, as was the one used in this study, (iii) PBNs can steer in full three dimensional (3D) space without the need for an axial rotation of the needle body [105], (iv) PBNs can be made from more compliant materials when compared to the kind of needles that require transmission of the torque from the base to the tip (as in the case of duty cycle spinning [7]), which leads to greater steering ability. With more compliant needle materials, follow-the-leader performance is also improved, as it is easier to maintain a suitable difference between needle and substrate stiffnesses to counteract the natural tendency for needle to straighten once it is bent.

The PBN used in the validation experiments in this study had a 15 MPa Young's modulus, was 2.5 mm in diameter, and was produced via extrusion (Xograph Healthcare Ltd. Gloucestershire, United Kingdom) of a medical-grade polymer (plasticised polyvinyl chloride) with 86 Shore "A" hardness. Nano-coating with Poly(para-xylylene) was applied to reduce the friction between the segments.

Detailed information about PBNs can be found in [124].

3.3 EM Sensor Setup

The EM sensor setup consisted of an EM field generator, EM sensors, and a processor. The field generated by the EM field generator was measured by the EM sensors. Then, the processor related the signals from the field generator and the sensors to estimate the 3D coordinates of the sensors [101].

The EM sensing system (NDI Aurora System, Ontario, Canada), is shown in figure 3.3, which included 4×⌀0.3 mm sensors with 5-Degree of Freedom (DoF), including the pitch, yaw, and position in 3 dimensions. The EM sensors were inserted into one of the lumens of the PBN segments in such a way that the sensors were placed at the segment tips. As per the manufacturer's specification, the root mean square error of the sensors was 0.7 mm in position and 0.2° in orientation.

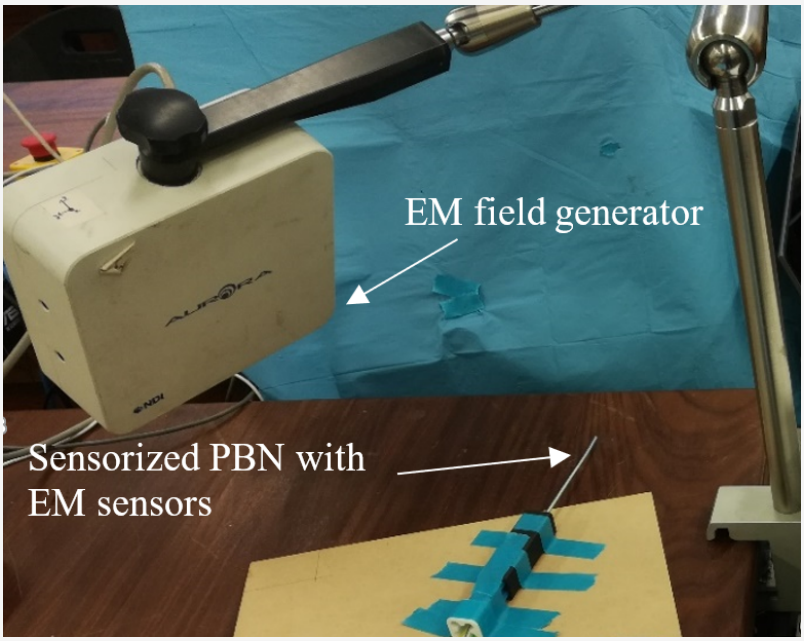

Figure 3.3: EM sensing setup with a sensorized PBN

The EM sensor wires were soldered to intermediary cables, which were connected to sensor interface units, while small currents induced inside of the sensors were digitised and amplified. Then, the signals were transmitted to the processor (figure 3.4 on the next page), which calcu-

lated the position and orientation of each sensor and controlled the EM field generator.

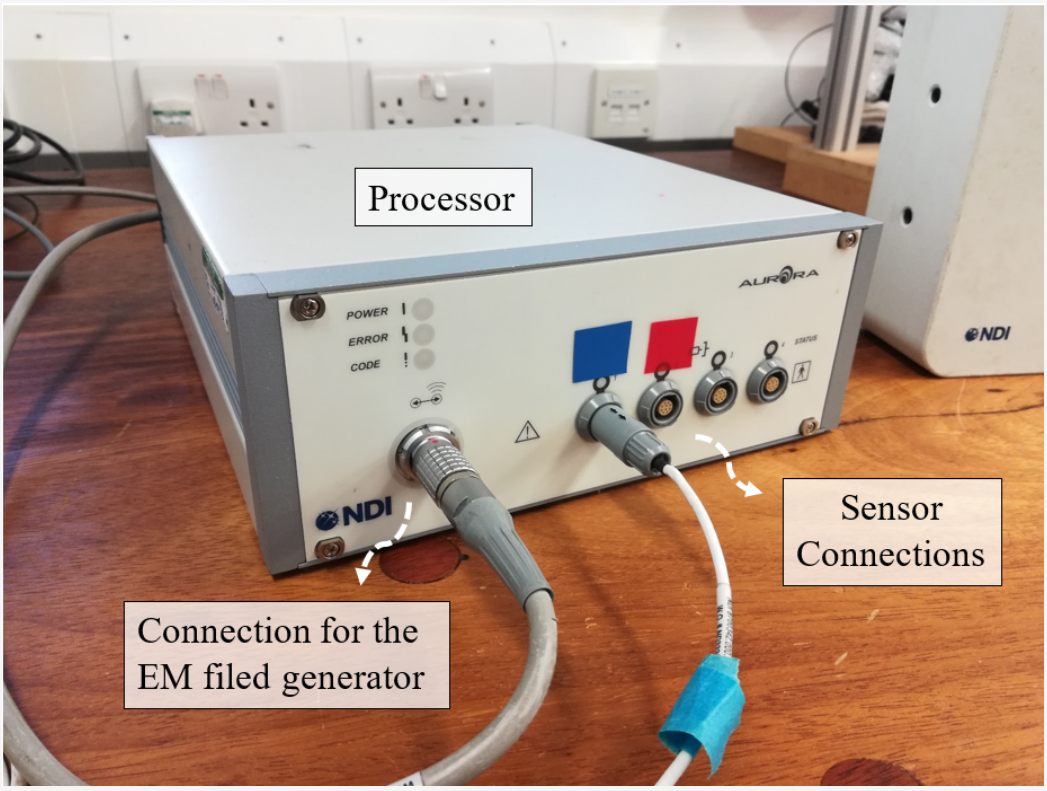

Figure 3.4: EM sensing processor

3.4 FBG Sensor Setup

In the validation experiments of the methods presented in Chapter 5 and Chapter 6, all of the segments of the PBN were instrumented with FBG-inscribed Multi-core Fibres (MCFs) (FBGS International NV, Geel, Belgium). The FBG-based shape sensing apparatus used in this study can be seen in figure 3.5. It consisted of four components:

- A four-channel optical spectrum interrogator
- A splitter box
- Four fanout boxes
- Four MCFs, each 195μm in diameter .

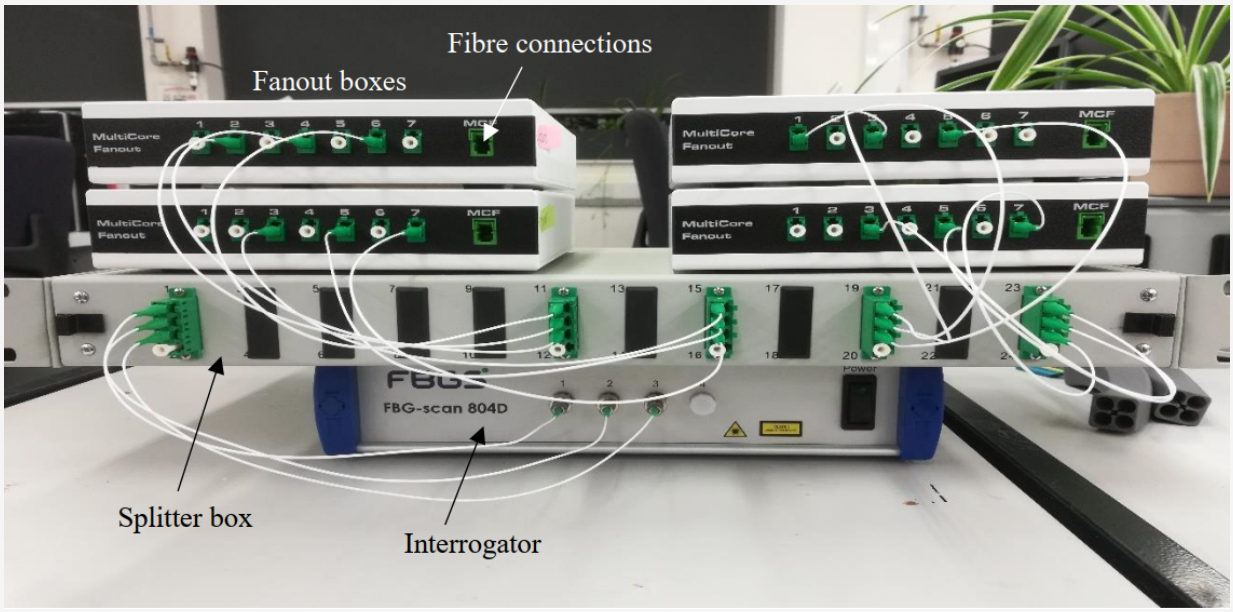

Figure 3.5: FBG-based shape sensing apparatus (fibres were not connected for the sake of clarity)

The 4-channel optical spectrum interrogator generated a light spectrum. The splitter box transmitted the light spectrum received from each channel of the interrogator to four fanout boxes, each of which was connected to one of the fibres. The fanout boxes received the light spectra from the four channels of the interrogator through the splitter box and transmit them

to the cores of the fibres. The interrogator was connected to a PC via a USB connection, and software for FBG wavelength acquisition was built in-house in MATLAB 2019b (MathWorks Inc., Natick, MA, USA).

The optical fibres (figure 3.6, figure 3.7 on the following page) were embedded within the working channels of the four segments of the needle. Each of the optical fibres had seven cores. However, only four of these seven cores were used, since the interrogator could generate a light spectrum for four channels. Moreover, the adjacent set of cores of the MCFs were used in this study for shape reconstruction due to their better signal quality with the cores at one half of the cross-section, as a result of the production method. The specifications of the MCFs are given in Table 3.1. The MCF cross-section and the cores used in the experiments in Chapter 5 and Chapter 6 are illustrated in figure 3.8. FBGs inscribed with the Draw Tower Gratings (DTG) method were chosen because fibres of relatively high strength are required in dynamic experiments [30].

These fibres were R&D products. Although three off-centred cores are enough for shape reconstruction, this six off-centred core design was a standard design of FBGS International at the time of the purchase. The reason why only four of the six off-centred cores were used is that the interrogator used in this study (figure 3.5 on the previous page) had only four channels. The smaller lumens of the PBN segments, which were with a diameter of 0.25 mm, were used to accommodate the 0.195 mm-outer-diameter MCFs.

To the best of author's knowledge, these 7-core fibres are not produced by the manufacturer anymore. The current standard is 3 off-centred cores with 120°separation.

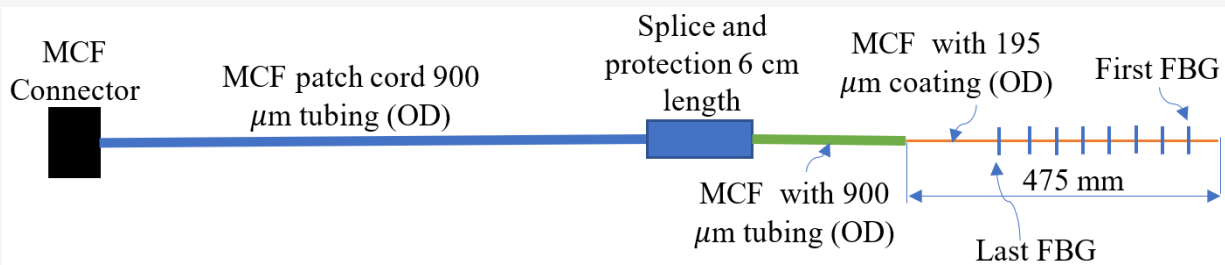

Figure 3.6: Schematic of an MCF - OD is short for outer diameter.

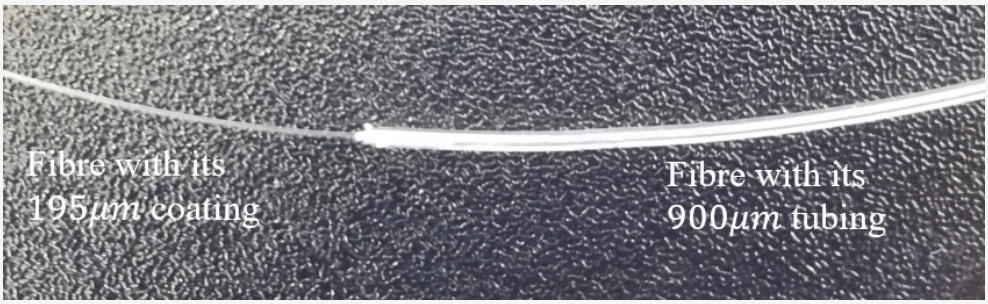

Figure 3.7: An MCF with its 900μm tubing

Table 3.1: MCF specifications - FBGS International NV (Geel, Belgium)

Production technique	DTG
Operating temperature	-20°C to 200°C
Wavelength configurations of the 4 MCFs	MCF 1: 1513.0nm - 1529.8nm MCF 2: 1532.2nm - 1549.0nm MCF 3: 1551.4nm - 1568.2nm MCF 4: 1570.6nm - 1587.4nm
Consecutive FBG Bragg-wavelength difference	2.4nm
Gage Factor $(1 - p_e)$	0.737
Interrogator model	FBGS FBG-scan 804D
Fiber coating	ORMOCER-T
FBG Refractive Index	3%
Number of cores	7 cores – 1 centered, 6 off-centered
Number of FBG sets	8
FBG length	5 mm
Consecutive FBG center to center distance	14 mm
Sensorized fiber length	103 mm

To enable repeated use of the FBG sets, it was necessary that the fibres could be removed easily. However, they also needed to be fixed to the segments during the insertion process. Therefore, a part was designed, and was 3D printed to fix the fibres to the corresponding segment bases, as shown in figure 3.9 on the following page, so that the fibre and the segment could be fixed with respect to each other by a pressure transmitted from a screw-driven plate.

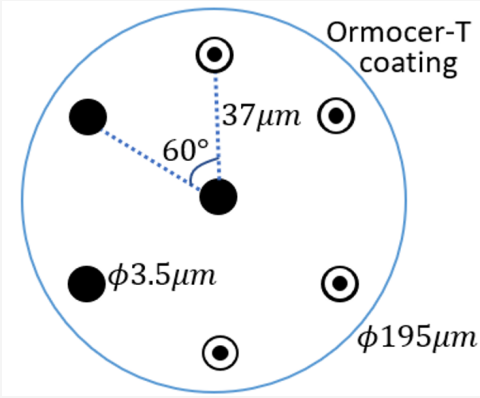

Figure 3.8: MCF cross-section including 1 centred and 6 off-centred cores. The 4 cores used in this study are marked with black and white circles.

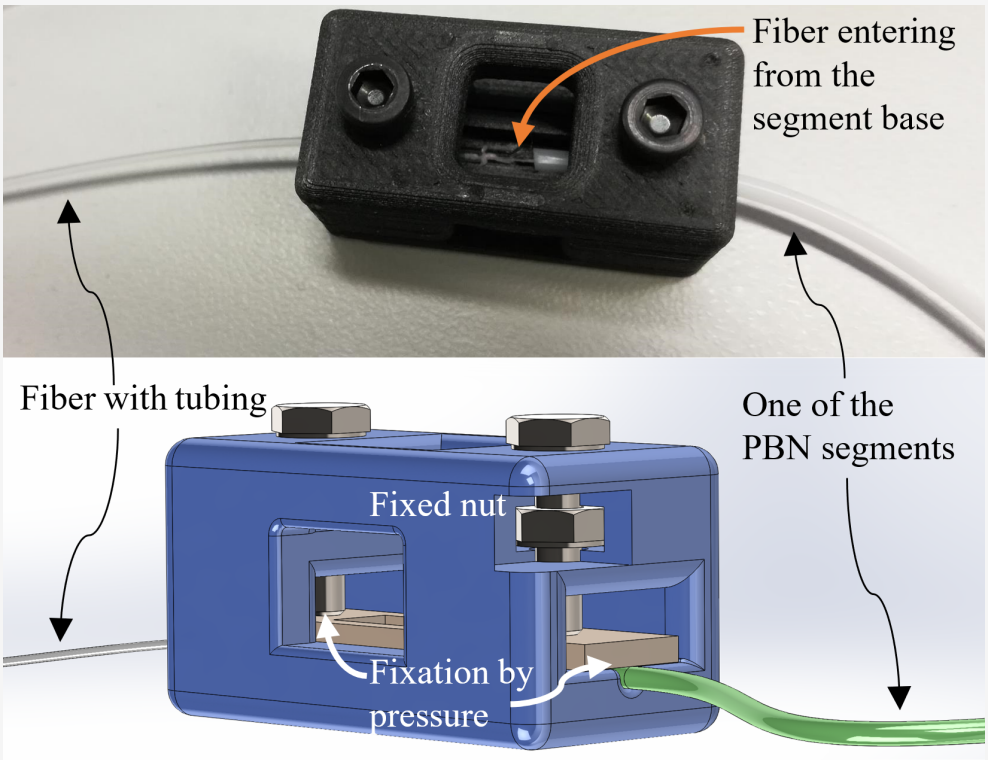

Figure 3.9: The 3D printed part fixing the fibres with PBN segment bases

3.5 Actuation Unit

For PBN actuation, an actuation unit (figure 3.10) consisting of 4 linear actuators,which was made previously by Dr Riccardo Secoli and Dr Vani Virdyawan in The Mechatronics in Medicine Laboratory was used in this study. Each of the linear actuators consisted of a 2 mm pitch lead screw and an EC20 Flat Maxon Motor (part number 351007), which was connected to a GP22A 19:1 reduction gearbox and driven by a EPOS2 24/2 motor driver. The rotation of the lead screws by the motors resulted in the movements of the carriages attached to the lead screws. Therefore, each of the 4 segments could be independently driven via a nitinol rod, which was connected to one of the carriages on one end and the corresponding segment wing (figure 3.2 on page 58) on the other end. The actuation unit also included encoders (HEDR-55L2-BP07, Broadcom Inc.), which were connected to the lead screw shaft and used to determine the actual navigation length of each segment.

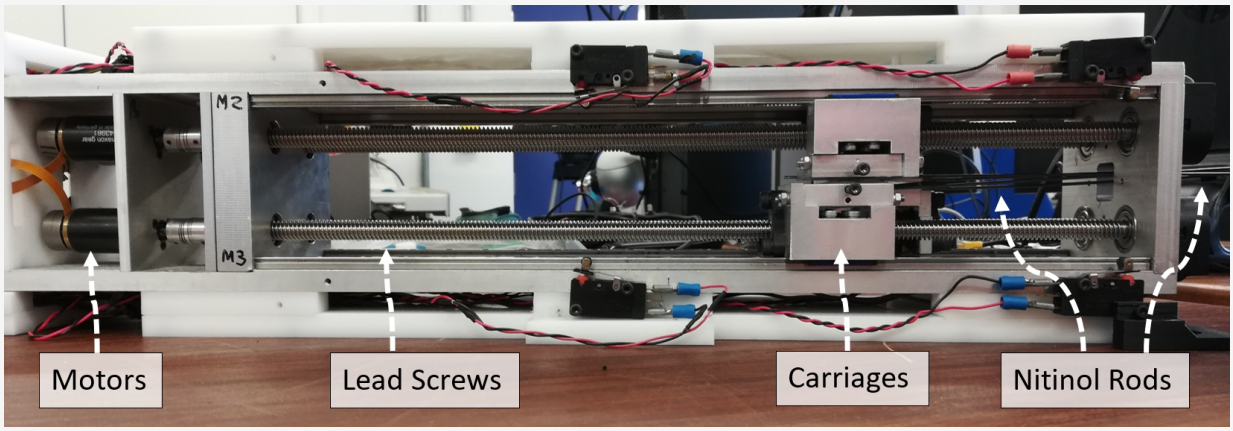

Figure 3.10: Actuation unit used for PBN actuation

Work done within this thesis: Actuation software that included higher-level motion commands for a 4-segment PBN was built in-house in MATLAB 2019b (MathWorks Inc.) on an EPOS2 library developed for single motor actuation [128]. Additional parts to combine the instrumented PBN with the actuation box were designed and then 3D printed, as shown in figure 3.11 on page 67. The function of these parts was to drive the PBN smoothly into a soft medium. The rail-like attachments, in which the segment-fibre connections could slide, as seen

in figure 3.11 on the following page, were to minimise the torsion of the instrumented PBN segments, which decreased the noise on the FBG signal. The CAD models of the assembled parts are also shown in figure 3.12 on page 68 for clarity. Moreover, two half-circular guides were designed to guide the PBN segments exactly to the centre channel of the trocar core, which was essential to prevent them from getting stuck during insertion. The trocar core had 4 outer circular channels to guide the PBN wings. Additionally, a curved part was designed for FBG calibration (figure 3.13 on page 69). This part could be attached to the other parts, as seen in the photo, and could be placed in 4 main directions (upward, rightward, downward, leftward), which was required in the calibration (Chapter 5.4.5).

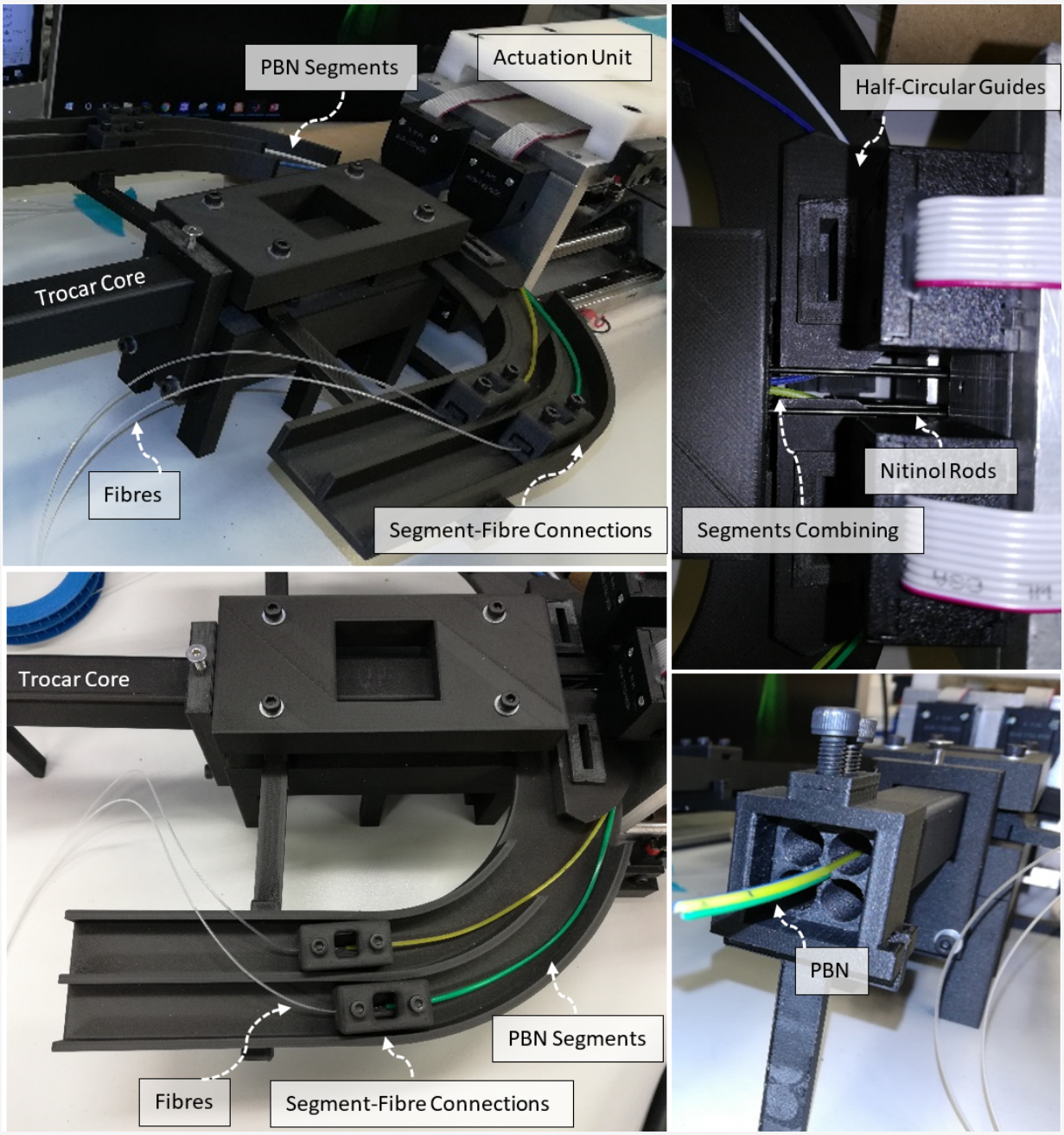

Figure 3.11: 3D parts designed for the integration of instrumented PBN and the actuation box

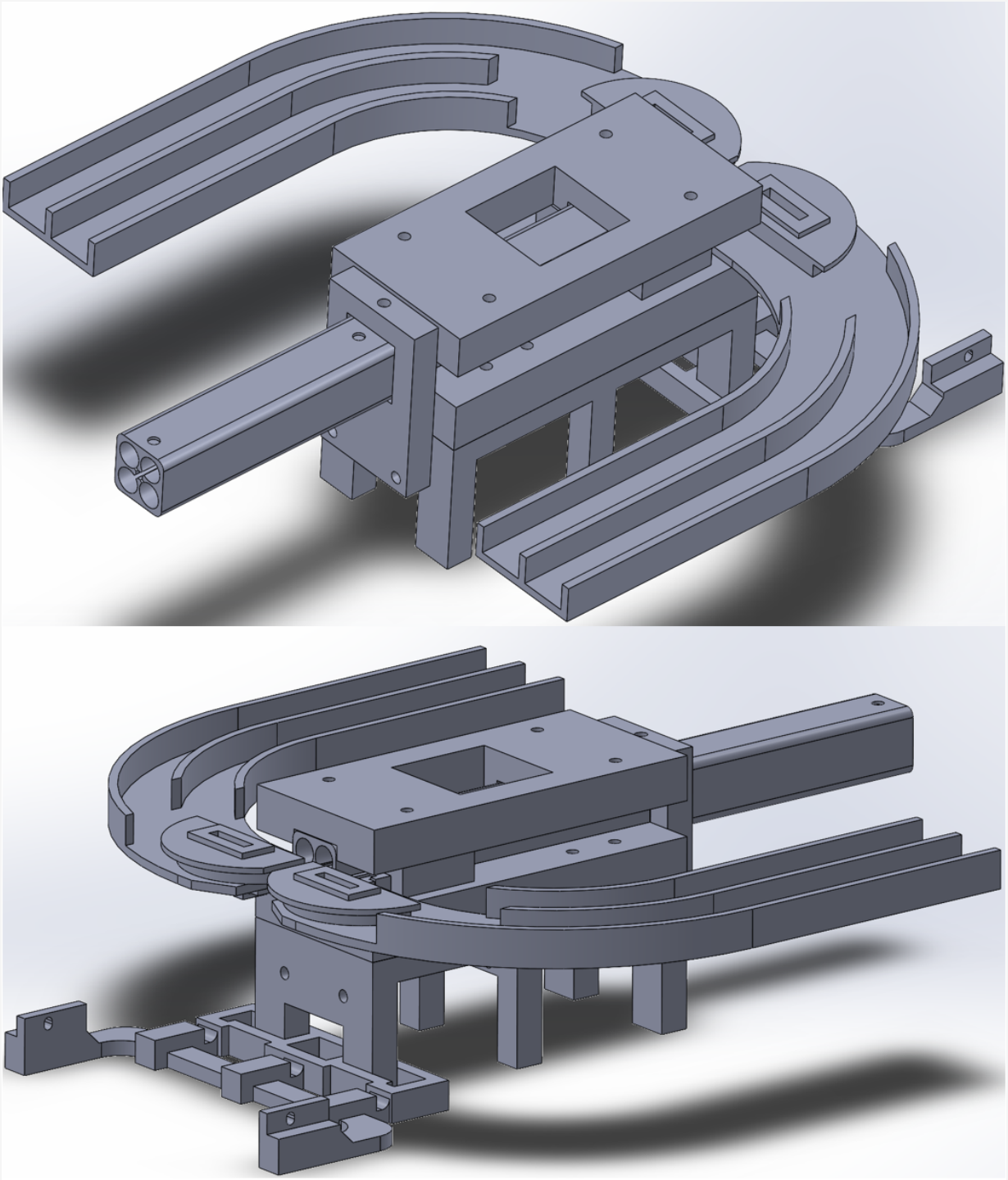

Figure 3.12: CAD models of the parts designed for the integration of the instrumented PBN and the actuation box

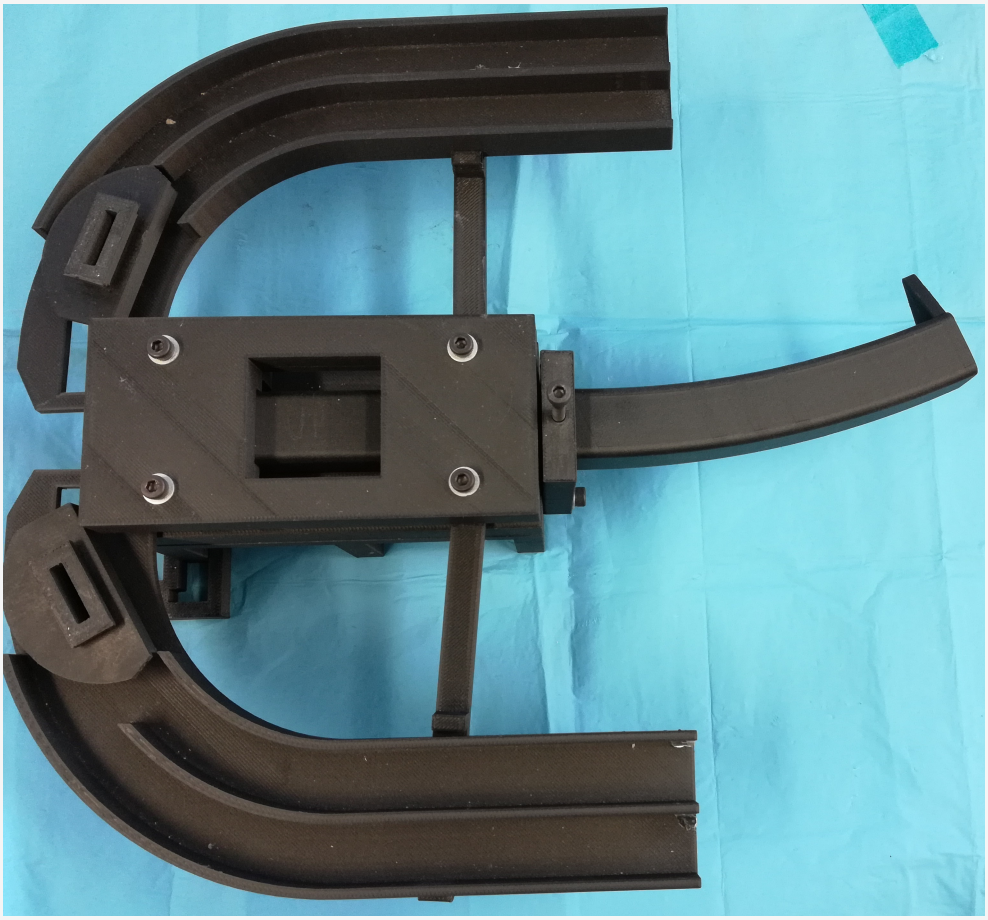

Figure 3.13: The curved guide designed for FBG calibration

3.6 Graphical User Interface

A GUI was developed to ease the simulation and control of the PBN. The developed actuation software and the PBN tissue interaction model presented in [105] were integrated with the GUI (figure 3.14 on page 72) to drive the PBN segments by showing the shape reconstruction online and simulate the PBN navigation, respectively. The simulation of the PBN navigation was used extensively at the early stages of the path-following controller presented in Section 6. In order to satisfy the PBN permissibility condition [124], which was necessary for the PBN to act as a single body at all times, the GUI was programmed in such a way that it blocked the movement commands breaching the condition. The other functionalities that could be performed using the GUI were as follows:

- Single, couple, and all forward segment movements (simulation and/or in reality),
- Single backward segment movements (simulation and/or in reality),
- Warning the user if the commands were not permissible,
- Showing the individual segment shapes and the overall needle (normal and zoom-out to show the entire ground-truth path),
- Saving the command history,
- Saving the current PBN state,
- Loading a command history that was previously saved to rerun,
- Loading a PBN state that was previously saved,
- Showing the current encoder values of the segments (the distances that the segments were pushed),
- Setting the torsion value for the representation of the undesired torsion occurring during navigation in heterogeneous tissue,
- Setting the distance between the reconstructed curve points,

- Showing and hiding the task frame history,
- Stopping the needle navigation in case of an emergency,
- Navigation with the developed path-following controller

The buttons on the GUI were mainly for quick manual control. More complex and simultaneous movements of the segments could be performed when navigating with the developed controller. The GUI was developed in MATLAB 2019b (MathWorks Inc.).

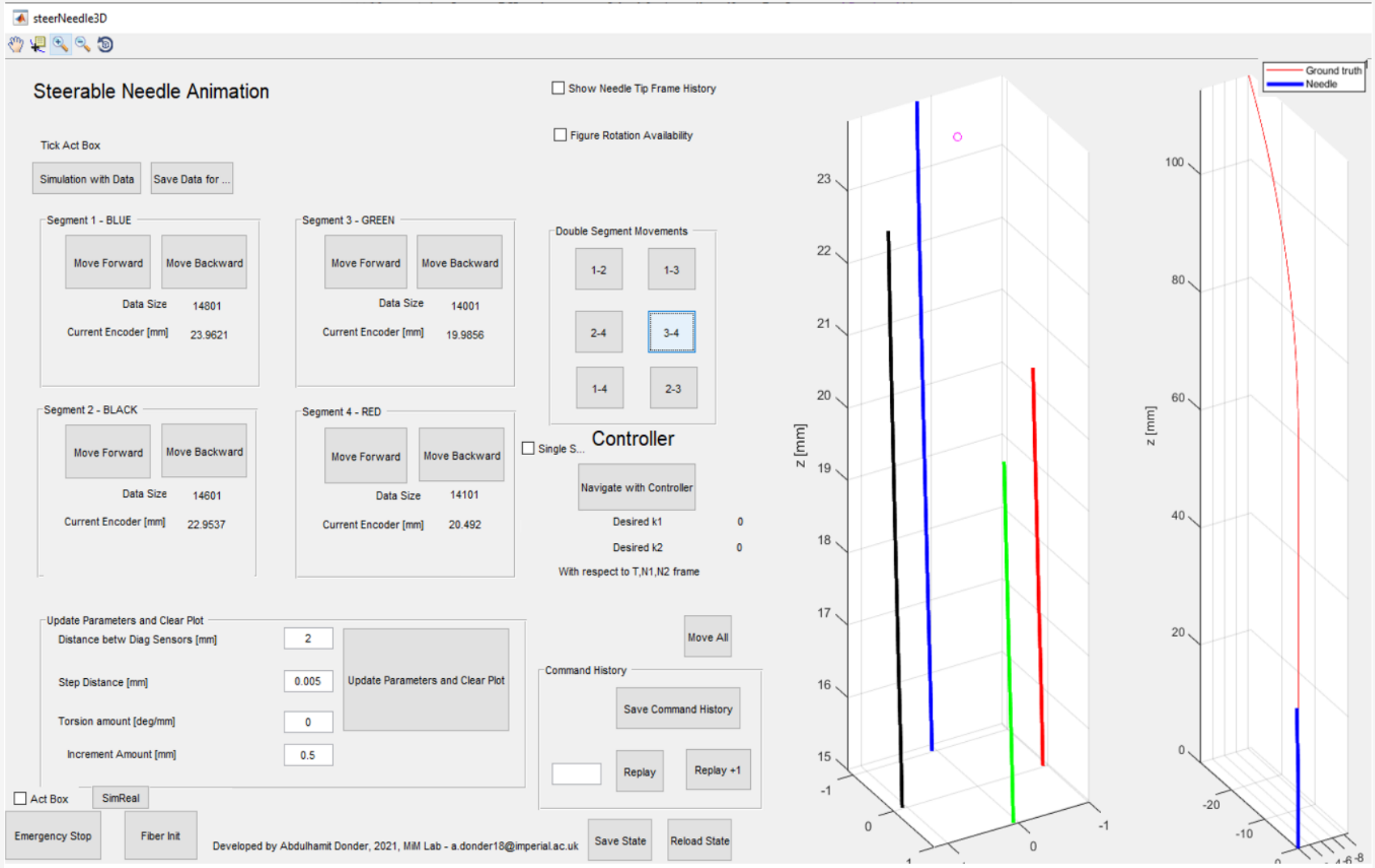

Figure 3.14: The GUI

3.7 Conclusion

In this chapter, the experimental system including the GUI developed to run the actuation and sensing software, was introduced. The work made in the scope of this thesis was clearly stated and distinguished from that in previous studies. This system now, offers a complete setup that can be used to run an automated controller and for manual testing. FBG calibration can also be made and both of the sensing modalities (EM and FBG) can be used simultaneously for comparison.

The PBN presented in this chapter was used in all of the experiments in this thesis. The EM setup was used in the study given in Chapter 4 for PBN tip tracking and in Chapter 5 as ground truth in the validation experiments of the FBG-based sensing. The FBG sensor setup was used in the experiments given in Chapter 5 to validate the FBG-based shape reconstruction algorithm and in Chapter 6 to provide feedback for the closed-loop path-following controller. The GUI was used to simulate the navigation of the PBN at the early stages of the path-following controller presented in Chapter 6 and to conduct the experiments given in the same chapter and Chapter 5. Finally, the actuation unit was used to test the sensing and control methods presented in Chapter 5 and Chapter 6.

Chapter 4

Electromagnetic Pose Estimation for a Programmable Bevel-Tip Steerable Needle

4.1 Introduction

Since steering in a desired direction is achieved by actuating particular Programmable Bevel Tip Steerable Needle (PBN) segments, the position and orientation of each segment (i.e. the pose) are required in order to ensure that the correct segment is actuated. Although the axial displacement of the segments is known from the actuator encoders, it is not possible to know the full pose of the needle tip due to undesired torsion and flexion occurring during navigation through heterogeneous tissue. This problem grows as the segment tips move away from each other. The direction of the PBN steering depends on the non-linear combination of the relative offsets between the PBN segment tips, thus the direction of the Leading Segment (LS) is not sufficient to provide the real direction of steering, and the knowledge of the PBN tip full pose has vital importance in creating correct curvatures when considering the undesired torsion during insertion. Ideally, 6-Degree of Freedom (DoF) sensors would be embedded in each segment to estimate the full pose, but to the best knowledge of the author, no 6 DoF sensor of 0.3 mm outer diameter (diameter of the PBN lumens) is commercially available.

Consequently a novel algorithm which estimates the full pose of the PBN tip, on the basis of four 5 DoF sensors, missing roll, embedded one in each segment, is presented along with a set

of trials, which validate its performance under controlled conditions. The detailed explanation of the proposed algorithm is given in this chapter.

4.1.1 Publications

This chapter is from an edited version of the below article, which is under revision (major revisions):

- Secoli, R., Matheson, E. W., Pinzi, M., Galvan, S., Watts, T. E., **Donder, A.**, Rodriguez y Baena, F. - A Modular Robotic Platform for Precision Neurosurgery with a PBN. Submitted to IEEE Transactions on Robotics [106]

This paper presents the design and the first ex vivo assessment of the surgical workflow of the An Enhanced Delivery Ecosystem for Neurosurgery in 2020 (EDEN2020) project's robotic platform. It includes an explanation about robotic driver and Low-Level Controller (LLC) for PBNs, haptic master for the manual control of the PBN, Electromagnetic (EM)-based full-pose reconstruction for PBNs, visual front-end interface, a PBN model for curvature estimation, and *ex vivo* experimental methods and results.

The novel EM-based PBN tracking method and experimental methods to validate this algorithm are my own and presented in this chapter of the thesis.

4.2 Tip Pose Reconstruction

This section describes the PBN tip full pose estimation algorithm, which fuses 5-DoF poses provided by the sensing embedded within the tips of the 4-segment-PBN. The variables and notation used in this section are given in Table 4.1:

To simplify the notation, time dependencies and the arc-length parameter are omitted, as well as the reference frame which is the inertial frame of the needle for the entire procedure.

Because of the longitudinal offset, c, between the sensors and the segment tips, as shown in figure 4.1, $\boldsymbol{p'}_i \in \mathbb{R}^3, i \in \{1, 2, 3, 4\}$ is used to indicate the position vectors of the segment tips, whereas $\boldsymbol{p}_i \in \mathbb{R}^3$ is used for the position vectors of the sensors. Firstly, the method to estimate the position $\boldsymbol{p}_T \in \mathbb{R}^3$ of the PBN tip without taking c into account is presented. Then, essentially, this value will be extrapolated by the offset c in the direction of the PBN orientation vector to estimate the actual tip position, $\boldsymbol{p'}_T \in \mathbb{R}^3$. It is assumed that no local twist occurs over the length of this offset.

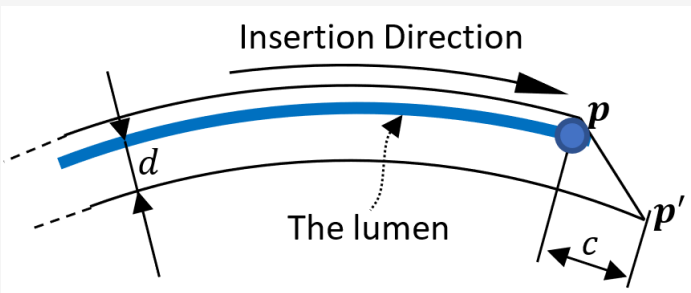

Figure 4.1: Illustration of a single segment of a PBN. c represents the longitudinal offset between the sensor position, $\boldsymbol{p}$, and the segment tip, $\boldsymbol{p'}$

The other assumptions for the tip pose reconstruction are as follows:

1. Each of the 4 sensors, $S_i, i \in \{1, 2, 3, 4\}$ provide 5-DoF pose information: three dimensional (3D) position and orientations about the sensors' pitch and yaw axes.
2. Each sensor embedded in a segment is bonded with the segment body.
3. Each sensor is located at the tip of the segment lumens, as shown in figure 4.1.

Table 4.1: The variables and notation used in EM-based tip pose reconstruction algorithm

c:	The longitudinal offset as shown in figure 4.1 on the preceding page
d:	The nominal lateral distance between the PBN tip and the LS tip shown in figure 4.4 on page 83, figure 4.1 on the preceding page and defined in Algorithm 3
D:	The direction: clockwise or anti-clockwise shown in figure 4.6 on page 87
ϵ:	The weight threshold, which is determined empirically
φ_i:	The angle between $\boldsymbol{v}_i$ and $\boldsymbol{v}_T$
l_1, l_2:	The distances shown in Figures 4.4-4.5 and defined in Algorithms 3,6
$\boldsymbol{p}_D, \boldsymbol{p}_L, \boldsymbol{p}_T, \boldsymbol{p'}_T$:	The sensor position vectors of the Diagonal Segment (DS), the LS, and the PBN tip with and without taking the offset c into account
$\boldsymbol{p}_i, \boldsymbol{p}_j$:	The position vectors of the sensors at the segment tips, where $i, j \in \{1, 2, 3, 4\}$
$\boldsymbol{p}_{k1}, \boldsymbol{p}_{k2}$:	The position of the auxiliary points shown in figure 4.4 on page 83, 4.5 and defined in Algorithms 3 and 6
$\boldsymbol{p}_U, \boldsymbol{p}_{Up}, \boldsymbol{p}_T$:	The position of the points shown in figure 4.5 on page 85
plane P:	The plane which is created by $\boldsymbol{v}_L$ and $\boldsymbol{p}_D$
plane K:	The plane which is passing through $\boldsymbol{p}_T$ and normal to $\boldsymbol{v}_T$
$\boldsymbol{q}_i$,$\boldsymbol{q}_{Tip}$:	The orientation of S_i and PBN tip in unit quaternions
$\boldsymbol{R}_{Tip}$:	The PBN-tip-fixed frame transformation matrix as defined in 4.4
S_i:	i^{th} sensor as shown in figure 4.2 on page 79
$\boldsymbol{t}_2$,$\boldsymbol{t}_3$,$\boldsymbol{t}_4$:	Vectors from the position of S_1 to the positions of T_2, T_3, T_4, respectively
T_2,T_3,T_4:	Temporary sensor labels as shown in figure 4.3 on page 81
$\boldsymbol{u}_1$,$\boldsymbol{u}_2$,$\boldsymbol{u}_3$:	The basis vectors of the PBN-tip-fixed reference frame as defined in Algorithm 7 and shown in figure 4.6 on page 87
$\boldsymbol{v}_L, \boldsymbol{v}_T, \boldsymbol{v}_i$:	The orientation unit vectors of the LS tip, the PBN tip, and S_i tip
$\boldsymbol{v}_{ij}$:	The vectors as defined in Algorithm 2
W_1, W_2:	The weights as defined in Algorithm 4

4. The PBN's bending angle from the DS tip (the segment which is not one of the segments adjacent to the LS) to the LS tip is constant. Therefore, the tip of the DS navigates on the plane, P, which is created by the unit LS orientation vector, $\boldsymbol{v}_L \in \mathbb{R}^3$, and the DS tip, $\boldsymbol{p}_D \in \mathbb{R}^3$. This assumption also enforces no torsion along the same region, which is

considered acceptable based on [124].

5. The unit orientation vector of the PBN tip, $\boldsymbol{v}_T \in \mathbb{R}^3$, is the same as that of the LS, $\boldsymbol{v}_L$.

As long as these assumptions are satisfied, there is no constraint regarding the segments other than LS and DS.

4.2.1 Data Acquisition

Sensor S_i provides a 5-DoF pose: a position vector, $\boldsymbol{p}_i \in \mathbb{R}^3$ and a quaternion for the orientation, $\boldsymbol{q}_i = [q_w \; q_x \; q_y \; q_z] \in \mathbb{R}^4$. The q_z component is always set to 0, which indicates that no rotation is measurable about the local longitudinal axis, 3rd basis axis, i.e. the direction of sensor orientation. Therefore the unit orientation vector, $\boldsymbol{v}_i \in \mathbb{R}^3$, of the ith sensor with respect to the inertial frame is obtained as follows:

$$\boldsymbol{v}_i = \begin{bmatrix} 2(q_x q_z + q_w q_y) \\ 2(q_y q_z - q_w q_x) \\ q_w^2 - q_x^2 - q_y^2 + q_z^2 \end{bmatrix} \tag{4.1}$$

4.2.2 Segment Labelling

The full pose computation algorithm assumes that the configuration of the segments is as shown in figure 4.2 on the next page. Therefore, a labelling method has been developed to label the sensors accordingly. In this method, the sensors are not required to be perfectly aligned or at the same plane.

First step of the method is selection of one of the sensors and labelling it as S_1. Secondly, other sensors are labelled randomly and temporarily as T_2, T_3, T_4. Thirdly, three vectors from the position of S_1 to the positions of T_2, T_3, T_4 are created and named $\boldsymbol{t}_2$, $\boldsymbol{t}_3$, $\boldsymbol{t}_4$ as shown in figure 4.3 on page 81.

The main idea is cross multiplying the created vectors in pairs and comparing the direction of resulting vector with the direction of S_1, $\boldsymbol{v}_1$, which is obtained from the corresponding sensor. For this comparison, dot product is applied. If the resulting vector and $\boldsymbol{v}_1$ are showing the

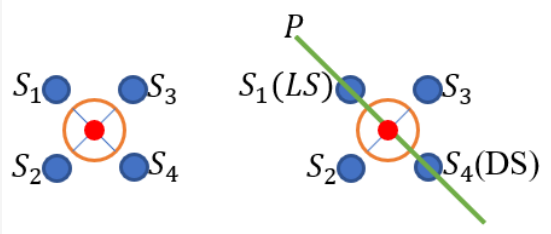

Figure 4.2: Segment configuration assumed by the full pose estimation algorithm. Left: S_i, with $i \in \{1, 2, 3, 4\}$ represent the 4 sensors. Circle with cross denotes the insertion direction of the segments. Red smaller circle in the middle denotes $\boldsymbol{p}_T$. Right: Cross-section illustration of LS, DS and plane P. Assuming that LS corresponds to S_1, the diagonal segment, DS, is assigned to S_4, and the plane which is created with the LS tip orientation vector and the DS tip position is assigned as plane P

same direction, then the result of their dot product becomes positive and vice versa. Therefore, whether a sensor is at the clockwise side of another sensor with respect to the catheter centre, starting from S_1 is determined by the sign of the dot product result. The sensor which is at the most clockwise side with respect to the catheter centre, starting from S_1 should be labelled as S_2, the previous one S_4 then S_3 as shown in figure 4.2.

With the light of the explanation above, let T_3 be at the clockwise side of T_2 with respect to the catheter centre, starting from S_1 as in figure 4.3 on page 81, then;

$$(\boldsymbol{t}_2 \times \boldsymbol{t}_3) \cdot \boldsymbol{v}_1 > 0 \tag{4.2}$$

Let T_4 be at the clockwise side of T_3, as in figure 4.3 on page 81, then;

$$(\boldsymbol{t}_3 \times \boldsymbol{t}_4) \cdot \boldsymbol{v}_1 > 0 \tag{4.3}$$

Therefore, T_4 is labelled as S_2 and T_2, T_3 are labelled as S_3, S_4 respectively, as shown in figure 4.2.

This section can be implemented using Algorithm 1.

Algorithm 1 Segment Labelling

Input: 5-DoF pose information of the 4 segment tips

Output: Position and orientation vectors of the 4 sensors at the segment tips: $\boldsymbol{p}_i$, $\boldsymbol{v}_i$ with $i \in \{1, 2, 3, 4\}$

```
Random sensor naming (T_2, T_3, T_4)
t_2 ← Vector from T_2 to S_1
t_3 ← Vector from T_3 to S_1
t_4 ← Vector from T_4 to S_1
if (t_2 × t_3) · v_1 > 0 then
    if (t_3 × t_4) · v_1 > 0 then
        S_2 ← T_4
    else
        S_2 ← T_3
    end if
else
    if (t_2 × t_4) · v_1 > 0 then
        S_2 ← T_4
    else
        S_2 ← T_2
    end if
end if
if S_2 = T_4 then
    if (t_2 × t_3) · v_1 > 0 then
        S_3 ← T_2
        S_4 ← T_3
    else
        S_3 ← T_3
        S_4 ← T_2
    end if
else if S_2 = T_3 then
    if (t_2 × t_4) · v_1 > 0 then
        S_3 ← T_2
        S_4 ← T_4
    else
        S_3 ← T_4
        S_4 ← T_2
    end if
else if S_2 = T_2 then
    if (t_3 × t_4) · v_1 > 0 then
        S_3 ← T_3
        S_4 ← T_4
    else
        S_3 ← T_4
        S_4 ← T_3
    end if
end if
p_i ← position vector of S_i
v_i ← orientation vector of S_i
```

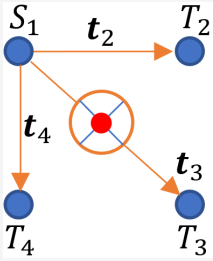

Figure 4.3: Arbitrary sensor labelling for the segment labelling algorithm Circle with cross denotes the insertion direction of the segments.

4.2.3 Definition of the LS

As per [124], a path dependent discrepancy is expected between the distal and proximal offsets of the PBN segments because of the separation between the neutral axes of them. Therefore, it is proposed to determine the LS by using the sensory information at the distal end, instead of the encoders at the proximal end. The steps to define the LS is given in Algorithm 2.

4.2.4 Estimation of the PBN tip translational coordinates

Once the plane P is defined, $\boldsymbol{p}_T$ can be determined following Algorithm 3, which is depicted graphically in figure 4.4 on page 83. Parameter d, shown in figure 4.1 on page 76, is defined as the radius of the circle made up by the sensor positions in the case where all the segments are aligned. This is known from the design, and is the nominal distance between $\boldsymbol{p}_T$ and $\boldsymbol{p}_L$, which for the catheter considered in this work is 0.80 mm.

4.2.5 Estimation of the PBN tip rotational coordinates

To define the PBN tip rotational coordinates, the PBN-tip-fixed reference frame is created. The contributions of the sensors other than the ones at LS tip and the DS tip depend on the weights which are determined according to the distance between the sensor and $\boldsymbol{p}_T$ (the weight corresponding to LS and DS is always taken as 1). Because of the correlation of this distance with the angle between $\boldsymbol{v}_L$ and the sensor's orientation vector, this angle is used in the determination of the weights, as shown in Algorithm 4. Note that the weights are not normalised, i.e. while the weight corresponding to LS and DS is 1, the weight corresponding

Algorithm 2 LS Definition

Input: Position and orientation vectors of the 4 sensors at the segment tips: $\boldsymbol{p}_i$, $\boldsymbol{v}_i$ with $i \in \{1, 2, 3, 4\}$

Output: LS tip unit orientation and position vectors: $\boldsymbol{v}_L \in \mathbb{R}^3$, $\boldsymbol{p}_L \in \mathbb{R}^3$

```
1:  v_ij = p_j − p_i        j ∈ {1, 2, 3, 4}
2:  if (v_21 · v_1) > 0 then
3:     if (v_31 · v_1) > 0 then
4:        if (v_41 · v_1) > 0 then
5:           v_L ← v_1  &  p_L ← p_1
6:        else
7:           v_L ← v_4  &  p_L ← p_4
8:        end if
9:     else
10:       if (v_43 · v_3) > 0 then
11:          v_L ← v_3  &  p_L ← p_3
12:       else
13:          v_L ← v_4  &  p_L ← p_4
14:       end if
15:    end if
16: else
17:    if (v_32 · v_2) > 0 then
18:       if (v_42 · v_2) > 0 then
19:          v_L ← v_2  &  p_L ← p_2
20:       else
21:          v_L ← v_4  &  p_L ← p_4
22:       end if
23:    else
24:       if (v_43 · v_3) > 0 then
25:          v_L ← v_3  &  p_L ← p_3
26:       else
27:          v_L ← v_4  &  p_L ← p_4
28:       end if
29:    end if
30: end if
```

to the other segments is defined between $[0, 1]$.

The first step in the method is determining the angles $\varphi_i \in \mathbb{R}_{\geq 0}$ with $i \in \{1, 2, 3, 4\}$ between $\boldsymbol{v}_i$, and $\boldsymbol{v}_T$, which is assumed to be the same as $\boldsymbol{v}_L$. It is known that S_1 and S_4, and S_2 and S_3 are diagonal to each other as shown in figure 4.2 on page 79. The sensor with the smaller φ is selected from each diagonal couple and the weights are calculated as given in Algorithm 4, where the threshold, $\epsilon \in \mathbb{R}_{\geq 0}$, is determined empirically. Note that this algorithm outputs the

Algorithm 3 Estimation of PBN tip translational coordinates

Input: Position vectors of the sensors at LS tip and DS tip: $\boldsymbol{p}_L$, $\boldsymbol{p}_D \in \mathbb{R}^3$, LS tip unit orientation vector $\boldsymbol{v}_L$

Output: PBN tip position vectors with and without considering the offset c shown in figure 4.1 on page 76: $\boldsymbol{p}_T, \boldsymbol{p'}_T \in \mathbb{R}^3$

1: $d \leftarrow$ the nominal distance between the LS tip and the PBN tip
2: $\boldsymbol{e}_1 = \boldsymbol{p}_L - \boldsymbol{p}_D$
3: $\alpha_1 = \cos^{-1}((\boldsymbol{e}_1 \cdot \boldsymbol{v}_L)/(\|\boldsymbol{e}_1\| \, \|\boldsymbol{v}_L\|))$
4: $l_1 = \|\boldsymbol{e}_1\| \cos(\alpha)$
5: $\boldsymbol{p}_{k1} = \boldsymbol{p}_L - l_1 \boldsymbol{v}_L$
6: $\boldsymbol{h}_1 = \boldsymbol{p}_D - \boldsymbol{p}_{k1}$
7: $\boldsymbol{p}_T = \boldsymbol{p}_L + d(\boldsymbol{h}_1 / \|\boldsymbol{h}_1\|)$
8: $\boldsymbol{p'}_T = \boldsymbol{p}_T + c \, \boldsymbol{v}_L$

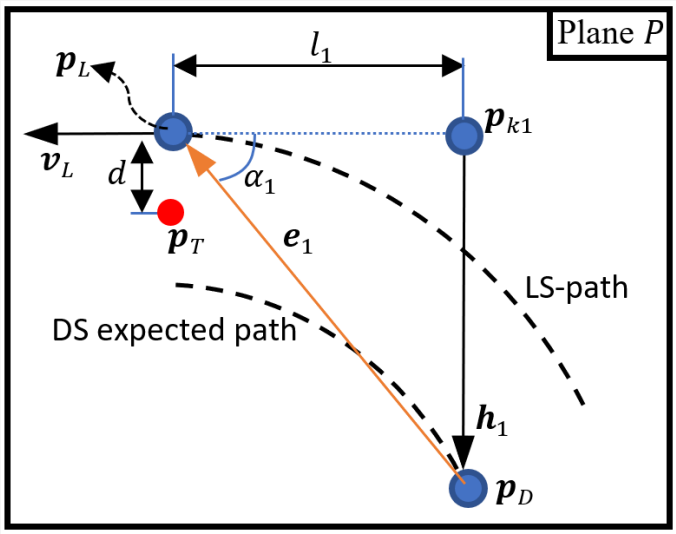

Figure 4.4: Illustration of the vectors and distances used in the estimation of the PBN tip translational coordinates. $\boldsymbol{p}_L$, $\boldsymbol{p}_D$ represents the tip position vectors of the sensors at LS tip and DS tip. $\boldsymbol{p}_T$ is the PBN tip without taking the offset c into account. $\boldsymbol{v}_L$ is the unit vector showing the orientation of the LS tip. $\boldsymbol{e}_1$, l_1, α_1, and $\boldsymbol{h}_1$ are as shown. $\boldsymbol{p}_{k1}$ is the position vector of the shown auxiliary intersection point. d is the distance between the LS tip and the PBN tip. Note that the sensors other than the ones at LS and DS are not shown because this illustration is limited to plane P, which is created with the LS orientation vector, $\boldsymbol{v}_L$, and $\boldsymbol{p}_D$

weight corresponding to LS as 1.

In the following steps, the base vector, $\boldsymbol{b} \in \mathbb{R}^3$ and the auxiliary vector $\boldsymbol{a} \in \mathbb{R}^3$ are defined, which are used to place the PBN-tip-fixed reference frame's 1st and 2nd basis vectors that are perpendicular to $\boldsymbol{v}_T$, i.e. the 3rd basis vector.

Algorithm 4 Catheter Tip Frame Weight Definition

Input: PBN tip unit orientation vector: $\boldsymbol{v}_T$, the weight threshold: $\epsilon \in \mathbb{R}_{\geq 0}$, and the unit orientation vectors of the segment tips: $\boldsymbol{v}_i \in \mathbb{R}^3, i \in \{1, 2, 3, 4\}$

Output: The weights corresponding to S_1 and S_4, and S_2 and S_3: W_1, W_2, The angles between $\boldsymbol{v}_T$ and $\boldsymbol{v}_i$: $\varphi_i \in \mathbb{R}_{\geq 0}$

```
1: φ_i = cos^{-1}((v_T · v_i)/(||v_T|| ||v_i||))
2: if min(φ_1, φ_4) > ε then
3:     W_1 = 0
4: else
5:     W_1 = 1 − ε^{-1} min(φ_1, φ_4)
6: end if
7: if min(φ_2, φ_3) > ε then
8:     W_2 = 0
9: else
10:    W_2 = 1 − ε^{-1} min(φ_2, φ_3)
11: end if
```

The base vector, $\boldsymbol{b}$ is determined with Algorithm 5. Note that always the vectors towards S_1 and S_2 are preferred in the calculation of $\boldsymbol{b}$ for the sake of consistency.

Algorithm 5 Base Vector Calculation

Input: The position vectors of the PBN tip, and sensor at the LS tip, S_1, S_2: $\boldsymbol{p}_T, \boldsymbol{p}_L, \boldsymbol{p}_i \in \mathbb{R}^3, i \in \{1, 2\}$

Output: The base vector: $\boldsymbol{b} \in \mathbb{R}^3$

```
1: if p_L = p_1 or p_L = p_2 then
2:     b = p_L − p_T
3: else
4:     b = p_T − p_L
5: end if
```

Subsequently, the sensor with smaller φ from the diagonal couple excluding LS is projected onto plane K, passing through $\boldsymbol{p}_T$ and normal to $\boldsymbol{v}_T$. The position vector of this sensor is shown with $\boldsymbol{p}_U \in \mathbb{R}^3$ and the position vector of the projection is shown with $\boldsymbol{p}_{Up} \in \mathbb{R}^3$. Afterwards the unit vector, $\boldsymbol{a}$, from $\boldsymbol{p}_T$ towards this projection is estimated if the corresponding weight is not 0, i.e. the corresponding diagonal couple is so behind the LS as not to be considered for the PBN-tip-frame calculation. Note that if the corresponding weight is 0, $\boldsymbol{a}$ is not calculated and not used in Algorithm 7, where the PBN-tip-fixed reference frame is calculated. Also, note that since one of the weights has to be 1 (the one corresponding to the LS), the condition to calculate $\boldsymbol{a}$ is defined as: if $W_1 \neq 0$ & $W_2 \neq 0$. Similar to the case in $\boldsymbol{b}$, the vectors towards

S_1 and S_2 are always used when determining $\boldsymbol{a}$ for the sake of consistency. Therefore, in the case of $\boldsymbol{a}$ being towards S_3 or S_4, it is reverted. This algorithm is given in Algorithm 6. The vectors and distances used are illustrated in figure 4.5.

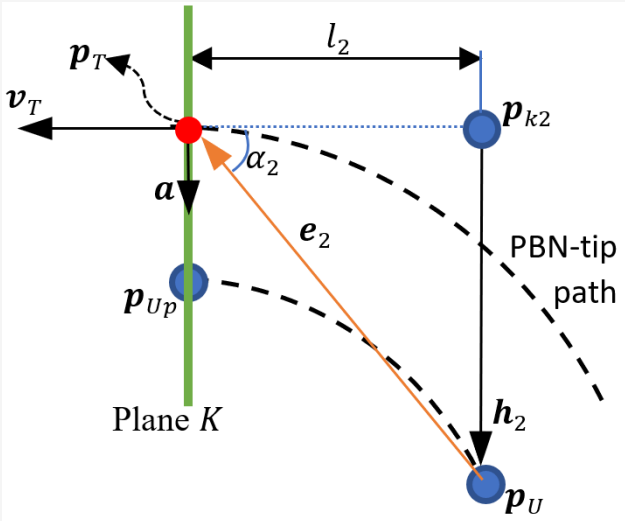

Figure 4.5: Illustration of the vectors and distances used in estimation of the vector, $\boldsymbol{a}$. $\boldsymbol{p}_U$ represents the position vector of the sensor with smaller φ from the diagonal couple excluding LS. $\boldsymbol{p}_{Up}$ is the position vector of the projection of this sensor onto the plane K, which is at $\boldsymbol{p}_T$ and perpendicular to $\boldsymbol{v}_T$. $\boldsymbol{v}_T$ is the unit vector showing the orientation of the PBN tip. $\boldsymbol{e}_2$, α_2, $\boldsymbol{h}_2$, l_2 are as shown. $\boldsymbol{p}_{k2}$ is the auxiliary intersection point. Note that $\boldsymbol{a}$ is in the same direction with $\boldsymbol{h}_2$.

In the ideal case and when all the segments are aligned, the angle, θ, between $\boldsymbol{b}$ and $\boldsymbol{a}$, is expected to be 90°, since each segment covers only a quarter of the PBN's cross-section, and these vectors are in the direction of the segment tips, which are adjacent to each other. However, because of the low stiffness of the catheter and the noise with the sensing data, estimation of θ is required. To create the PBN-tip-frame such that the basis axes of it are perpendicular to one another, $\boldsymbol{b}$ and $\boldsymbol{a}$ are relocated by taking W_1 and W_2 into account.

In the case where one of the weights is 0, since $\boldsymbol{a}$ is not calculated, θ is taken as 90°. The necessary points and vectors are illustrated in figure 4.6 on page 87 for the case where $W_1 = 1$ and $0 < W_2 < 1$ as an example and the steps for the catheter tip frame definition is given in Algorithm 7.

As a result, catheter tip frame transformation matrix, $\boldsymbol{R}_{Tip} \in \mathbb{R}^{3\times3}$, is created with the bases

Algorithm 6 Auxiliary Calculation (if $W_1 \neq 0$ & $W_2 \neq 0$)

Input: PBN tip position vector and orientation vector: $\boldsymbol{p}_T$,$\boldsymbol{v}_T$, The weights: W_1, W_2, The angles between $\boldsymbol{v}_T$ and $\boldsymbol{v}_i$: $\varphi_i, i \in \{1, 2, 3, 4\}$

Output: Auxiliary Unit Vector $\boldsymbol{a} \in \mathbb{R}^3$, shown in figure 4.5 on the preceding page

```
if W_1 = 1 then
    if min(φ_2, φ_3) = φ_2 then
        p_U = p_2
    else
        p_U = p_3
    end if
else if W_2 = 1 then
    if min(φ_1, φ_4) = φ_1 then
        p_U = p_1
    else
        p_U = p_4
    end if
end if
e_2 = p_T − p_U
α_2 = cos^{−1}((e_2 · v_T)/(‖e_2‖ ‖v_T‖))
l_2 = ‖e_2‖ cos(α)
p_{k2} = p_T − l_2 v_T
h_2 = p_U − p_{k2}
a = h_2/ ‖h_2‖
if (v_T × v_U · a) > 0 then
    z = − cos^{−1}((v_T × v_U · a)/(‖v_T × v_U‖ ‖a‖))
else
    z = π − cos^{−1}((v_T × v_U · a)/(‖v_T × v_U‖ ‖a‖))
end if
a ← z rotation of a about v_T
if p_U = p_3 or p_U = p_4 then
    a = −a
end if
```

axes of the PBN-tip-fixed reference frame.

$$\boldsymbol{R}_{Tip} = \begin{bmatrix} \boldsymbol{u}_1 & \boldsymbol{u}_2 & \boldsymbol{u}_3 \end{bmatrix} \tag{4.4}$$

Algorithm 7 Catheter Tip Frame Definition

Input: The weights: W_1, W_2, The PBN tip orientation vector: $\boldsymbol{v}_T$, The base vector: $\boldsymbol{b}$, The auxiliary vector $\boldsymbol{a}$ (if $W_1 \neq 0$ & $W_2 \neq 0$)

Output: Three basis axes of the PBN-tip-fixed reference frame: $\boldsymbol{u}_1 \in \mathbb{R}^3, \boldsymbol{u}_2 \in \mathbb{R}^3, \boldsymbol{u}_3 \in \mathbb{R}^3$

```
if W_1 ≠ 0 & W_2 ≠ 0 then
    θ = cos^{-1}((b · a)/(||b|| ||a||))
else
    θ = π/2
end if
if W_1 = 1 then
    D ← anticlockwise {directions shown in figure 4.6}
else if W_2 = 1 then
    D ← clockwise
end if
γ = min(W_1, W_2)(π/2 − θ)/2
g_1 ← π/4 rotation of b about v_T in the direction of D
g_2 ← γ rotation of g_1 about v_T towards b

u_2 ← π/4 rotation of g_2 about v_T anti-clockwise
u_3 = v_T
```

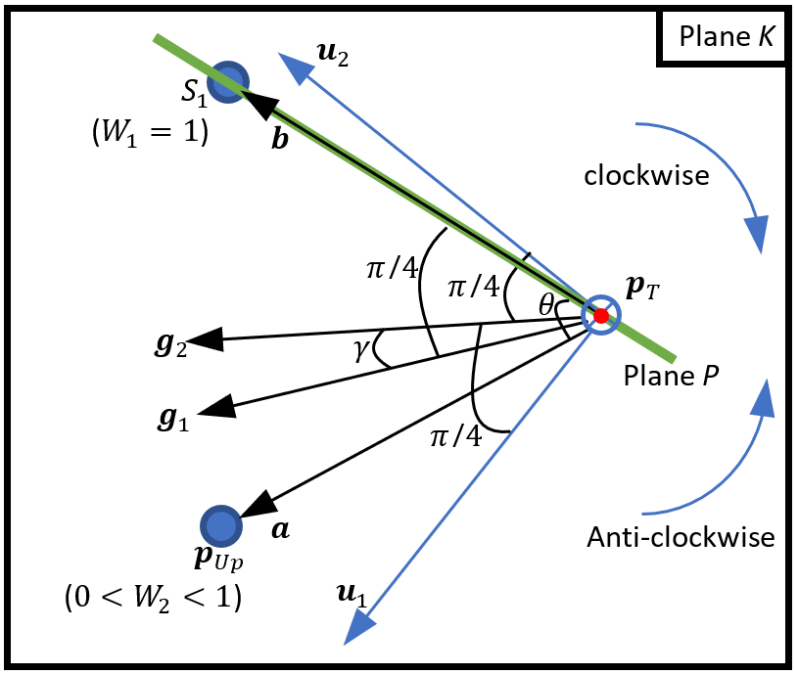

Figure 4.6: The vectors that are used in Algorithm 7. Note that in this figure it is assumed that S_1 is the LS, and this condition is satisfied: $\min(\varphi_2, \varphi_3) = \varphi_2$. Therefore, $\boldsymbol{p}_{Up}$ corresponds to the projection of S_2

4.3 Experimental Methods

To validate the reconstruction process, a set of tests were conducted using two 3D printed guides, which were printed using Markforged Mark Two 3D printer (printing resolution: 100 μm), as shown in figure 4.7, each of which was designed with an inner hollow channel to accommodate the PBN.

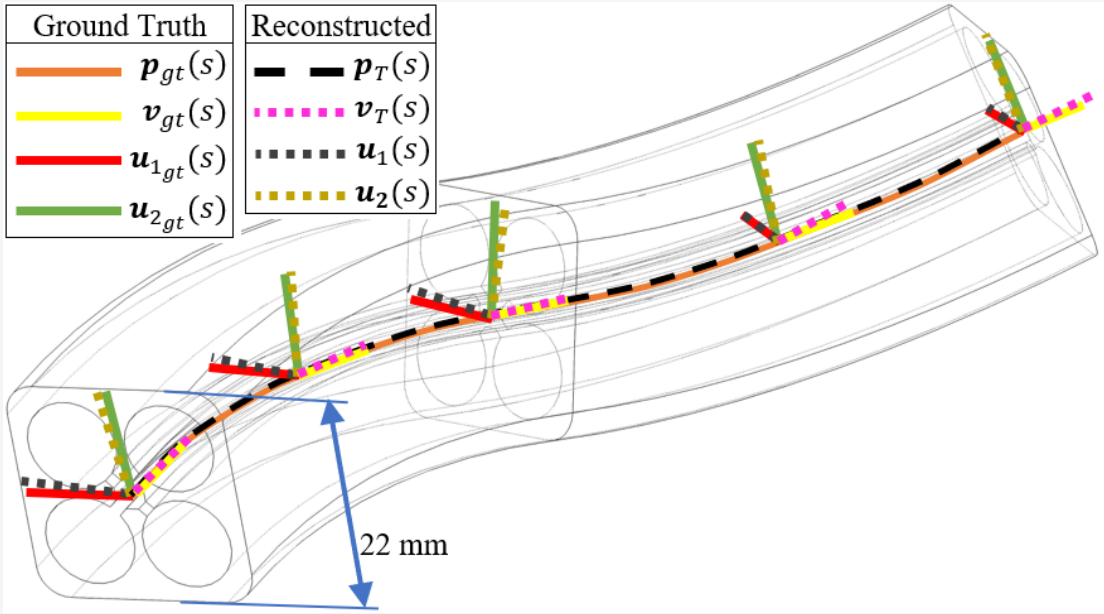

Figure 4.7: Schematic of one of the 3D-printed guides used in the bench-test validation

The 3D guides needed to be printed vertically since having support material in their channels is not desirable due to the difficulties with the removal process. In order to make sure that no error occurs because of gravitational forces during vertical printing, a planar guide, which was printed vertically, and the negative of this part, which was printed horizontally, were produced. Then, it was seen that these two parts fit perfectly as seen in figure 4.8, and there is no recognisable difference between the accuracy of the vertically printed part and the horizontally printed part.

The centre-line of both of the guides used in the experiments consists of two 60 mm-constant-curvature-parts, which have a radius of 120 mm. and 90 mm. respectively, and lie on perpen-

Figure 4.8: The parts printed to compare the vertical and horizontal print accuracy

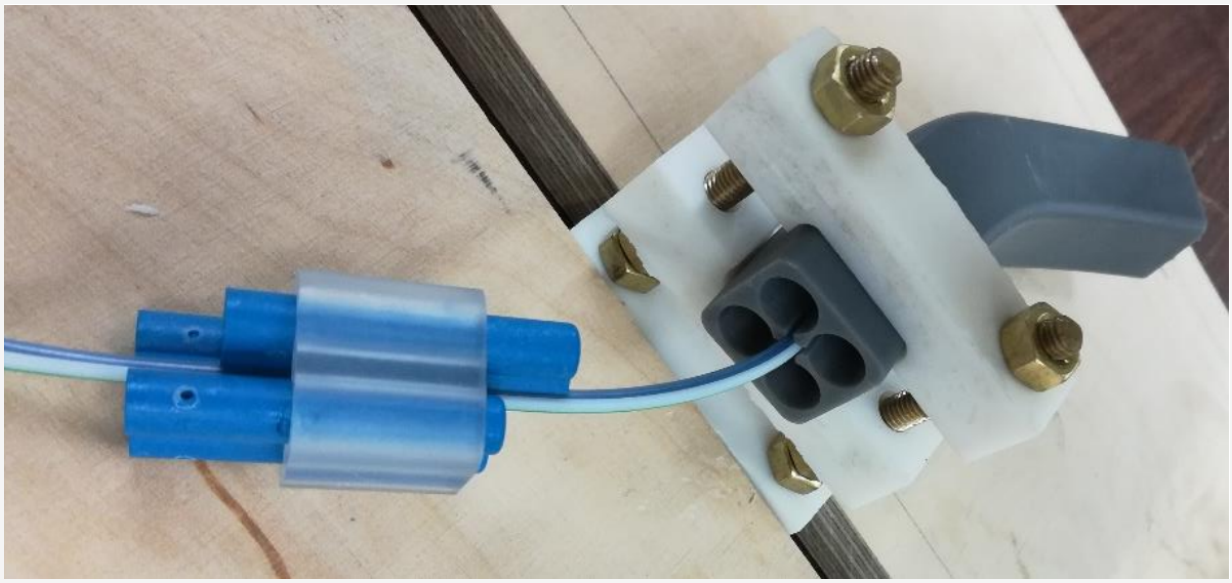

Figure 4.9: EM-based tip pose reconstruction experiment

dicular planes.

The difference between the guide center-lines is that the first guide has no torsional twist, whereas the second guide has a constant torsional twist of 0.25°/mm. A set of 3 insertions was performed with multiple offsets up to 20 mm between any two segments, which is the maximum reported for dynamic mapping of offset-curvatures in [124]. Note that the procedure solves the pose reconstruction at each time step along the arc-length of the insertion, thus it was considered that, with 3 insertions, the reconstruction was tested approximately 1,500

times.

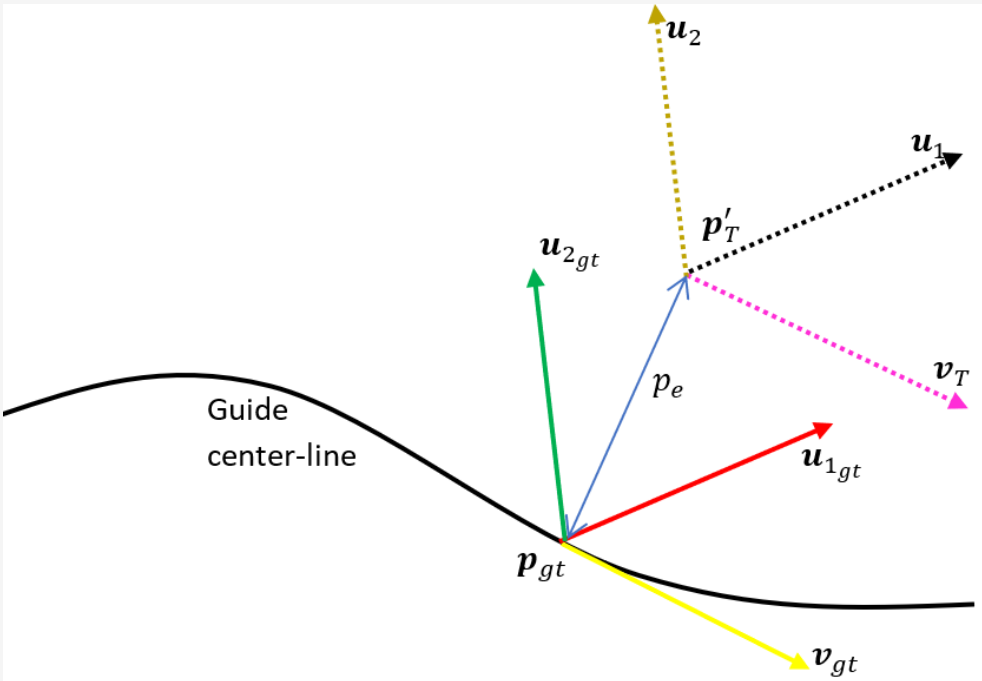

Figure 4.10: Illustration of axes used in figure 4.7 on page 88

The metrics to validate the system are defined using three discrete error measurements between the reconstructed pose and the poses of each guide's center-line. Both metrics are parametrised by the arc-length s of the spline that defines the guide centre-line and which the catheter is constrained to follow. The results of the bench-test validation with error metrics defined as:

$$
\begin{aligned}
p_e &= \left\| \boldsymbol{p'}_T(s) - \boldsymbol{p}_{gt}(s) \right\| \\
\phi_e &= \cos^{-1}((\boldsymbol{v}_T(s) \cdot \boldsymbol{v}_{gt}(s)) \\
\beta_e &= \cos^{-1}((\boldsymbol{u}_1(s) \cdot \boldsymbol{u}_{1_{gt}}(s))
\end{aligned}
$$

where $p_e \in \mathbb{R}_{\geq 0}$ is the magnitude of the position error between the PBN tip, $\boldsymbol{p'}_T(s) \in \mathbb{R}^3$, and the ground truth, $\boldsymbol{p}_{gt}(s) \in \mathbb{R}^3$.

Here, $\phi_e \in \mathbb{R}_{\geq 0}$ is the angle between the unit orientation vectors of the PBN tip, $\boldsymbol{v}_T(s) \in \mathbb{R}^3$, and the ground truth, $\boldsymbol{v}_{gt}(s) \in \mathbb{R}^3$. Lastly, $\beta_e \in \mathbb{R}_{\geq 0}$ is the torsional twist error, which is

defined as the angle between the unit lateral basis axes of the PBN tip fixed reference frame, $\boldsymbol{u}_1(s) \in \mathbb{R}^3$, and the ground truth, $\boldsymbol{u}_{1_{gt}}(s) \in \mathbb{R}^3$. These axes are illustrated in figure 4.7 on page 88. The parameter s is reconstructed from encoder values.

4.4 Results and Discussion

The results of the validation experiments are reported in figure 4.11. The overall average error in pose reconstruction at the 50th percentile are: 0.33 mm, 1.42° and 4.43°, respectively, for the position error p_e, orientation error ϕ_e, and torsional twist error β_e.

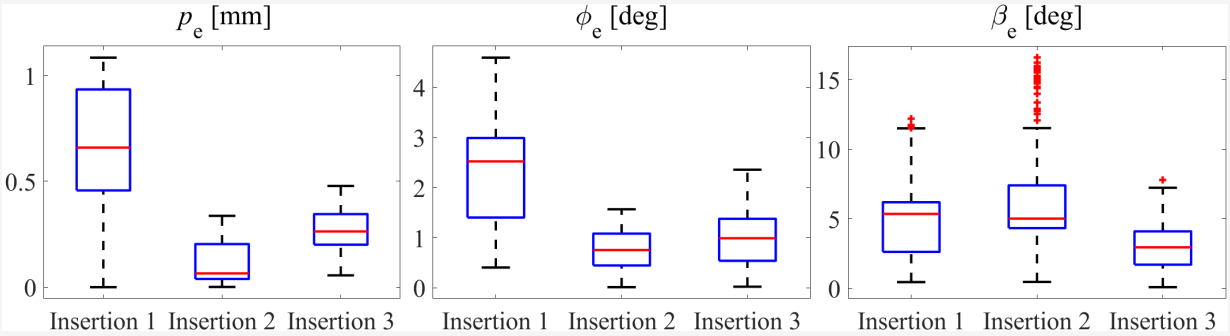

Figure 4.11: Results from the 3D printed guide trials. Position error p_e, Orientation error ϕ_e, and torsional twist error β_e. Insertion 1 and Insertion 2 was conducted using Guide 1, and Insertion 3 was conducted using Guide 2.

Although the same guide was used in Insertion 1 and Insertion 2, lower position and orientation errors were obtained in the latter. The reason for this could be that the PBN used in Insertion 2 had already been used several times, and its outer shape fit the guide in a better way. Therefore, it is thought that the PBN was centred in the guide's channel more precisely during the insertion, which led to lower position and orientation errors. Having a third experiment using the same guide would have been better to have a clearer picture regarding the algorithm's performance, but it could not be performed due to an inconvenience with the experimental setup.

When compared to another PBN tip pose estimation study [29], in which an extended Kalman Filter (KF) algorithm was presented for a 2-segment PBN, the results are mainly comparable except for the twist errors, which is higher in our study. The reason for this could be the difference between the methods used and the difference between the validation experiments. In this thesis, 3D experiments were conducted using a 4-segment PBN, whereas, in [29], the proposed algorithm was validated with planar experiments using a 2-segment PBN.

The position error obtained from the first insertion is illustrated in figure 4.12 to show that the error does not grow during needle navigation.

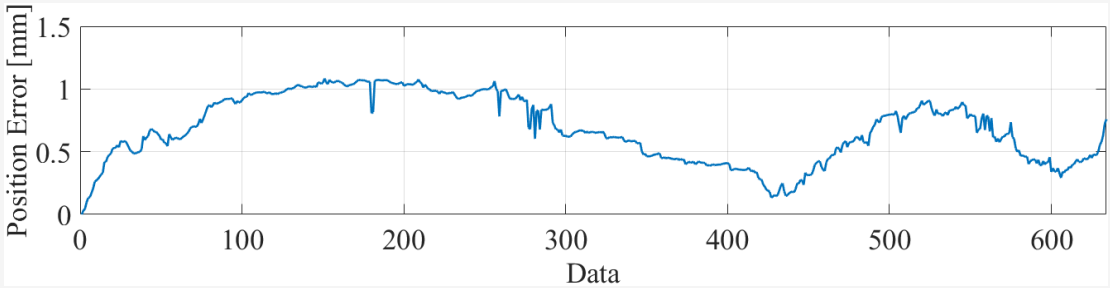

Figure 4.12: The position error during Insertion 1

Since a small position error can cause a large angular error (the diameter of the circle created by the sensors is 2 mm), the relatively large twist error was in the range of what was expected, given the experimental setup. The illustration of the effect of small position error on the twist angle calculation is illustrated in figure 4.13. As can be seen, a 0.5-mm error in the sensor position can cause a 29° angular error.

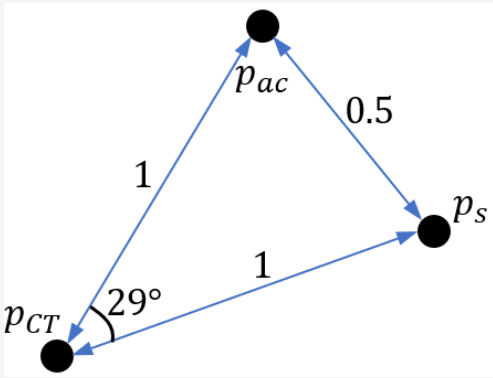

Figure 4.13: The illustration of the effect of small position error on the twist angle calculation. Distances are in mm. $\boldsymbol{p}_{CT}$ is the catheter tip point position. $\boldsymbol{p}_{ac}$ and $\boldsymbol{p}_s$ represent actual sensor position and sensor position according to the sensor data respectively.

4.5 Conclusion

In this chapter, a novel method for PBN pose estimation using four 5-DoF sensors was presented, and the experimental results were discussed. Such a method was required to drive the correct segments to steer the PBN in a desired direction, and it was developed based on the projection of sensor positions onto the plane at the PBN tip and perpendicular to the orientation vector. The chapter began with data acquisition and the segment labelling algorithm, while the segment labels were arranged according to their locations, which was required, since, later on, the sensors contributed to the reconstruction algorithm based on their relative locations. Then, an algorithm was given based on dot and cross products of the segments' orientation vectors and the vectors between the sensors to find the LS. It was necessary to develop such a particular algorithm to account for the path-dependent discrepancies of PBN segments. Then, the PBN tip position calculation algorithm using the LS and DS was outlined. A partial no-torsion assumption was made for the length between LS tip and DS tip. The rotational coordinates were determined by constructing the tip reference frame, and finally, the rotational transformation of the PBN tip with respect to the inertial reference frame was determined in quaternions. The presented algorithm does not depend on EM sensors, and other types of sensors could also be used as long as the same type of information is obtained.

The experimental results showed that the developed method effectively reconstructed the full-tip pose of the needle under the assumptions made. The developed method inherently reduced the reconstruction error by fusing the data from the four EM sensors together with the reconstruction of the full pose. This method can be extended to other applications in which full pose estimation must be derived from reduced order measurements.

In the next chapter, another localisation algorithm, which is based on Fibre Bragg Grating (FBG) sensing, is presented.

Chapter 5

Dynamic 3D Shape Reconstruction for Steerable Needles with Fiber Bragg Gratings in Multi-Core Fibers

5.1 Introduction

Fibre Bragg Grating (FBG)-based fibre-optic shape reconstruction techniques are commonly preferred in steerable needle studies because of their small size, which is of great importance for miniaturised needles, Magnetic resonance imaging (MRI) and Electromagnetic (EM) wave compatibility [117], [85], having non-toxic and bio-compatible material properties [113].

This chapter introduces a novel FBG-based shape reconstruction method that ensures that frequent measurements along the fibre length can be acquired even in the presence of only 1 FBG set, which is located at the needle tip, irrespective of the number of bending direction discontinuities along the length of the fibre. Previously proposed approaches focused on reconstructing the steerable needle shape itself, whereas in this thesis, it is proposed to reconstruct the path created by the steerable needle tip during its insertion into soft tissue instead. This method is based on the follow-the-leader assumption, where the needle body follows the needle tip, which is a valid approximation for most steerable needle embodiments [102], [1], [92], [124]. This approach also enables the reconstruction of the full needle, regardless of where the gratings stop.

In a sense, only using the FBG set at the needle tip is similar to tip tracing methods based on, e.g. an EM sensor embedded within the needle tip. However, while three dimensional (3D) tip position information can be acquired directly in this way, curvature vectors covering the entire fibre are needed in the case of FBGs to estimate the same information so that the shape is reconstructed from base to tip by numerical integration. In this thesis a method is proposed to acquire the required curvature vectors along the entire needle with only 1 FBG set. Furthermore, a Kalman Filter (KF)-based algorithm is introduced to fuse the information at different discrete time steps, and from different FBG sets in the case where there is more than one along the fibre, which enables the detection of shape changes due to possible soft tissue movements, alongside increases in reconstruction and tracking accuracy.

The proposed method's performance and other commonly used methods from the literature have been compared in a noise-free simulation environment. Additionally, validation experiments were performed *in vitro* and *ex vivo* with a clinically-sized, medical-grade Programmable Bevel Tip Steerable Needle (PBN).

5.1.1 Publications

This chapter is from an edited version of the article:

- **Donder, A.**, Rodriguez y Baena, F. (Accepted in 2021). Kalman Filter-Based, Dynamic 3-D Shape Reconstruction for Steerable Needles with Fiber Bragg Gratings in Multi-Core Fibers. Accepted to IEEE Transactions on Robotics [25] ©2021 IEEE

5.2 FBG Theory

An FBG is a grating pattern with a periodic refractive index modulation etched onto an optical fiber, which has the property of reflecting the light of a specific wavelength, the Bragg wavelength, λ_B, which is a function of temperature and strain [48].

$$\lambda_B = 2n_{eff}\Lambda \tag{5.1}$$

where n_{eff} is the effective refractive index and Λ is the grating period. The relationship between the reflected wavelength shift and change in temperature, ΔT, and strain, ε, is given as follows:

$$\Delta\lambda = \lambda_B((1 - p_e)\varepsilon + (\alpha_\lambda + \alpha_n)\Delta T) \tag{5.2}$$

where p_e is the photo-elastic coefficient, and α_λ and α_n are the thermal expansion coefficient and the thermo-optic coefficient, respectively [48].

When the temperature change can be assumed to be 0 (it is not assumed to be 0 in this thesis), the axial strain on an FBG can be computed as:

$$\varepsilon = \frac{\Delta\lambda}{\lambda_B(1 - p_e)} \tag{5.3}$$

Assuming that the fibre is in pure bending and behaves as a uniform, symmetric, linear Kirchhoff rod [59], the axial strains due to bending at each core can be derived from mechanics principles as follows [47]:

$$\varepsilon_j(s) = -\kappa(s)\delta_j(s) \tag{5.4}$$

where s represents the arc length parameter along the fibre $(0, L)$, where L is the length of the fibre, $\varepsilon_j(s)$ is the strain at the jth core, with $j \in 1, ..., G$, and G is the total number of

off-centred cores. $\kappa(s)$ is the curvature, and $\delta_j(s)$ is the distance between the centre of the jth core and the neutral bending plane, as shown in figure 5.1 on the following page. Therefore, (5.4) can be written as follows:

$$\varepsilon_j(s) = -\kappa(s) r_j cos(\beta(s) + \theta + \theta_{1j}) + \varepsilon_0(s) \tag{5.5}$$

where r_j is the radial distance between the fibre centre and the centre of the jth core, $\beta(s)$ is the angular offset from the curvature vector to the x axis of the local frame, and θ is the angular offset from the x axis of the local frame to the 1st core. Similarly, θ_{1j} is the angular offset from the 1st core to the jth core, with $\theta_{11}(s) = 0$. The curvature vector is defined with $\kappa(s)$ being the magnitude and $\beta(s)$ the bending direction of the curvature vector. It can also be defined as the rate of change of the curve's unit tangent vector with respect to s: $d\boldsymbol{T}(s)/ds$. The strain bias $\varepsilon_0(s)$ is due to additional axial strain and temperature change. When a temperature change can be assumed to affect all the gratings in an FBG set equally due to the proximity of the fibres (as in the case of Multi-core Fibres (MCFs)), the effect of it can be assumed to be compensated by the strain bias [49], [46]. Additionally, in the case of separation between the neutral axes of a needle and the fibre, it is instrumented with, the additional axial strain reflects on $\varepsilon_0(s)$ as well. (5.5) is a general formula, which is valid for any number of cores along a fibre in any configuration, symmetrical or asymmetrical. An example configuration is shown in figure 5.1 on the next page, with 3 cores to illustrate the parameters used in (5.5).

The locations of the FBG sets along a fibre are known *a priori*. To compute the curvature vector, at least 3 linearly independent (i.e., not symmetric about the fibre centre), off-centred cores are necessary. As many equations as the number of such cores can be obtained from (5.5), which can be solved simultaneously to compute the curvature value, $\kappa(s)$, bending direction, $\beta(s)$, and $\varepsilon_0(s)$. Note that at least 3 equations are required for this calculation ($G \in \mathbb{Z}_{\geq 3}$). In the presence of more than 3 available cores, the equations from all of the cores can be used to increase accuracy and improve robustness via redundancy. In matrix form, (5.5) can be written for G cores as follows:

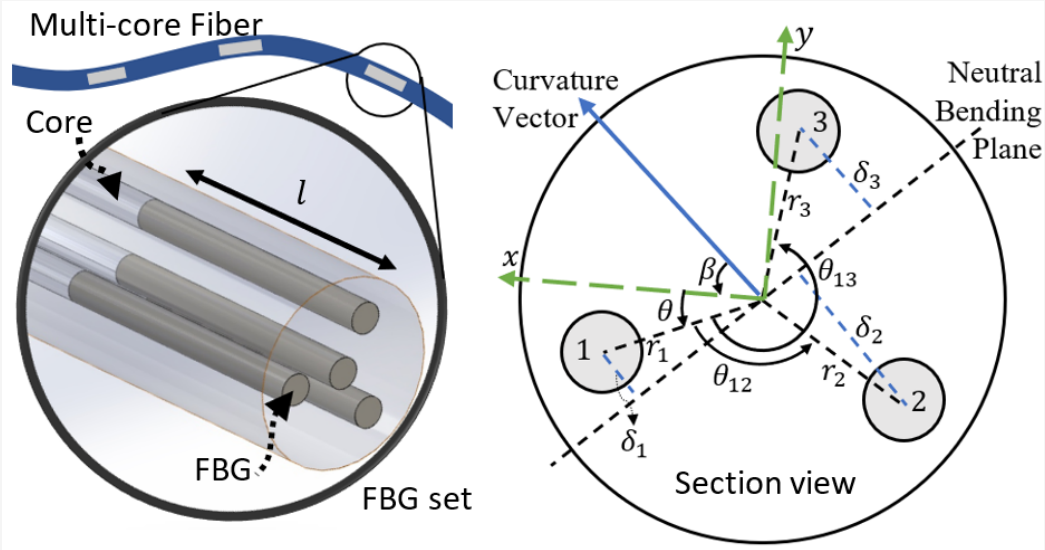

Figure 5.1: Left: FBG-inscribed MCF including 4 cores: 1 centred, 3 off-centred. Right: MCF with 3 off-centred cores in section view (an FBG set). The cores are denoted by the numbers: $1, 2, 3$. r_j is the radial distance from the MCF centre to the centre of the jth core, where $j \in \{1, 2, 3\}$. δ_j is the distance between the neutral bending plane and the jth core centre. The local frame is denoted by the x, y axes. θ is the angular offset from the local x axis to the 1st core. β is the angular offset from the curvature vector to the local x axis. θ_{12} is the angle from the 1st core to the 2nd core. Similarly, θ_{13} is the angle from the 1st core to the 3rd core.

$$\underbrace{\begin{bmatrix} \varepsilon_1(s) \\ \vdots \\ \varepsilon_G(s) \end{bmatrix}}_{\boldsymbol{\varepsilon}(s)} = \underbrace{\begin{bmatrix} -r_1 cos(\theta_{11}+\theta) & r_1 sin(\theta_{11}+\theta) & 1 \\ \vdots & \vdots & \vdots \\ -r_G cos(\theta_{1G}+\theta) & r_G sin(\theta_{1G}+\theta) & 1 \end{bmatrix}}_{\boldsymbol{M}} \underbrace{\begin{bmatrix} \kappa(s) cos\beta(s) \\ \kappa(s) sin\beta(s) \\ \varepsilon_0(s) \end{bmatrix}}_{\boldsymbol{\alpha}(s)} \tag{5.6}$$

Solving for $\boldsymbol{\alpha}(s)$:

$$\boldsymbol{\alpha}(s) = \boldsymbol{M}^{\dagger}\boldsymbol{\varepsilon}(\boldsymbol{s}) \tag{5.7}$$

where $\boldsymbol{M}^{\dagger}$ is Moore-Penrose pseudo-inverse of $\boldsymbol{M}$ (Note that $\boldsymbol{M}$ is not necessarily a square matrix).

As a result:

$$\kappa(s) = \sqrt{\boldsymbol{\alpha}_1(s)^2 + \boldsymbol{\alpha}_2(s)^2} \tag{5.8}$$

$$\beta(s) = atan_2(\boldsymbol{\alpha}_2(s), \boldsymbol{\alpha}_1(s)) \tag{5.9}$$

The torsion can be approximated with numerical derivation:

$$\tau(s) = \frac{\beta(s) - \beta(s - \Delta s)}{\Delta s} \tag{5.10}$$

$\kappa(s)$, $\beta(s)$, and $\tau(s)$ are used for shape reconstruction, as reviewed in the following section.

5.3 Background

Shape reconstruction methods require the information from the strain values or the curvature vectors along the entire fibre. However, only sparse measurements can be obtained with discrete FBG sets, and, therefore, an interpolation/curve fitting method is required to estimate the intermediate values. Although, in this study, the proposed shape reconstruction method does not require the estimation of the intermediate strain values or curvature vectors in between the FBG sets, an overview of interpolation and curve fitting methods is given in Section 5.3.1 for completeness. Also, in the following sections, shape reconstruction methods from the literature, based on discrete FBG measurements, are reviewed. These methods show promise, but their accuracy is susceptible to errors of the interpolation methods.

5.3.1 Interpolation/Curve Fitting Methods

In this section, interpolation and curve fitting methods based on discrete FBG measurements are reviewed from the literature to help interpret the comparative study in Section 5.5.

The accuracy of fibre tip pose estimation highly depends on selecting the most suitable interpolation/curve fitting methods to determine the intermediate strain values or curvature vectors between the discrete FBG sets. For example, a small curvature error due to the applied interpolation method will result in a large position error at the tip due to error accumulation during numerical integration.

Henken *et al.* [46] presented an error analysis of standard interpolation methods. They used the curvature vector as the interpolation parameter, as in most of the studies in the literature. However, Jäckle *et al.* [49] proposed interpolating the strain because of its continuity along the fibre, when considering the possible discontinuity in the bending direction.

A simulation study comparing the proposed method with the methods requiring interpolation is given in Section 5.5, alongside an analysis investigating the effect of discontinuities in the bending direction to shape sensing accuracy.

5.3.2 Frenet-Serret Frame (FSF)-Based Method

This shape reconstruction method is based on the FSF equations [87], [53]:

$$\frac{d\boldsymbol{\gamma}(s)}{ds} = \boldsymbol{T}(s), \quad \frac{d\boldsymbol{N}(s)}{ds} = -\kappa(s)\boldsymbol{N}(s) + \tau(s)\boldsymbol{B}(s)$$

$$\frac{d\boldsymbol{T}(s)}{ds} = \kappa(s)\boldsymbol{N}(s), \quad \frac{d\boldsymbol{B}(s)}{ds} = -\tau(s)\boldsymbol{N}(s) \tag{5.11}$$

where $\boldsymbol{\gamma}(s)$ is the position vector in $\mathbb{R}^3$, $\boldsymbol{T}(s)$ the unit tangent vector, $\boldsymbol{N}(s)$ the unit normal vector, $\boldsymbol{B}(s)$ the unit binormal vector, $\kappa(s)$ the curvature value, and $\tau(s)$ the torsion of the curve (i.e., the rate of change of bending direction, $\beta(s)$).

This method requires that the curve to be reconstructed must be with non-zero curvature along its length; otherwise, it generates ambiguity in the definition of $\boldsymbol{N}(s)$ and $\boldsymbol{B}(s)$, because $\tau(s)$ is not defined in the case of zero curvature [44]. After estimating intermediate curvature values in between the FBG sets using one of the methods in Section 5.3.1, the shape is reconstructed as follows:

With $\boldsymbol{R(s)} = [\boldsymbol{T}(s)\boldsymbol{N}(s)\boldsymbol{B}(s)] \in SO(3)$ being an orthonormal frame, equation set 5.11 can be written in matrix form as follows:

$$\frac{d}{ds}\boldsymbol{X}(s) = \boldsymbol{X}(s)\boldsymbol{A}(s) \tag{5.12}$$

where the pose $\boldsymbol{X}(s) \in SE(3)$:

$$\boldsymbol{X}(s) = \begin{bmatrix} \boldsymbol{R}(s) & \boldsymbol{\gamma}(s) \\ \boldsymbol{0}_{1\times 3} & 1 \end{bmatrix} = \begin{bmatrix} \boldsymbol{T}(s) & \boldsymbol{N}(s) & \boldsymbol{B}(s) & \boldsymbol{\gamma}(s) \\ 0 & 0 & 0 & 1 \end{bmatrix} \tag{5.13}$$

and the twist matrix $\boldsymbol{A}(s) \in \mathfrak{se}(3)$, which agrees with the nonholonomic kinematics of steerable needles, is given as;

$$\boldsymbol{A}(s) = \begin{bmatrix} 0 & -\kappa(s) & 0 & 1 \\ \kappa(s) & 0 & -\tau(s) & 0 \\ 0 & \tau(s) & 0 & 0 \\ 0 & 0 & 0 & 0 \end{bmatrix} \tag{5.14}$$

Note that, in the case of interpolation, the elements of $\boldsymbol{A}(s)$ are the interpolated curvature and torsion values. To reconstruct the shape, (5.12) can be discretized assuming that the twist, $\boldsymbol{A}(s)$, is constant between two discretized arclength positions, s:

$$\boldsymbol{X}(s + \Delta s) = \boldsymbol{X}(s) \exp(\boldsymbol{A}(s)\Delta s) \tag{5.15}$$

where Δs is the unit distance between two consecutive discrete curve steps.

Lastly, the position vectors, $\boldsymbol{\gamma}(s)$, of the reconstructed shape are found in the last column of the pose, $\boldsymbol{X}(s)$, for every discretized arclength position, s.

5.3.3 Parallel Transport Frame (PTF)-Based Method

This shape reconstruction method is based on the PTF [8], which satisfies the following frame equations:

$$\frac{d\boldsymbol{\gamma}(s)}{ds} = \boldsymbol{T}(s), \quad \frac{d\boldsymbol{T}(s)}{ds} = \kappa_1(s)\boldsymbol{N}_1(s) + \kappa_2(s)\boldsymbol{N}_2(s)$$

$$\frac{d\boldsymbol{N}_1(s)}{ds} = -\kappa_1(s)\boldsymbol{T}(s), \quad \frac{d\boldsymbol{N}_2(s)}{ds} = -\kappa_2(s)\boldsymbol{T}(s) \tag{5.16}$$

where $\boldsymbol{T}(s)$ is the unit tangent vector and $\boldsymbol{N}_1(s)$, $\boldsymbol{N}_2(s)$ the unit normal vectors. $\kappa_1(s)$ and $\kappa_2(s)$ describe the change of $\boldsymbol{T}(s)$ in the $\boldsymbol{N}_1(s)$ and $\boldsymbol{N}_2(s)$ directions at arc length position s and are calculated as follows:

$$\kappa_1(s) = \kappa(s)cos(\beta(s))$$

$$\kappa_2(s) = \kappa(s) sin(\beta(s)) \tag{5.17}$$

The PTF is illustrated in figure 5.2. This method is advantageous over the FSF since it is defined for every curve, including zero curvature curves. $\boldsymbol{N}_1(s)$, and $\boldsymbol{N}_2(s)$ change slightly along the curve upon being chosen arbitrarily at the needle base, such that the frame components are perpendicular to one another. The shape is reconstructed in a similar way as in the case of FSF-based reconstruction, with the pose, $\boldsymbol{X}(s)$, and the twist, $\boldsymbol{A}(s)$, matrices defined as:

$$\boldsymbol{X}(s) = \begin{bmatrix} \boldsymbol{T}(s) & \boldsymbol{N}_1(s) & \boldsymbol{N}_2(s) & \boldsymbol{\gamma}(s) \\ 0 & 0 & 0 & 1 \end{bmatrix} \tag{5.18}$$

$$\boldsymbol{A}(s) = \begin{bmatrix} 0 & -\kappa_1(s) & -\kappa_2(s) & 1 \\ \kappa_1(s) & 0 & 0 & 0 \\ \kappa_2(s) & 0 & 0 & 0 \\ 0 & 0 & 0 & 0 \end{bmatrix} \tag{5.19}$$

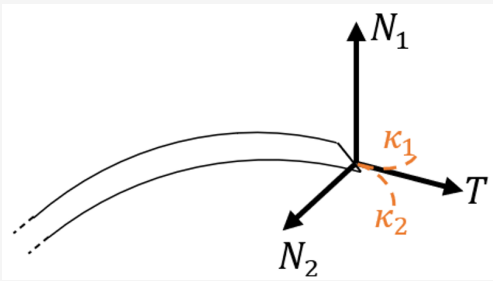

Figure 5.2: Body frame coordinates (PTF) shown on a bevel-tip needle. κ_1 and κ_2 represent the change of the tangent vector $\boldsymbol{T}$ in directions $\boldsymbol{N}_1$ and $\boldsymbol{N}_2$.

5.3.4 Piecewise constant curvature method

Roesthuis *et al.* [92] proposed a reconstruction method based on piecewise constant curvature elements. The $(i+1)^{th}$ element expressed in previous element's frame is created with a constant curvature vector:

$$\boldsymbol{p}_{i+1}^{i} = \begin{bmatrix} dx & dy & dz \end{bmatrix}$$

$$= \begin{bmatrix} \rho_i sin(d\theta_i) & 0 & \rho_i cos(d\theta_i) - \rho_i \end{bmatrix} \tag{5.20}$$

where dx, dy, and dz are the Cartesian distances, ρ_i is the radius of curvature, and $d\theta_i = ds/\rho_i$ with ds being the length of the curvature element. Therefore, the whole shape is obtained by directly integrating these discrete elements. Linear spline interpolation was used to estimate the intermediate curvature values in their study.

5.3.5 Polynomial shape-based methods

Seifabadi *et al.* [109] proposed fitting an nth order polynomial to n curvature values obtained from FBG measurements. The displacement along the fibre is obtained by integrating the polynomial twice and applying the boundary conditions; $y'(0) = 0$ and $y(0) = 0$.

$$y''(s) = \kappa(s) \tag{5.21}$$

where $y(s)$ is the deflection, $y'(s)$ and $y''(s)$ are the first and second derivatives of deflection, and $\kappa(s)$ is the curvature value at arc length s. In this method, the intermediate curvature values are accessed via the fitted continuous polynomial.

5.3.6 Data-driven Regression Approachs (DDRAs)

Sefati *et al.* [107] proposed a regression-model-based method which is sensor-model-independent and only requires the raw data of the FBG wavelengths to estimate the tip position of a continuum dexterous manipulator. Although this method does not require the estimation of intermediate strain values or curvature vectors, the tip position estimation performance is expected to increase as the number of measurements increases along the fibre.

5.4 Materials and Methods

Regardless of the total number of FBG sets that an MCF inside a needle possesses, in this thesis it is proposed that only the FBG set at the fibre's tip is used to reconstruct the shape during soft tissue navigation. In the case of more than 1 available FBG set, the information from different sets can then be fused using the method proposed in Section 5.4.3.

Because of the "follow-the-leader" nature of steerable needles, it is assumed that the needle's shape overlaps with the path created by its tip during navigation into soft tissue. Therefore, instead of reconstructing the fibre shape, the shape of the path covered by the fibre's tip is reconstructed. The curve created during navigation of the MCF tip is modelled as a regular unit-speed space curve in $\mathbb{R}^3$ with $i \in \{1, ..., N_k\}$ denoting the discrete curve points. N_k is the total number of curve points at discrete sampling time k: t_k. The fibre is assumed to be in pure bending, and it is modelled as a uniform-density, symmetric (circular cross-section), linear Kirchhoff rod [59].

5.4.1 Shape Reconstruction

The curve points are assumed to be fixed with respect to the soft tissue (and not with respect to the needle). Therefore, as the needle advances into the soft tissue, the curvature vectors at newly covered ground are calculated at each time step (figure 5.3 on the next page). Let $n_k \in \mathbb{Z}_{\geq 0}$ be the number of curve points created (i.e., positions of which are calculated) at t_k in the case of the advancement of the needle into soft tissue. Let $\tilde{\boldsymbol{c}}_k = \begin{bmatrix} \tilde{\kappa}_{1,k} & \tilde{\kappa}_{2,k} \end{bmatrix}^T \in \mathbb{R}^{2\times 1}$ be the curvature pair as given in (5.17) calculated after obtaining the segment's curvature vectors using wavelength readings at t_k.

Also, let $\hat{\boldsymbol{c}}_k^i = \begin{bmatrix} \kappa_{1,k}^i & \kappa_{2,k}^i \end{bmatrix}^T \in \mathbb{R}^{2\times 1}$ be the curvature pair of the ith curve point at t_k. The curvature pairs corresponding to newly covered ground, and N_k are obtained as follows.

$$\hat{\boldsymbol{c}}_k^i = \tilde{\boldsymbol{c}}_k \tag{5.22}$$

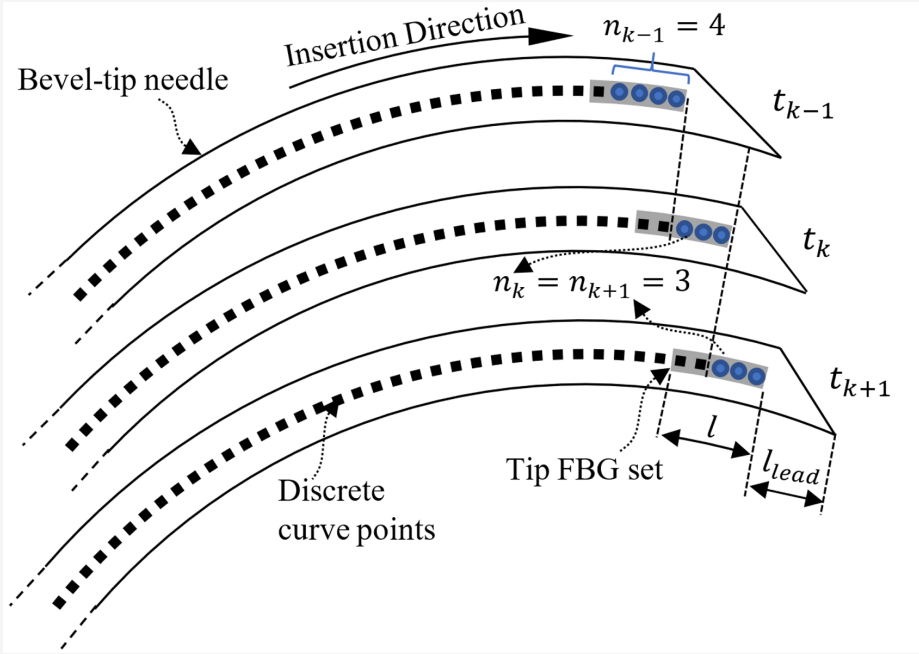

Figure 5.3: Two dimensional (2D) Illustration of needle insertion into soft tissue. A bevel-tip needle is illustrated at three successive time steps. The FBG set with the length of l is shown at the tip in grey. The discrete curve points are assumed to be fixed with respect to the soft tissue (not with respect to the needle). The curve points created at the current time step are shown in blue circles, whereas the curve points created at the previous time steps are shown in black squares. Note that the illustration was prepared in such a way that $n_{k-1} \neq n_k$ and $n_{k-1} \neq n_{k+1}$ to indicate that this value is not fixed, and it is a function of the navigation length at the corresponding time step. The distance between the needle tip and the FBG set is called lead-out length, l_{lead}, and the curvature values of which can be estimated by extrapolation. $n_k \in \mathbb{Z}_{\geq 0}$ is the number of curve points created at t_k.

$$N_k = N_{k-1} + n_k \tag{5.23}$$

5.4.2 Compensation for the Lead-Out Length

The length between the tip FBG set and the needle tip is called the "lead-out" length, as shown in figure 5.3 as l_{lead}. This length is required for three reasons: (i) to accommodate the needle tip's bevelled shape, (ii) to protect the end of the fibre, (iii) to position the tip FBG set at a point where the relevant curvature of the needle tip can be measured. The curvature of the needle tip is best measured at a small distance from its very tip due to the soft needle material, and the tolerances between the outer diameter of the fibre and the diameter of the needle's

working channel. This situation is illustrated in figure 5.4. Therefore, $\tilde{\boldsymbol{c}}_k$ is also assigned to curvatures corresponding to this length.

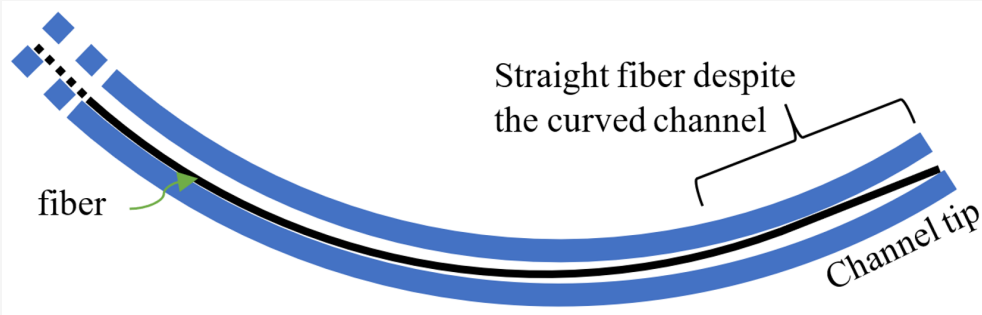

Figure 5.4: A needle working channel. The last bits of fibres tend to be straight even if the needle curves because of the soft needle material and the clearance between the fibre and the channel. The width of the channel is exaggerated for clarity.

5.4.3 KF-Based Sensor Fusion

In this study, a KF is used to obtain more reliable estimates of the curvatures along the fibre length. The measurements at a time step are used to create or update the curve points of the ground that is covered by the FBG set/sets at that time step. Let M be the total number of FBG sets along a fibre, and FBG_m, $m \in \{1, ..., M\}$, be the mth FBG set from the fibre tip (e.g., FBG_1 is the FBG set at the fibre tip) as shown in figure 5.5 on the following page. As a needle is inserted into a soft tissue, the very first shape reconstruction is obtained by FBG_1 as described in the previous sections. If there are other FBG sets, once FBG_2 reaches a curve point of the reconstructed path, the curvature information from FBG_1 is fused with that of FBG_2 by means of a KF. This is repeated as FBG_2 continues to take measurements or other FBG sets start taking measurements from that curve point. This procedure is performed for all the curve points along the fibre. The information from an FBG set is used to update the curvature information of the curve points covered by any part of its length. This process enables shape reconstruction at a length which is greater than the length of the sensorized segment of the fibre.

The KF-based sensor fusion consists of two steps: prediction and correction, which require the formulation of a process model with process noise, and a measurement model with measurement

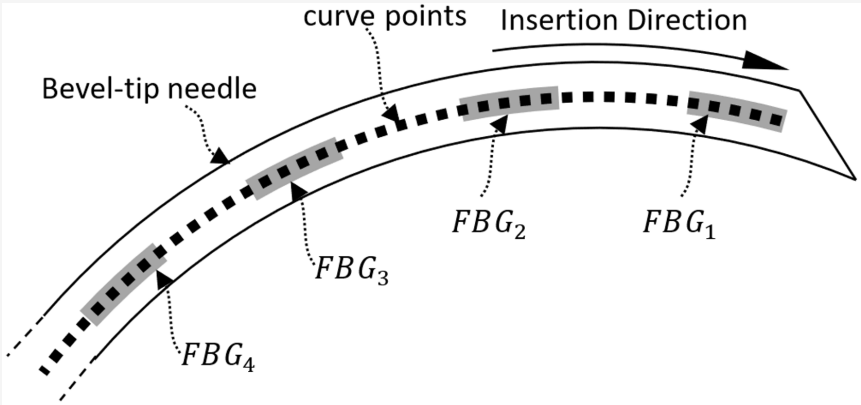

Figure 5.5: 2D Illustration of a bevel-tip needle with an MCF possessing more than one FBG set along its length. The discrete curve points are assumed to be fixed to the soft tissue, and they are created only by FBG_1. The other FBG sets' measurements, each of which corresponds to the entire region covered by the FBG set, are not used to create additional points. Instead, they are used to update the state of the existing curve points covered by their lengths.

noise, respectively [114].

The first state vector, i.e., curvature pair values, of any curve point is always obtained with FBG_1 because the path is created by the tip. After that, the state vector is updated by means of the KF if this curve point is covered by one of the FBG sets. Otherwise, the same values are used for the next time step's state vector.

The process model is defined as a linear stochastic equation:

$$\hat{\boldsymbol{c}}_k^i = \hat{\boldsymbol{c}}_{k-1}^i + \boldsymbol{w} \tag{5.24}$$

where $\boldsymbol{w} \sim \boldsymbol{N}(0, \boldsymbol{Q}) \in \mathbb{R}^{2\times 1}$ is the process noise vector represented by zero-mean Gaussian distribution with $\boldsymbol{Q} \in \mathbb{R}^{2\times 2}$ being the covariance matrix. The reason for process noise uncertainties arises from the possible non-zero error in the follow-the-leader assumption.

The measurement model is defined as follows:

$$\boldsymbol{z}_k^i = \hat{\boldsymbol{c}}_k^i + \boldsymbol{v} \tag{5.25}$$

where $\boldsymbol{z}_k^i$ is the measurement variable and $\boldsymbol{v} \sim \boldsymbol{N}(0, \boldsymbol{R}) \in \mathbb{R}^{2\times1}$ is the measurement noise vector represented by a zero-mean Gaussian distribution with $\boldsymbol{R} \in \mathbb{R}^{2\times2}$ being the covariance matrix.

The covariance matrices $\boldsymbol{Q}$ and $\boldsymbol{R}$ are determined as per description at the end of this subsection. Based on the process and the measurement models, the filter's prediction and correction steps are applied at each sampling loop to correct the state estimates.

Prediction step: In this step, the *a priori* system state at t_k is estimated:

$$\hat{\boldsymbol{c}}_k^{-,i} = \hat{\boldsymbol{c}}_{k-1}^i \tag{5.26}$$

Given the initial estimate, the *a priori* error covariance $\boldsymbol{P}^{-,i} \in \mathbb{R}^{2\times2}$, which is the combination of process noise and the propagation of the error covariance, $\boldsymbol{P}_{k-1}^i$, from the previous state, is estimated as follows:

$$\boldsymbol{P}_k^{-,i} = \boldsymbol{P}_{k-1}^i \boldsymbol{Q} \tag{5.27}$$

Correction Step: In this step, *a priori* estimates of the system state and error covariance are updated with the Kalman Gain, $\boldsymbol{K}_k^i \in \mathbb{R}^{2\times2}$.

$$\boldsymbol{K}_k^i = \boldsymbol{P}_k^{-,i}(\boldsymbol{P}_k^{-,i} + \boldsymbol{R})^{-1}$$

$$\hat{\boldsymbol{c}}_k^i = \hat{\boldsymbol{c}}_k^{-,i} + \boldsymbol{K}_k^i(\boldsymbol{z}_k^i - \hat{\boldsymbol{c}}_k^{-,i}) \tag{5.28}$$

$$\boldsymbol{P}_k^i = (\boldsymbol{I}_2 - \boldsymbol{K}_k^i)\boldsymbol{P}_k^{-,i}$$

where $\boldsymbol{I}_2 \in \mathbb{R}^{2\times2}$ is an identity matrix. If a curve point is not covered by any FBG set at t_k, $\hat{\boldsymbol{c}}_{k-1}^i$ and $\boldsymbol{P}_{k-1}^i$ are directly assigned to $\hat{\boldsymbol{c}}_k^i$ and $\boldsymbol{P}_k^i$ respectively:

$$\hat{\boldsymbol{c}}_k^i = \hat{\boldsymbol{c}}_{k-1}^i \tag{5.29}$$

$$\boldsymbol{P}_k^i = \boldsymbol{P}_{k-1}^i \tag{5.30}$$

Calculation of the Covariance Matrices: In order to determine the matrix $\boldsymbol{R}$, which is defined to be the same for all the FBG sets, the needle is driven along a constant curvature trajectory, and $\boldsymbol{R}$ is calculated using the curvature pair error values, $\boldsymbol{e}_a \in \mathbb{R}^{A\times 2}$, which are given as follows:

$$\boldsymbol{e}_a = \tilde{\boldsymbol{c}}_a - \frac{1}{A}\sum_{f=1}^{A} \tilde{\boldsymbol{c}}_f \tag{5.31}$$

where $a \in \{1, ..., A\}$, A being the total number of measurements for all of the FBG sets, and $\tilde{\boldsymbol{c}}_a \in \mathbb{R}^{1\times 2}$ the ath curvature pair measurement.

$\boldsymbol{Q}$ is defined as follows:

$$\boldsymbol{Q} = \xi \begin{bmatrix} \sigma_{\kappa_1}^2 & \sigma_{\kappa_1\kappa_2} \\ \sigma_{\kappa_1\kappa_2} & \sigma_{\kappa_2}^2 \end{bmatrix} \tag{5.32}$$

where $\sigma_{\kappa_1}^2$ and $\sigma_{\kappa_2}^2$ are the process error variances of the curvatures, which are assumed to be equal to each other, given that the PBN has a symmetric cross-section. ξ is a variable scaling parameter defined to scale the matrix at the first prediction step when a new FBG reaches the position, and it is used to give more weight to the newer measure:

$$\xi = \begin{cases} \rho, & \text{First prediction step of a new FBG} \\ 1, & \text{otherwise} \end{cases} \tag{5.33}$$

In order to collect data to be used to determine the unknowns of the matrix $\boldsymbol{Q}$, a steerable

needle instrumented with an optical fibre is inserted into a soft tissue phantom, and curvature values are collected from FBG sets throughout the insertion. The three unknowns, ρ, $\sigma^2_{\kappa_1}$ and $\sigma_{\kappa_1\kappa_2}$, the last of which is the co-variance of the curvature process error, are optimised with the interior point algorithm [14] so the mean tip position error between the ground truth and the reconstruction is minimised.

Although the curvature pairs are used as the state variables, curvature vectors, FBG strain values, or the ratios between wavelength shifts and Bragg wavelengths would also be suitable. This is because these are independent variables describing the state of curve points, and the shape can be reconstructed using the curvatures calculated using them, as explained in Section 5.2 and Section 5.3. However, strain and wavelength values are less intuitive for the intended use-case compared to others, and using curvature vectors would require tuning three elements of matrix $\boldsymbol{Q}$ instead of two elements, as in this study, since the elements on the main diagonal (the curvature and the bending direction) cannot be assumed to be equal.

A single evaluation of shape reconstruction performance for an MCF with KF, sampled every 50 μm (20 Hz at 1 mm·s^{-1}) throughout the navigation process, running on an Intel(R) Core(TM) i7-10510U CPU @ 1.80 GHz - 2.30 GHz with MATLAB 2020b, takes an average of 23 ms in the presence of only the tip FBG set (before the other FBG sets reach the points created by the tip FBG set) and 88 ms in the presence of eight FBG sets, each of which is assumed to be 5 mm long.

5.4.4 Application to Needle Steering

When a PBN where all the segments contain an MCF is inserted into a soft tissue, each segment's shape can be reconstructed individually with the proposed method. Also, the shape of the PBN at t_k can be assumed to be always equivalent to that of the segment that is further ahead (i.e., the Leading Segment (LS)). However, it is proposed to integrate the curvature information from all the segments to increase accuracy by averaging the curvatures corresponding to each curve point of the PBN. It is assumed that the PBN is not exposed to any torsion. This assumption and the follow-the-leader assumption previously explained are considered ac-

ceptable according to the PBN-tissue interaction model developed and validated in [124]. This assumption is also valid for bevel-tip needles [1], [92], which are similar to each of the PBN segments.

Let $p \in \{1, ..., N_k^{PBN}\}$ correspond to discrete curve points along the PBN, where N_k^{PBN} is the total number of the curve points. Also, let the superscript $v \in \{1, ..., g_k^p\}$ denote the vth curve, created by one of the segment tips, of which one curve point corresponds to p, with g_k^p being the total number of the curves. This parametrization allows the reconstruction to complete successfully if the segments tips are not aligned, a configuration that is essential to create curvature.

Therefore, the corresponding curvatures for all PBN curve positions are averaged to calculate the resultant curvatures along the PBN.

Considering a PBN's curvilinear navigation, a path-dependent discrepancy is expected between the segments' navigation lengths because of the separation between their neutral axes. A similar discrepancy is also expected between the curves created by the segment tips. Therefore, this discrepancy must be taken into account when matching the corresponding curvatures along the PBN. This issue was discussed by Watts *et al.* in [124], where they proposed an open-loop compensation method for the case where the curve points of the PBN centreline are known, which is the inverse of what is available in this study, where the curve points of the individual segments are known. Therefore, their algorithm was adapted with additional steps in this study to compensate for this discrepancy and, thus, match the steps of individual curves corresponding to curve points along the PBN. The updated algorithm is given in Algorithm 8.

Let $\boldsymbol{d}_h \in \mathbb{R}^{2\times1}$ be the neutral axis discrepancy of the hth segment, $h \in \{1, 2, 3, 4\}$, as shown in figure 3.1 on page 57 and $\hat{\boldsymbol{c}}_k^{i,h} \in \mathbb{R}^{2\times1}$ be the curvature value pair of the hth segment's i^{th} curve point. Therefore, the curves' curvature pairs corresponding to PBN curve points are calculated with Algorithm 8, and the curvature pairs, $\bar{\boldsymbol{c}}_k^{PBN,p} \in \mathbb{R}^{2\times1}$, of the PBN are calculated by averaging the curvature pairs corresponding to PBN curve points:

Algorithm 8 An algorithm to calculate PBN curvature pairs by matching the curve points of individual curves. All the parameters are for the discrete time step, t_k

Input: Neutral axis separations: $\boldsymbol{d}_h$, $h \in \{1, 2, 3, 4\}$, Curvature value pairs: $\hat{\boldsymbol{c}}_k^{i,h}$, The total number of curve points of the curves created by the segment tips: N_k^h

Output: g_k^p, and all the curves' curvature pairs corresponding to PBN curve points: $\boldsymbol{c}_k^{\upsilon,p}$

$l_h = N_k^h + \sum_{i=1}^{N_k^h}(\boldsymbol{d}_h \cdot \hat{\boldsymbol{c}}_k^{i,h})$ {Corresponding length of curve h at PBN centreline}
$L =$ Index of Max(l_1, l_2, l_3, l_4) {Leading segment}
$T_h = 0$
for all p **do**
  $g_k^p = 0$ $\{N_k^{PBN} = N_k^L\}$
  $\upsilon = 0$
  for $h = 1, 2, 3, 4$ **do**
    $T_h = T_h + (1 - \boldsymbol{d}_h \cdot \frac{\hat{\boldsymbol{c}}_k^{p,L}}{\|1+\hat{\boldsymbol{c}}_k^{p,L} \cdot \boldsymbol{d}_L\|})(1 + \boldsymbol{d}_L \cdot \hat{\boldsymbol{c}}_k^{p,L})$
    if $N_k^h \geq T_h$ **then**
      $g_k^p = g_k^p + 1$
      $\upsilon = \upsilon + 1$
      $\boldsymbol{c}_k^{\upsilon,p} = \hat{\boldsymbol{c}}_k^{round(T_h),h}$
    end if
  end for
end for

$$\bar{\boldsymbol{c}}_k^{PBN,p} = \frac{1}{g_k^p} \sum_{\upsilon=1}^{g_k^p} \boldsymbol{c}_k^{\upsilon,p} \tag{5.34}$$

Finally, the PBN shape is reconstructed with the resultant curvature pairs, $\bar{\boldsymbol{c}}_k^{PBN,p}$, based on the PTF-based method given in Section 5.3.3 because of its stability and noise handling capabilities, making it advantageous over the other methods, as suggested in [49]. When reconstructing, each curvature pair was set to correspond to the midpoint of two consecutive discrete arclength positions (s and $s + \Delta s$ as seen in (5.15)) and was used in the constant twist matrix between them.

5.4.5 Calibration and Curvature Value Correction

Firstly, calibration is required to determine the FBG wavelengths at zero-strain, which are to be used as Bragg wavelengths in (5.3). These are determined by placing the fibre into a linear guide. Secondly, calibration is needed to determine the angular position of the 1st core

with respect to the local frame as denoted by θ in figure 5.1 on page 99. This is determined by placing the fibre into a 2D curved guide with a known bending direction (figure 3.13 on page 69). This is repeated 4 times towards the 4 main directions (leftward, upward, rightward, downward) which correspond to 0°, 90°, 180°, and 270° bending angles of the local reference frame, and the averaged θ is used for increased accuracy.

Additionally, as proposed in [49], since the photo-elastic coefficient, p_e, could be biased, a correction parameter, $c_{correct}$, is determined to calculate the curvature values more accurately, as follows:

$$\kappa_{real} = c_{correct}\kappa_{measured} \tag{5.35}$$

The parameter, $c_{correct}$, is determined for each of the FBG sets separately by placing the fibre in 2D curved guides with known curvatures (κ_{real}) and comparing it with the ones obtained from FBG measurements ($\kappa_{measured}$). Therefore, $c_{correct}$ and the angle θ (the angular offset from the x axis of the local frame to the 1st core - figure 5.1 on page 99) can be determined simultaneously. This calibration procedure needs to be performed for each fibre only once after fibre-needle fixation.

5.5 Simulations

According to Henken *et al.* [46], shape errors are lowest with cubic spline interpolation, which was used in this simulation study. The shape was reconstructed with the interpolation of the strain values corresponding to virtual FBG set locations. Several simulations were performed to show the advantages of the proposed method over the methods requiring interpolation in a noise-free environment. A steerable needle is assumed to be driven into three different shapes consisting of two parts with zero torsion along their length. The radius of curvature of the first parts is 90 mm. The radius of curvature of the second parts, which are in planes perpendicular to the first segments, is 120 mm.

Shape 1: both two parts are 49 mm long,

Shape 2: the first part is 44 mm long, and the second part is 54 mm long,

Shape 3: the first part is 54 mm long, and the second part is 44 mm long.

At each time instant during the insertions, the ground truth curvatures and strain values corresponding to the virtual FBG sets' locations are considered to be the measurements obtained from these.

5.5.1 Shape Reconstruction with Interpolation

Eight virtual pointwise FBG sets were modelled with 14 mm centre-to-centre distances. The simulation flow chart is given in figure 5.6 on the next page. The curvatures and the strain values corresponding only to the 8 virtual FBG set locations on the ground truth curve were used. These FBG sets are illustrated in figure 5.7 on the following page along with the 3 shapes. These pointwise values were interpolated, and the PTF method was used for shape reconstruction since it is advantageous over the other methods, as described in Section 5.4.4. Lastly, the tip positions of the reconstructed curves were compared with that of the ground truths.

Another simulation study was conducted to understand the effect of imprecise placement of

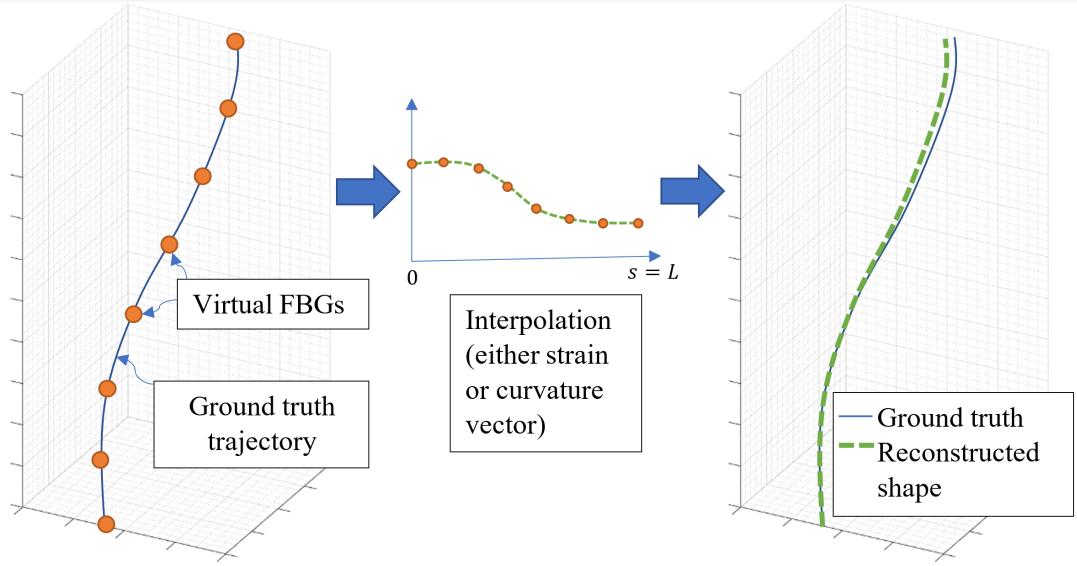

Figure 5.6: Shape Reconstruction with a Method Requiring Interpolation.

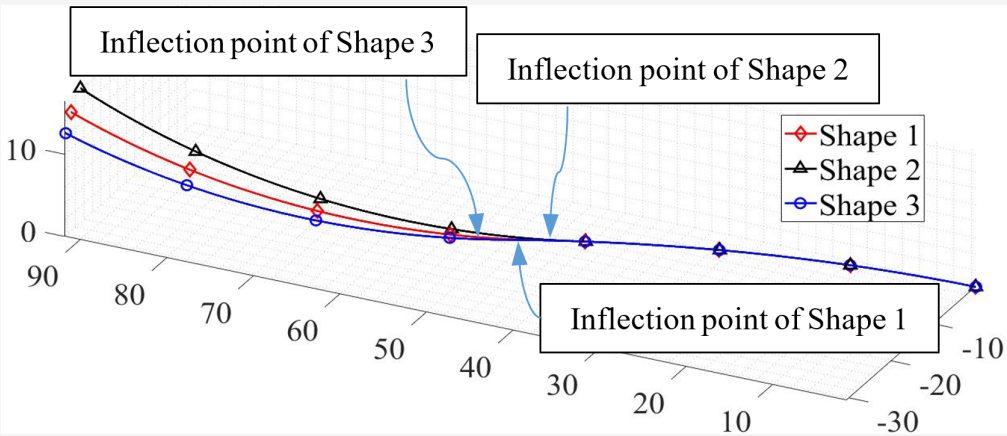

Figure 5.7: Illustration of the three shapes with the virtual FBG sets used in the simulation study. Markers represent the locations of the pointwise FBGs. Dimensions are in millimeters.

fibres to the tip position reconstruction accuracy when the interpolation-based method is used. Error is expected to occur if the faulty placement of the fibres causes a wrong curvature measurement, which happens if imprecise placement causes an FBG set to be interpreted to be on the wrong side of an inflection point. To analyse this, a simulation similar to the one above was conducted. This time the needle was assumed to be inserted into a 3D shape consisting of two 60 mm parts and had zero torsion along its length. The first part's radius of curvature was 150 mm. The radius of curvature of the second part, which was in a plane perpendicular

to the first one, was 200 mm. It was again assumed that an MCF consisted of 8 pointwise FBGs. The shape was reconstructed, and the tip position error was calculated when there was 50 μm for FBG_5 to pass the inflection point. Then, it was again calculated assuming a 100 μm placement error, which caused all the FBG sets to be interpreted to be at the wrong locations and specifically FBG_5 to be on the other side of the inflection point.

5.5.2 Shape Reconstruction with the Proposed Method

A simulation using the proposed method was conducted with only one pointwise FBG set at the fibre tip with an insertion speed of 1 mm·s^{-1} and a sampling frequency of 100 Hz, which results in sampling at each 10 μm of the insertion trajectory. No interpolation or curve fitting was used. Also, since the simulation was conducted in a noise-free environment, the KF was not used.

5.5.3 Results and Discussion

The results of the simulations conducted to compare the interpolation-based method and the proposed method are given in Table 5.1. The small error of the reconstruction without interpolation is clearly due to the high sampling frequency throughout the insertion trajectory.

Table 5.1: Simulation study tip position errors in mm when a steerable needle is driven into the three shapes.

	Shape 1	**Shape 2**	**Shape 3**
Shape reconstruction with interpolation	0.6	3.26	1.65
Shape reconstruction with the proposed method	0.048	0.094	0.040

The simulation results show that both the interpolation method and the positions of angle discontinuities along a fibre significantly influence the tip position error. The reconstruction error of Shape 1 is significantly lower than that of the others because the inflection point of this shape corresponds to the midpoint between two consecutive FBGs, as seen in figure 5.7, which led to better interpolation performance. By eliminating these uncertainties, shape reconstruction with the proposed method has resulted in the tip position error being decreased

to a negligible level in a noise-free simulation environment.

The results of the simulation study conducted to understand the effect of imprecise placement of fibres are given in Table 5.2. Although the error difference seems to be 239 μm, it was seen that the reconstructed shape flipped to the other side of the ground truth because of the change in the data obtained from FBG_5, which was one of the eight measurements used for interpolation. Note that this kind of behaviour is not only related to fibre placement, and it is also expected to occur when an FBG passes by an inflection point during insertion. The method proposed in this study is not prone to such instabilities.

Table 5.2: Results of the simulation study conducted to understand the effect of imprecise positioning of MCFs - Tip position reconstruction errors in mm.

No MCF-placement error	100 μm MCF-placement error
3.648	3.887

Also, no reconstruction error caused by imprecise fibre placement is expected with the interpolation-based method if the faulty fibre placement does not cause an FBG set to be interpreted to be on the wrong side of an inflection point. The reason for this is that the shape used in this study consists of constant curvature profiles between its inflection points, which is why no change is expected with the 8 FBG measurements if the imprecise fibre placement does not cause an FBG set to be interpreted to be on the opposite side of an inflection point.

5.6 Experiments

In vitro and *ex vivo* tests were conducted to validate the proposed shape reconstruction methods. Two error measures were defined to quantify performance, as follows:

1. The absolute difference between the tip of the reconstruction and the corresponding ground truth point:

$$e_{pos}^{tip} = \left\| \boldsymbol{\gamma}_{recon}^{tip} - \boldsymbol{\gamma}_{gt}^{tip} \right\| \tag{5.36}$$

   where the "gt" subscript is for "ground truth", and $\boldsymbol{\gamma}_{gt}^{tip}$ is the ground truth point corresponding to the reconstructed tip point $\boldsymbol{\gamma}_{recon}^{tip}$

2. The absolute angular difference between the orientations at the tips of the ground truth and the reconstructed curve:

$$e_{o}^{tip} = cos^{-1}\left(\frac{\boldsymbol{r}_{gt}^{tip} \cdot \boldsymbol{r}_{recon}^{tip}}{\left\| \boldsymbol{r}_{gt}^{tip} \right\| \left\| \boldsymbol{r}_{recon}^{tip} \right\|} \right) \tag{5.37}$$

   where $\boldsymbol{r}_{recon}^{tip}$ is the reconstructed tip orientation vector, and $\boldsymbol{r}_{gt}^{tip}$ is the ground truth orientation vector corresponding to the reconstructed tip orientation. Minimising this error is essential when the intervention, such as drug delivery or tissue ablation, must be performed at a given tip orientation [17]

The tip errors are expected to be the greatest because of the error accumulation in numerical integration.

5.6.1 Setup

The experiments were conducted utilising a clinically-sized, medical-grade, 4-segment PBN. The FBG data acquisition was performed with a sampling frequency of 50 Hz. In addition to the KF, a moving average filter using the data of 5 time steps was utilised to further mitigate the effect of noise.

Four EM sensors were used as ground truth in the experiments. Each segment of the PBN has 0.25 mm and 0.3 mm outer diameter lumens, which are used to accommodate the MCF and EM sensors, respectively. Four EM sensors were inserted into the segment lumens in such a way that each sensor was located at one of the segment tips.

The insertions were completed in such a way that there were always two aligned segments ahead of the other two so that the ground truth PBN tip position and orientation could be computed using the EM sensors attached to the leading segments.

To ease the positioning of the MCFs, the manufacturer was asked to mark the first and the last FBG locations. The marked FBG sets were seen through the PBN segments, which were not fully opaque. Therefore, a digital caliper was used to measure the distance between the PBN tip and the tip FBGs for precise placement. However, since the fibres were inside the segments when they were needed to be measured, there was no surface to apply the caliper against, which was thought to have created positioning errors up to 100 μm. The effect of this error was investigated in Chapter 5.5.

The PBN segments were actuated at a predefined speed of 1 mm·s^{-1} and actuation unit's encoders were used to determine n_k of each segment at each time step. The shape sensing software was developed in-house in MATLAB 2019b (MathWorks Inc). The *ex vivo* experimental setup is shown in figure 5.8 on the next page and the PBN during one of the gelatine experiments is captured in figure 5.9 on the following page.

The *in vitro* experiments were conducted in a gelatine soft tissue simulant, and the *ex vivo* experiments were conducted in *ex vivo* brain tissue to test the validity of the proposed methods. In both types of the experiments, the PBN was inserted into the soft mediums using the actuation unit so that it created the following shapes:

1. Single bend: this is a planar curved-shape with a 150 mm radius.
2. Double bend: this is a planar shape with 2 bends along its length. The radius of each bend is 150 mm.
3. 3D shape: this is similar to the one used in the simulation. It consists of two 60 mm parts

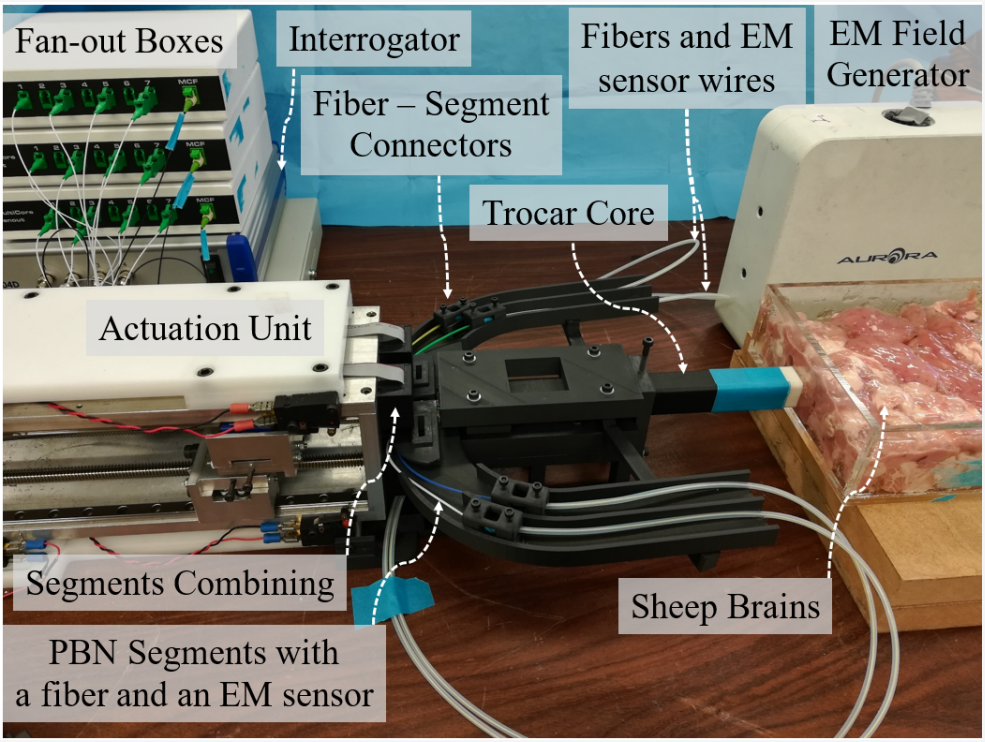

Figure 5.8: The *ex vivo* experimental setup used for shape sensing experiments

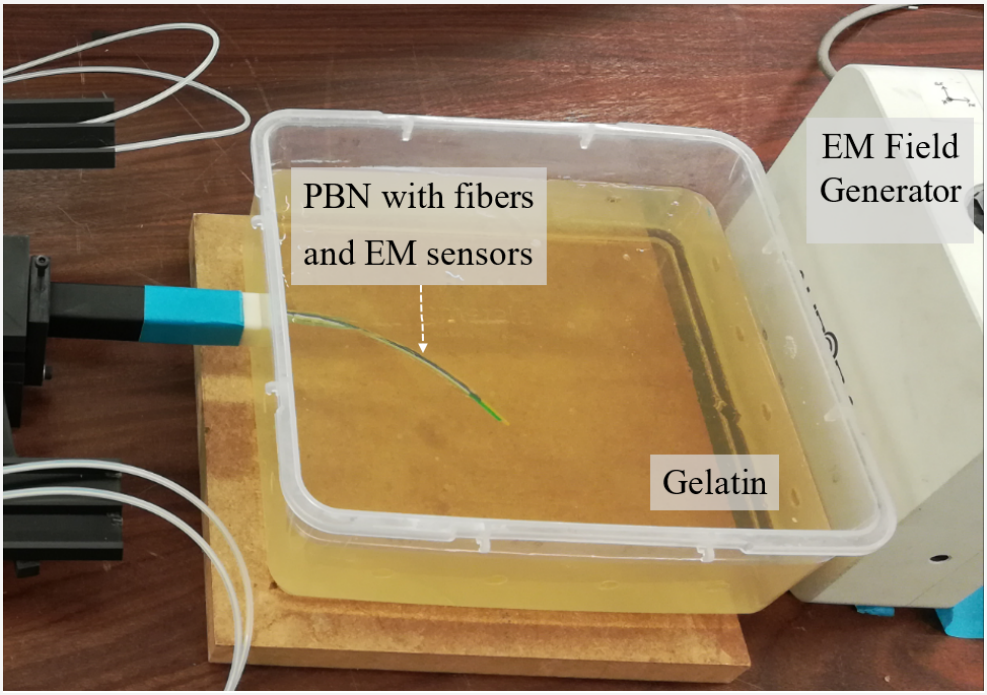

Figure 5.9: The *in vitro* experimental setup used for shape sensing experiments. The PBN navigating inside the gelatine phantom

and has zero torsion along its length. The first part's radius of curvature is 150 mm. The radius of curvature of the second part, which is in a plane perpendicular to the first one, is 200 mm.

Six insertion experiments (3 *in vitro* and 3 *ex vivo*) were conducted in total, and the PBN was reconstructed online. All the insertions were carried out to a depth of 120 mm, which is longer than the fibre's sensorized length. The tip position and orientation reconstructions for each PBN segment were compared with the ground truth data obtained from the EM sensor attached to the corresponding segment. Thus, validation was performed using the reconstructions of 24 single segments and 6 PBNs in total.

The gelatine phantom was produced from 7% by weight bovine gelatine, which mimics human brain tissue [33]. Sheep brains were purchased from a local butcher, and several of them were used to create a large enough volume for steering to become observable.

$\boldsymbol{R}$ was calculated via the method explained in Section 5.4.3, and the moving average filter used in the experiments was also taken into account in the determination of $\boldsymbol{R}$. In order to optimise $\boldsymbol{Q}$, the PBN instrumented with both optical fibres and EM sensors was inserted into a gelatine phantom in such a way that the PBN created a 3D shape. Then, $\boldsymbol{Q}$ and ρ were optimised with the interior point algorithm using MATLAB 2020b (MathWorks Inc) to minimise the tip position reconstruction error. As a result, the matrices and the scaling factor ρ were determined to be as follows:

$$\boldsymbol{R} = \begin{bmatrix} 0.21 & -0.15 \\ -0.15 & 0.26 \end{bmatrix} \mathrm{m}^{-2}, \quad \boldsymbol{Q} = \xi \begin{bmatrix} 2.21 & -0.85 \\ -0.85 & 2.21 \end{bmatrix} \mathrm{m}^{-2}$$

$$\rho = 2.04$$

The neutral axis separations were calculated using Dassault Systèmes SolidWorks:

$$\boldsymbol{d}_1 = \begin{bmatrix} 0.40 \\ 0.63 \end{bmatrix} \text{mm}, \quad \boldsymbol{d}_2 = \begin{bmatrix} -0.63 \\ 0.40 \end{bmatrix} \text{mm}$$

$$\boldsymbol{d}_3 = \begin{bmatrix} -0.40 \\ -0.63 \end{bmatrix} \text{mm}, \quad \boldsymbol{d}_4 = \begin{bmatrix} 0.63 \\ -0.40 \end{bmatrix} \text{mm}$$

The tip position reconstruction was also performed with an interpolation-based method to compare the proposed method's performance with a standard approach. The reconstruction was made on the basis of the PTF to use the same method as in the proposed approach after strain interpolation, which is preferred because of the advantages explained in Section 5.3.1. However, the shape could be reconstructed with the interpolation-based method only until an insertion length of 113 mm, as this value corresponds to the sum of the sensorized fibre length and lead-out length, l_{lead}, the last of which measured as 10 mm.

5.6.2 Results

The mean, standard deviation, and maximum of the tip errors for both PBN and individual segment reconstructions were calculated online at each time step over the 120 mm insertion and are presented in Table 5.3 and Table 5.4, for position and orientation, respectively. Figure 5.10 on the next page shows the PBN tip position reconstruction and the ground truth during the *ex vivo* experiment with the 3D shape. The single segment results cover all four segments of the PBN. The results of the reconstructions made with the interpolation-based method are given in Table 5.5. The comparison of the results of the proposed method with the interpolation-based method is given in figure 5.11 on page 126.

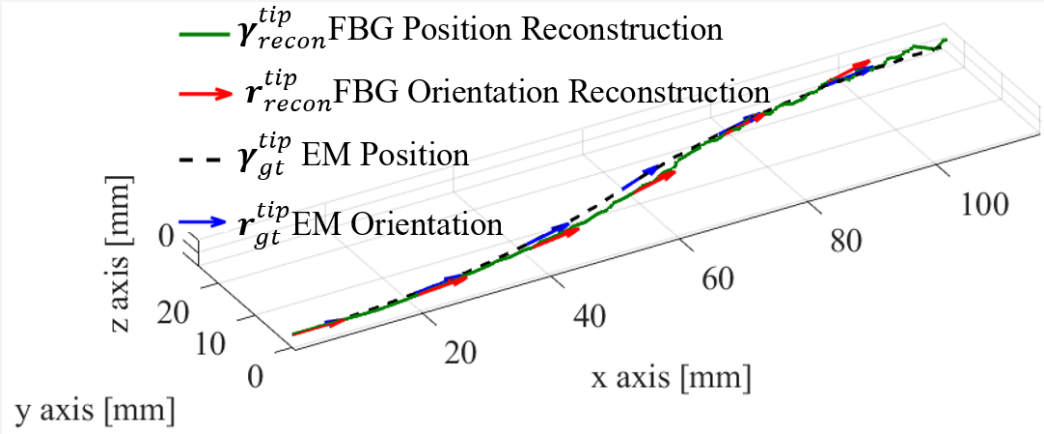

Figure 5.10: The EM sensor position measurements and the FBG-based tip pose reconstruction

Table 5.3: Mean ($\bar{e}^{tip}_{pos}$), standard deviation ($\sigma_{e^{tip}_{pos}}$) and maximum ($e^{tip}_{pos,max}$) of tip position errors $\bar{e}^{tip}_{pos}$ $(\sigma_{e^{tip}_{pos}})$ $[e^{tip}_{pos,max}]$ (mm)

		PBN (4 MCFs)		Single Segments (1 MCF)	
	Reconstruction with →	Tip FBG set	8 FBG sets	Tip FBG set	8 FBG sets
In vitro	Single Bend	2.03(1.33)[4.72]	1.01(0.51)[2.22]	3.69(1.69)[6.96]	1.77(0.98)[3.57]
	Double Bend	2.24(1.54)[5.10]	1.95(0.98)[4.62]	4.81(1.94)[8.71]	2.09(1.48)[4.99]
	3D Shape	3.08(1.70)[6.25]	2.18(1.30)[4.96]	5.16(2.35)[9.53]	2.95(1.65)[6.12]
Ex vivo	Single Bend	4.69(1.37)[7.12]	1.16(0.64)[2.71]	5.79(1.78)[9.30]	2.10(0.97)[4.05]
	Double Bend	5.60(2.70)[11.84]	2.04(1.01)[5.24]	6.93(2.93)[11.91]	2.27(1.33)[5.32]
	3D Shape	5.42(1.91)[9.95]	2.87(1.63)[5.76]	7.54(3.28)[11.46]	3.24(1.84)[6.87]

Table 5.4: Mean ($\bar{e}^{tip}_{o}$), standard deviation ($\sigma_{e^{tip}_{o}}$) and maximum ($e^{tip}_{o,max}$) of tip orientation errors $\bar{e}^{tip}_{o}$ $(\sigma_{e^{tip}_{o}})$ $[e^{tip}_{o,max}]$ (deg)

		PBN (4 MCFs)		Single Segments (1 MCF)	
	Reconstruction with →	Tip FBG set	8 FBG sets	Tip FBG set	8 FBG sets
In vitro	Single Bend	2.89(1.14)[5.57]	2.47(1.08)[4.19]	3.35(1.50)[6.86]	2.68(1.21)[5.33]
	Double Bend	3.11(1.88)[6.35]	2.51(1.49)[5.67]	3.60(2.12)[7.46]	2.96(1.99)[6.95]
	3D Shape	4.21(2.44)[7.26]	3.43(2.21)[6.41]	4.61(2.59)[8.38]	3.74(2.48)[7.64]
Ex vivo	Single Bend	3.18(2.08)[5.89]	2.33(1.60)[4.66]	4.18(2.59)[7.45]	3.52(2.54)[6.81]
	Double Bend	4.01(2.72)[7.10]	3.78(2.39)[6.71]	5.78(2.83)[10.94]	4.24(2.60)[8.22]
	3D Shape	4.48(2.84)[9.79]	3.84(2.76)[8.29]	6.66(3.01)[12.10]	5.45(2.90)[9.49]

Table 5.5: Tip position errors of single segment reconstructions with the interpolation-based method $\bar{e}^{tip}_{pos}$ $(\sigma_{e^{tip}_{pos}})$ $[e^{tip}_{pos,max}]$ (mm)

	In vitro	*Ex vivo*
Single Bend	2.54(1.16)[4.15]	2.86(1.27)[5.20]
Double Bend	3.66(2.25)[9.91]	4.06(2.76)[11.55]
3D Shape	5.24(2.33)[10.84]	6.1(3.64)[13.29]

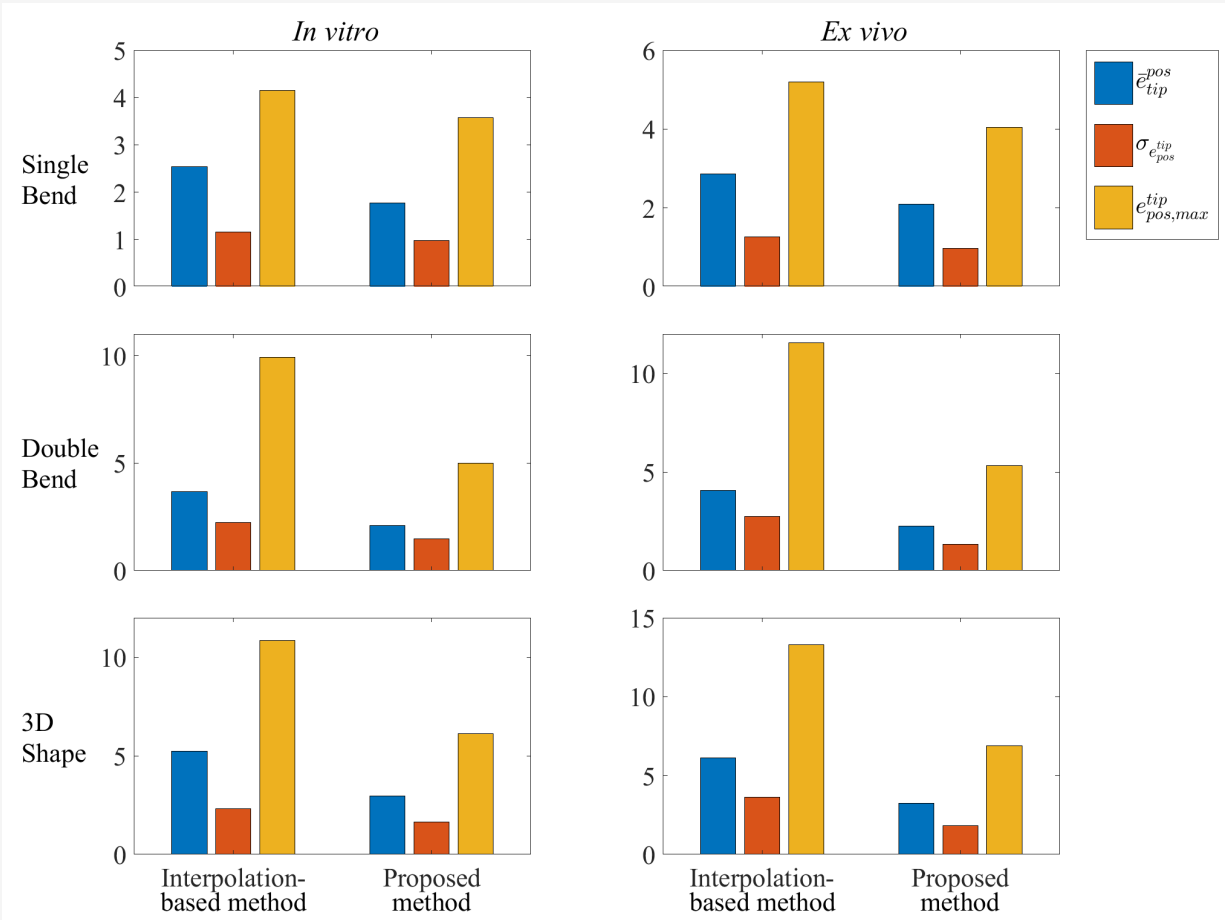

Figure 5.11: Comparison of the interpolation-based method and the proposed method - Tip position errors of single segment reconstructions [mm]

5.7 Discussion

The best experimental results were obtained using all the FBG sets of the fibres, which was expected. It is seen that in this case, the highest mean position error is 2.87 mm. When accounting for the 0.7 mm RMS error of the EM sensors, the total mean error, 3.57 mm, is in the clinically acceptable margin for tumours with 0.5 ml volume (assuming the tumour is spherical), the limit for clinically significant prostate tumours as reported in [6].

The error values obtained using 8 FBG sets are considerably lower than those obtained with only the tip FBG sets. This is probably because a higher number of FBG sets along a fibre enables better detection of curvature changes due to tissue deformation and leads to more accurate shape reconstruction. Thanks to the KF approach, the FBG sets other than the one at the tip are also used to correct the reconstruction constantly.

Results for the *in vitro* experiments are lower than those for the *ex vivo* experiments, as expected, because of the homogeneity of the soft tissue phantom compared to biological tissue. Navigating through the *ex vivo* tissue might have resulted in slight buckling of the PBN when penetrating tissue layers, and nonuniform deformation of the tissue, which would have affected the needle shape. These cases were accounted for, to a certain extent, by fusing the curvature information of the previously created points with those of new measurements. The results show that the FBG-based reconstruction method presented in this thesis is capable of dealing with tissue heterogeneity and tissue layers with different mechanical properties. Also, we expect that better results could be obtained with less compliant tissue such as the liver, which would provide better support for the needle to navigate in a follow-the-leader fashion, thanks to its higher stiffness.

The orientation error results are generally in agreement with the position errors. In comparison to the interpolation-based method, similar results were obtained in the case of the Single Bend shape. However, especially when looking at the maximum error values, the performance of the proposed approach seems to outperform the interpolation-based approach in the case of exper-

iments with 3D Shape and Double Bends, for which inflection points were shown to be one of the most significant error sources for the reconstruction methods requiring interpolation.

Compared to our previous work [54], where an FBG-based shape reconstruction method requiring interpolation was used for the dynamic reconstruction of a PBN, the mean tip position and orientation errors decreased significantly. When compared to the results in [53], where the needle shape was reconstructed statically, a higher mean error was obtained in this study. The lower accuracy may be due to the lower signal-to-noise-ratio in the dynamic reconstruction, tissue movements during the dynamic experiments, and the low refractivity of the MCFs produced with the Draw Tower Gratings (DTG) method. This method's advantage, providing durable fibres suitable for dynamic environments, comes at the cost of low refractivity compared to other production methods, such as the Phase Mask technique. Therefore, this leads to lower performance in wavelength detection and, accordingly, higher tip position error.

Another error source with the dynamic experiments can be that the fibres are fixed to the needle only at the needle base, which may not be sufficient to prevent relative motion between needle and fibre under strain. The resulting errors can be mitigated using a needle's mechanics model, such as [124] for PBNs.

Similar to single-core fibres [83], [46], imprecise placement of the MCFs along the needle may be another possible source of error.

Errors can also be attributed to calibration inaccuracies because, as in [49], small errors in wavelength in zero-strain and bending direction with respect to the 1st core, θ, accumulate throughout the MCF length, resulting in significant position error at the tip.

The sampling frequency along the navigation path can be increased to improve the shape reconstruction accuracy by decreasing the insertion speed or increasing the interrogator's sampling frequency. The single evaluation time of the algorithm and the experimental results show that the algorithm can work on an average PC with an adequate sampling frequency to run online.

Although a constant insertion speed was preferred in this study, since the number of curve points

created at each time step is computed using the navigation length, the method presented in this thesis allows navigation with other speeds or varying speeds for each PBN segment.

In this study, the torsion that the needle is exposed to was assumed to be negligible. However, considering the isotropic material structure of the PBN and the asymmetric forces and deformations that the PBN might have undergone during the navigation in heterogeneous soft tissue, the errors can also be attributed to this assumption. To reduce the resulting errors, a composite steerable needle could be used with a wire braid that is stiff in torsion and compliant in bending, as suggested in [98]. Alternatively, the torsion can be detected and accounted for using helically-wrapped optical fibres [38], [127].

Lastly, although the results in this chapter were obtained with a PBN, it is believed that they are representative of the performance of other steerable needle designs that operate in a follow-the-leader fashion, given that a single PBN segment can be considered as an independent bevel-tip steerable needle.

5.8 Conclusion

This study presented a novel method for FBG-based shape reconstruction of steerable needles where the needle tip creates the insertion trajectory and is followed by the rest, assuming a follow-the-leader insertion method. Instead of reconstructing the steerable needle's shape, it was proposed to reconstruct the trajectory created by the needle tip during insertion into soft tissue under the assumption that the needle shape and the trajectory created by the needle tip are equivalent. This leads to the possibility of shape reconstruction even in the presence of 1 FBG set only, located at the needle tip. This approach, independently of the number of FBG sets used, also removes the limit that the reconstruction length can only be so long as the length of the sensorized region which is, to the best of the author's knowledge, a first in FBG-based steerable needle shape reconstruction. Besides, a KF-based sensor fusion method was introduced to combine the sensory information of a specific location on the trajectory acquired at different times. A fusion method was also proposed for combining the sensory information from different sensors for the case where more than 1 FBG set is present along an MCF. The performance of the methods was assessed in both simulation and experiments with a clinically-sized PBN. The lead-out length, which is between the needle tip and the last FBG set, was taken into account, and the errors were calculated with respect to the PBN tip and PBN segment tips. *In vitro* and *ex vivo* dynamic experiments in both 2D and 3D were conducted to validate the proposed methods and demonstrate clinically acceptable tracking accuracy. Finally, the effect of bending direction discontinuities on shape reconstruction accuracy was investigated with a simulation study.

The shape sensing methods presented in this chapter were used to provide feedback to the closed-loop path-following controller given in the following chapter.

Chapter 6

3D Path-Following Control for Steerable Needles with Fibre Bragg Gratings in Multi-Core Fibres

6.1 Introduction

In this chapter, a novel design and implementation approach for path-following controllers of steerable needles is introduced. The needle-tissue interaction is highly unpredictable because of several anatomical reasons, such as tissue heterogeneity, boundaries of tissue layers, bleeding, all of which lead to difficulties in constructing an accurate mathematical model. When considering the control methods covered in Chapter 2, fuzzy and sliding mode controllers distinguish with their ability to deal with uncertainties. Sliding mode control, which was already used to control a Programmable Bevel Tip Steerable Needle (PBN) as given in the same chapter, is not ideal considering its long settling time [104]. On the other hand, fuzzy control is mainly based on human perception and experience, and controlling complex systems like PBN Low-Level Controllers (LLCs) require strong intuition for controller optimisation. Thus, the Active Disturbance Rejection Control (ADRC) [43] is chosen in this study as the control method to account for needle-tissue interactions, as it is known for its parameters having a wide adaptive range and its robustness even in the presence of a rough mathematical model of the system. The performance of ADRCs was shown previously using systems with unknown dynamics in hard-to-model environments, such as underwater vehicles [123], aerial vehicles [129], and autonomous grinding applications [24]. This control method is based on defining

unmodelled dynamics and disturbances ("total disturbance") as the extended state in addition to the system states and estimating them via the Extended State Observer (ESO). The estimated generalised disturbance is cancelled via a feedback controller, which helps transforming advanced control problems into simpler ones. In this study, both the Nonlinear Active Disturbance Rejection Control (NADRC), which includes nonlinear functions in the ESO, and the Linear Active Disturbance Rejection Control (LADRC), of which the ESO consists of linear functions, are investigated. In terms of High-Level Controller (HLC), to guide the needle along the desired path, a controller based on Nonlinear Guidance Law (NLGL) [80] is designed. This is a control method commonly used for path-following of fixed-wing Unmanned Aerial Vehicles (UAVs) [116], which has the same nonholonomic constraints as steerable needles including PBNs. Furthermore, An algorithm is proposed for programming the PBN tip while observing the permissibility condition of PBNs, i.e., a condition ensuring that the PBN acts as a single body at all times. Fibre Bragg Grating (FBG)-inscribed Multi-core Fibres (MCFs) have been used for feedback. To the best of the authors' knowledge, this is the first study investigating path-following control methods of steerable needles employing MCFs with FBGs. Also, this is the first experimental three dimensional (3D) path-following study of PBNs.

6.1.1 Publications

This chapter is from an edited version of the article:

- **Donder, A.**, Rodriguez y Baena, F. (**Under Review**). 3-D Path-Following Control of Steerable Needles with Fiber Bragg Gratings in Multi-Core Fibers. Submitted to IEEE Transactions on Robotics [26]

6.2 3D Kinematic Modelling of PBNs

One of the most common methods used to model nonholonomic systems, such as steerable needles, is the Parallel Transport Frame (PTF) [105], [110], which is used also in this study and satisfies the following frame equations.

$$\frac{d\boldsymbol{\gamma}(s)}{ds} = \boldsymbol{T}(s), \quad \frac{d\boldsymbol{T}(s)}{ds} = \kappa_1(s)\boldsymbol{N}_1(s) + \kappa_2(s)\boldsymbol{N}_2(s)$$

$$\frac{d\boldsymbol{N}_1(s)}{ds} = -\kappa_1(s)\boldsymbol{T}(s), \quad \frac{d\boldsymbol{N}_2(s)}{ds} = -\kappa_2(s)\boldsymbol{T}(s) \tag{6.1}$$

where $\boldsymbol{T}(s)$ is the unit tangent vector, and $\boldsymbol{N}_1(s)$, $\boldsymbol{N}_2(s)$ are the unit normal vectors. $\kappa_1(s)$ and $\kappa_2(s)$ describe the change of $\boldsymbol{T}(s)$ in the $\boldsymbol{N}_1(s)$ and $\boldsymbol{N}_2(s)$ directions at arc length position s and are calculated as follows:

$$\kappa_1(s) = \kappa(s)cos(\beta(s))$$

$$\kappa_2(s) = \kappa(s)sin(\beta(s)) \tag{6.2}$$

where $\kappa(s)$ and $\beta(s)$ are the curvature value and the bending angle, respectively. The PBN tip reference frame and the curvature pair are illustrated in figure 6.1 on the next page

One of the main advantages of the PTF over one of the other commonly used techniques, the Frenet-Serret Frame (FSF), is that the PTF is defined for every curve $\gamma \in$ **SE3** including zero curvature while the FSF requires a nonzero curvature to be defined.

Because of the mechanical properties of PBNs, the relationship between the relative offsets of PBN segments and $\kappa(s)$ is not the same in all bending directions. This characteristic has been addressed for 4-segment PBNs by several studies in the literature, such as [124], and [105].

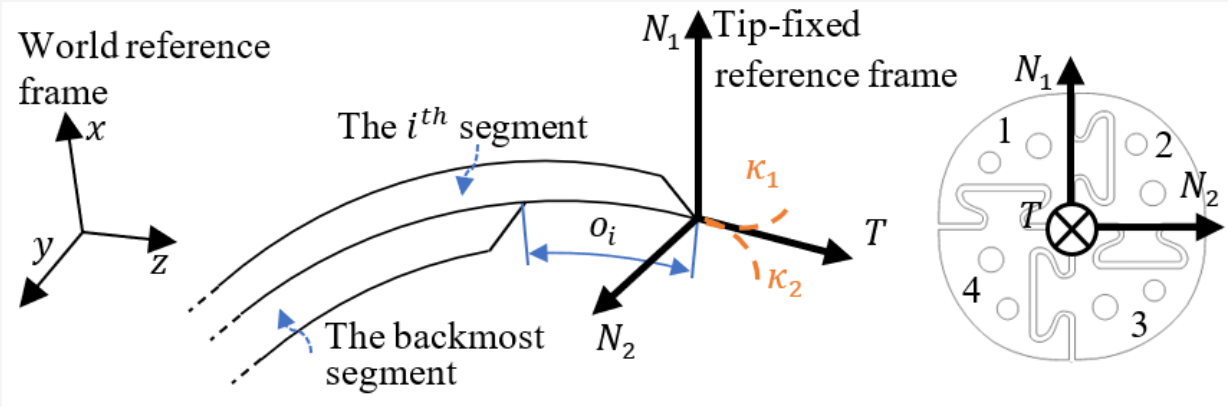

Figure 6.1: An illustration of the world reference frame, the PBN tip-fixed frame, which is fixed at the tip of the leading segment, and the curvature pair. Left: The PBN is illustrated two dimensional (2D) for clarity. o_i represents the relative offset of the ith PBN segment with $i \in \{1, 2, 3, 4\}$ (The relative offset of the backmost segment, the closest to the proximal end, is 0). Right: Cross-section view of a PBN with the frame at the tip. The segment numbers are shown on the segments

Because of its advantages for simple implementation, the latter has been adapted in this study, and is given as follows:

$$\dot{\boldsymbol{c}}_t = b\eta \boldsymbol{I}\ \boldsymbol{\Pi}\ \dot{\boldsymbol{o}}_t + \dot{\boldsymbol{\omega}}_t \tag{6.3}$$

where subscript t denotes the discrete time step, b is the control gain, which is unity in our system, $\boldsymbol{c}_t = \begin{bmatrix} \kappa_{1,t} & \kappa_{2,t} \end{bmatrix}^T \in \mathbb{R}^{2\times 1}$ is the estimated potential curvature pair at PBN tip (figure 6.1), $\eta \in \mathbb{R}$ is a constant optimised experimentally, $\boldsymbol{I}$ is a 2×2 identity matrix, $\boldsymbol{o}_t = \begin{bmatrix} o_{1,t} & o_{2,t} & o_{3,t} & o_{4,t} \end{bmatrix}^T \in \mathbb{R}^{4\times 1}$ denotes the relative offsets of PBN segments which are with respect to the backmost segment (i.e., the closest to the proximal end - figure 6.1), $\boldsymbol{\omega}_t \in \mathbb{R}^{2\times 1}$ is a nonlinear function representing general disturbance, and finally $\boldsymbol{\Pi} \in \mathbb{R}^{2\times 4}$ is given as:

$$\boldsymbol{\Pi} = \begin{bmatrix} cos(\theta_1) & cos(\theta_2) & cos(\theta_3) & cos(\theta_4) \\ sin(\theta_1) & sin(\theta_2) & sin(\theta_3) & sin(\theta_4) \end{bmatrix} \tag{6.4}$$

where $\theta_1 = \frac{\pi}{4} \pm \pi$, $\theta_2 = \frac{3\pi}{4} \pm \pi$, $\theta_3 = \frac{5\pi}{4} \pm \pi$, $\theta_4 = \frac{7\pi}{4} \pm \pi$ denoting the bending directions of the PBN segments.

In [105] it is stated that the general relationship between the relative segment offsets and the projected curvature in the orthogonal axes, which led to (6.3), was derived from experimental data by assuming that the model was linear and could be represented by the first order approximation of the Taylor's expansion.

The control gain b is included in (6.3) to account for the potential errors resulted from it being assumed to be unity.

6.3 Path-Following Controller

The purpose of the controller is to generate a PBN tip configuration that guides the needle throughout a predefined path, given the PBN-tip curvature pair and tip pose. The overall controller consists of two parts; a HLC and a LLC. The HLC generates desired curvature pairs, $\boldsymbol{c}_t^d = \left[\kappa_{1,t}^d, \kappa_{2,t}^d\right]^T$, defined in PBN tip frame, for the LLC, which then tracks them by manipulating the individual segments. The block diagram of the overall controller is given in figure 6.2.

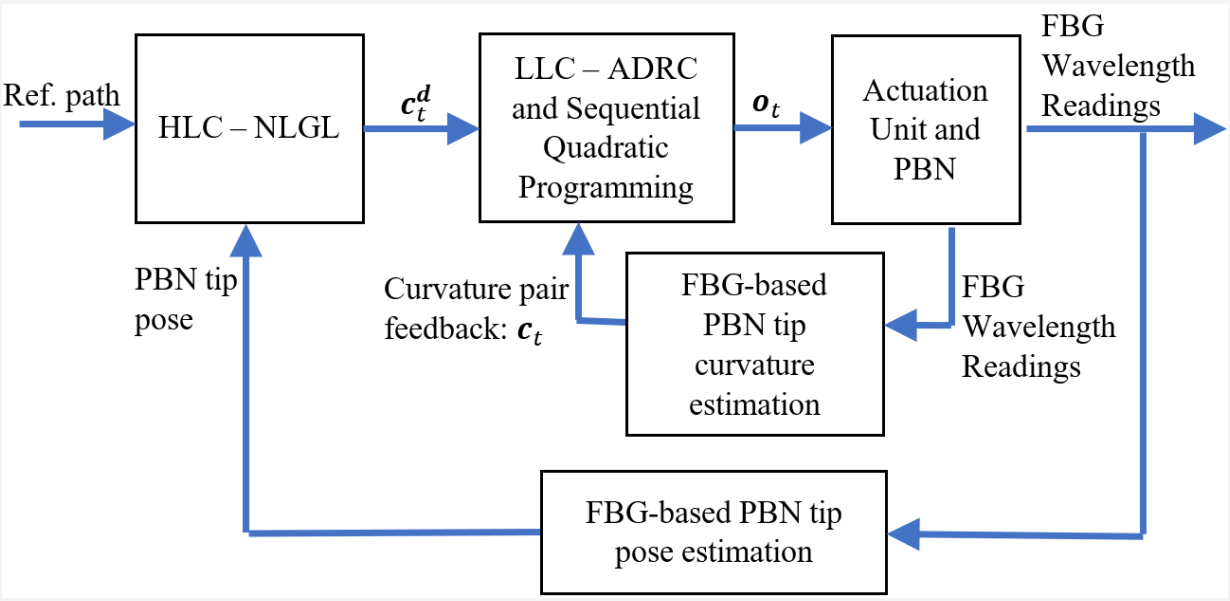

Figure 6.2: Overall path-following controller and data processing block diagram

6.3.1 High-level controller

Kinematic models of fixed-wing unmanned aerial vehicles and underwater vehicles are similar to steerable needles because of the same nonholonomic constraints. In this study, an NLGL-based path-following controller was implemented [80]. This method is based on defining a pseudo-target point, $\boldsymbol{p}_{s,t} \in \mathbb{R}^{3\times1}$, on the reference path at each time step, and estimating the desired curvature values for guidance. To define $\boldsymbol{p}_{s,t}$, a virtual sphere of radius r centred at the PBN tip is defined, as shown in figure 6.3 on the next page. Then, the further forward one of the two sphere - reference path intersection points along the path is defined as $\boldsymbol{p}_{s,t}$, which, thus,

guarantees smooth convergence. In the case where there is no intersection between the sphere and the reference path, $\boldsymbol{p}_{s,t}$ is defined as the point on the desired path closest to the sphere. This is followed by the calculation of the desired curvature pair, $\boldsymbol{c}_t^d$ as given in Algorithm 9.

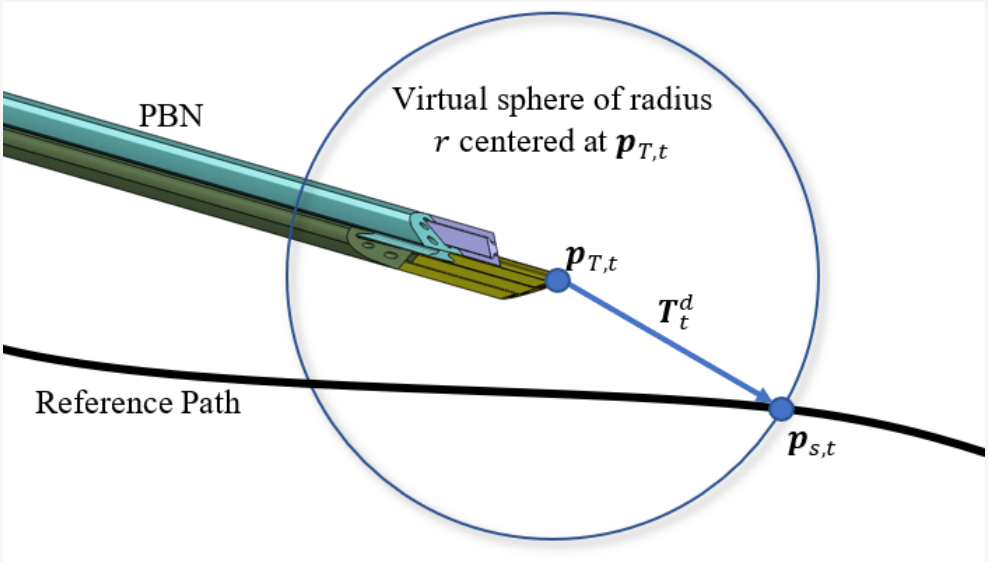

Figure 6.3: Illustration of the the NLGL

6.3.2 Low-level controller

In this section the process from the generation of the desired curvature pair, $\boldsymbol{c}_t^d$, to the completion of PBN tip programming, and the movement of the PBN with the programmed tip is given in three subsections: (i) ADRC to generate curvature control inputs, (ii) Sequential Quadratic Programming (SQP) to generate PBN segment offsets, (iii) PBN tip programming. The block diagram of the LLC is given in figure 6.4 on the following page.

6.3.2.1 Generation of Curvature Control Inputs

The ADRC is used to track the desired curvature pair, $\boldsymbol{c}_t^d$, generated by the HLC. The subscript t is omitted in this section for clarity, and all the variables are defined for time step t unless indicated otherwise.

Rewriting the model of the Multi-Input and Multi-Output (MIMO) system (6.3) in a more compact form:

$$\dot{\boldsymbol{c}} = b\,\boldsymbol{u} + \dot{\boldsymbol{\omega}} \tag{6.5}$$

Algorithm 9 HLC algorithm - all the positions and axes are defined with respect to the world reference frame.

Input: Reference Path, The radius of the virtual sphere: r, Needle tip position: $\boldsymbol{p}_{T,t} \in \mathbb{R}^{3\times1}$, Needle tip frame axes: $\boldsymbol{T}_t, \boldsymbol{N}_{1,t}, \boldsymbol{N}_{2,t} \in \mathbb{R}^{3\times1}$, Navigation length at each step: m (set manually)

Output: The desired curvature pair: $\boldsymbol{c}_t^d$

$n \leftarrow$ Number of intersection points of the sphere and the reference path
if $n = 2$ **then**
  $\boldsymbol{p}_{s,t} \leftarrow$The further forward intersection point along the reference path
else if $n = 0$ **then**
  $\boldsymbol{p}_{s,t} \leftarrow$The reference path point closest to the sphere
end if
$\boldsymbol{T}_t^d = \boldsymbol{p}_{s,t} - \boldsymbol{p}_{T,t}$
$\boldsymbol{N}_{1,t}^d = \boldsymbol{N}_{2,t} \times \boldsymbol{T}_t^d$
$\boldsymbol{N}_{2,t}^d = \boldsymbol{T}_t^d \times \boldsymbol{N}_{1,t}^d$
$\boldsymbol{X}_t = \begin{bmatrix} \boldsymbol{T}_t & \boldsymbol{N}_{1,t} & \boldsymbol{N}_{2,t} & \boldsymbol{p}_{T,t} \\ 0 & 0 & 0 & 1 \end{bmatrix}$ {Pose matrix}
$\boldsymbol{X}_t^d = \begin{bmatrix} \boldsymbol{T}_t^d & \boldsymbol{N}_{1,t}^d & \boldsymbol{N}_{2,t}^d & \boldsymbol{p}_{s,t} \\ 0 & 0 & 0 & 1 \end{bmatrix}$ {Desired pose matrix}
$\boldsymbol{A}_t = \ln(\boldsymbol{X}_t^{-1}\boldsymbol{X}_t^d)/m$ {Twist matrix}
$\boldsymbol{c}_t^d = \begin{bmatrix} 0 & 1 & 0 & 0 \\ 0 & 0 & 1 & 0 \end{bmatrix} \boldsymbol{A}_t \begin{bmatrix} 1 & 0 & 0 & 0 \end{bmatrix}^T$

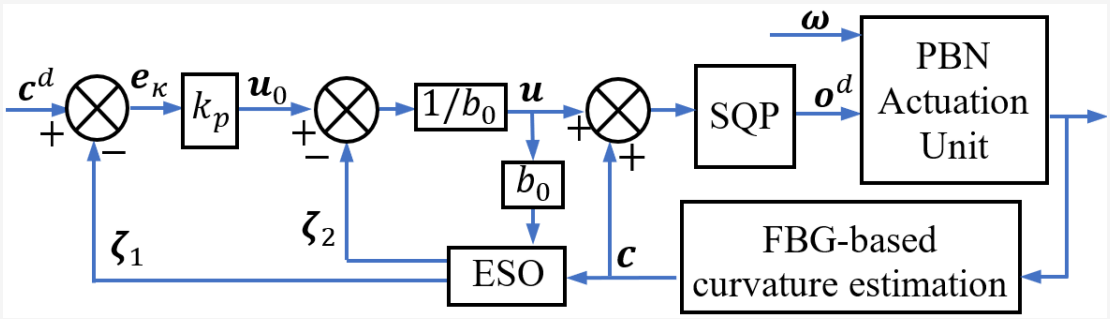

Figure 6.4: Overall LLC block diagram (subscript t is omitted for clarity)

where $\boldsymbol{u} = \eta \boldsymbol{I}\ \boldsymbol{\Pi}\ \dot{\boldsymbol{o}}$.

Both a linear ESO, which is similar to Luenberger observer [66], and a nonlinear ESO have been designed to estimate the system state $\boldsymbol{c}$ and the total disturbance (i.e., the extended state), which are tracked with $\boldsymbol{\zeta}_1 \in \mathbb{R}^{2\times1}$ and $\boldsymbol{\zeta}_2 \in \mathbb{R}^{2\times1}$, respectively.

$$\boldsymbol{\zeta}_1 \approx \boldsymbol{c}, \qquad \boldsymbol{\zeta}_2 \approx (b - b_0)\boldsymbol{u} + \dot{\boldsymbol{\omega}} \tag{6.6}$$

with b_0 being the estimation of the control gain b. $\boldsymbol{\zeta}_1$ is the estimation of the curvature pair, $\boldsymbol{c}$, and $\boldsymbol{\zeta}_2$ is the estimations of the total disturbance, which is the combination of the disturbance caused by the control gain's estimation error and the derivative of disturbance, $\dot{\boldsymbol{\omega}}$, as defined in (6.3). The potential factors causing disturbance could include the heterogeneity of the tissue in which the PBN is inserted, nonuniform friction between PBN segments, tissue displacements during needle navigation, and the tendon-driven effect caused by the wires of proprioceptive sensors placed away from the neutral axis of the PBN segments. The elimination of these uncertainties are the main motivation of using a closed-loop controller and are actively compensated by the ADRC in this study. The stability analysis for the LADRC is given in Appendix, and readers may refer to [62] for the stability analysis of the NADRC.

The control law is given as:

$$\boldsymbol{u} = \frac{\boldsymbol{u}_0 - \boldsymbol{\zeta}_2}{b_0} \tag{6.7}$$

Therefore, disturbances are assumed to be eliminated provided that they vary slowly, and (6.5) can be simplified as $\dot{\boldsymbol{c}} \approx \boldsymbol{u}_0$ where the controller output $\boldsymbol{u}_0 \in \mathbb{R}^{2\times 1}$ is defined as follows:

$$\boldsymbol{u}_0 = k_p \, \boldsymbol{e}_\kappa \tag{6.8}$$

where k_p is the proportional controller gain, and $\boldsymbol{e}_\kappa = \boldsymbol{c}^d - \boldsymbol{\zeta}_1$ denotes the error of the states.

The linear ESO is given in discrete form as follows:

$$\begin{cases} \boldsymbol{e} = \boldsymbol{c} - \boldsymbol{\zeta}_1 \\ \boldsymbol{\zeta}_{1,t+1} = \boldsymbol{\zeta}_1 + h(\boldsymbol{\zeta}_2 + b_0\boldsymbol{u} + \beta_1^L \boldsymbol{e}) \\ \boldsymbol{\zeta}_{2,t+1} = \boldsymbol{\zeta}_2 + h\beta_2^L \boldsymbol{e} \end{cases} \tag{6.9}$$

where h is the sampling period. β_1^L and β_2^L are given as $3\omega_0$ and $3\omega_0^2$, where ω_0 is the observer

bandwidth [40].

Similarly, the discrete nonlinear ESO is given as follows:

$$\begin{cases} \boldsymbol{e} = \boldsymbol{c} - \boldsymbol{\zeta}_1 \\ \boldsymbol{\zeta}_{1,t+1} = \boldsymbol{\zeta}_1 + h(\boldsymbol{\zeta}_2 + b_0\boldsymbol{u} + \beta_1^N fal(\boldsymbol{e}, \alpha_1, \delta)) \\ \boldsymbol{\zeta}_{2,t+1} = \boldsymbol{\zeta}_2 + \beta_2^N fal(\boldsymbol{e}, \alpha_2, \delta) \end{cases} \tag{6.10}$$

where β_2^N is a function of h and given as $\beta_2^N = 2/(5^2 h^{1.2})$, and $fal(.)$ is a nonlinear function as follows:

$$fal(\boldsymbol{e}, \alpha, \delta) = \begin{cases} \boldsymbol{e}/(\delta^{1-\alpha}), & |\boldsymbol{e}| \leq \delta \\ |\boldsymbol{e}|^{\alpha} sign(\boldsymbol{e}), & |\boldsymbol{e}| > \delta \end{cases} \tag{6.11}$$

where $\alpha \in \mathbb{R}_{<1}$ is a parameter to be optimised experimentally with δ. Readers may refer to [43] for more information about definitions of ADRC parameters.

6.3.2.2 Generation of PBN segment offsets

The incremental curvature commands, $\boldsymbol{u}$ are added with feedback curvature values, $\boldsymbol{c}$, and mapped into the desired relative offsets of the PBN segments, $\boldsymbol{o}^d$, via SQP technique, which was originally proposed in [104], and summarised here for completeness:

$$min\ \mathbf{J} = \frac{1}{2}\boldsymbol{o}^T \boldsymbol{Q} \boldsymbol{o} \tag{6.12}$$

with constraints

$$\begin{cases} \boldsymbol{u} + \boldsymbol{c} = \eta \boldsymbol{I}\ \boldsymbol{\Pi}\ \boldsymbol{o}_t \\ o_i \leq o_{max} \end{cases} \tag{6.13}$$

where $\boldsymbol{Q}$ is the weight matrix of the PBN segments, and o_{max} is the maximum allowed relative distal offset according to the physical limitations of the PBN (i.e, the limitation to eliminate

the risk of separation of segments).

6.3.2.3 PBN Tip Programming

In the last step, an actuation unit drives the PBN segments to program the PBN tip according to the desired segment offsets, $\boldsymbol{o}^d$, as given in Algorithm 10, which is explained in this section.

At the end of the programming, it is desired to have the same PBN tip position as in the beginning. Besides, the PBN tip should be kept fixed even during the programming to eliminate re-insertion and to decrease tissue damage. To this end: (i) If the Leading Segment (LS) should remain unchanged (the segment with the highest o^d is the same as the current leading one), it is kept fixed while others move to meet $\boldsymbol{o}^d$, (ii) otherwise, the desired LS, L^d, is driven next to the current LS, L, and the segments other than L^d are arranged such that the resulting relative offsets satisfy $\boldsymbol{o}^d$. L is not pulled back before L^d is driven next to it with or without one of the other two segments (in the case of a 4-segment PBN). The reason why another segment might be required to be driven next to L is to satisfy the permissibility conditions of PBNs [124], e.g., two Diagonal Segments (DSs) not to be driven forward (together or individually) in the case when they are ahead of the other two.

The desired insertion lengths of the PBN segments, which are some of the inputs of Algorithm 10, are calculated using the current insertion lengths and $\boldsymbol{o}^d$ by considering the discrepancy between the distal and the proximal offsets, which is expected to occur when the PBN follows a curvilinear path. To account for this, the method proposed in [124] (Section V.C) is used and the details are not given in this study.

Also taking into account the limitations of the actuation unit, the segment speeds are empirically set to ν_s, which was found to be appropriate to minimize tissue damage and operation time.

Finally, when the programming is completed, all the segments are pushed forward with the speed of ν_{all} for a distance of m, which is set manually, to realise the desired curvature. The speed, ν_{all}, is selected to be less than ν_s given that the tissue damage is expected to be higher

when all the segments are driven into the tissue at the same time [61].

Algorithm 10 The PBN tip programming algorithm for a 4-segment PBN satisfying the permissibility conditions [124] - The commands at each step are performed simultaneously.

Input: Current LS: L, desired LS: L^d, the segment located at the diagonal of L (not one of the neighbouring segments): D, the segment located at the diagonal of L^d: D^d, The desired insertion lengths of the PBN segments.

1: $S_1, S_2 \leftarrow$ The segments other than L and D
2: **if** $L^d = L$ **then**
3: **if** D is desired to move backward **then**
4: Retract D to the desired length,
 Position S_1 and S_2 to the desired length that the one to be back moves after the other one finishes
5: **else**
6: Position S_1 and S_2 in the way given in line 4
7: Drive D to the desired length
8: **end if**
9: **else if** $L^d = D$ **then**
10: $S_a \leftarrow$ The further extended one of S_1 and S_2
11: $S_b \leftarrow$ The hind one of S_1 and S_2
12: Drive S_a forward till the tip of L,
 Drive L^d forward till the tip of S_a
13: Retract L to the desired length,
 Position S_b to the desired length,
 Retract S_a to the desired length
14: **else**
15: Drive L^d to the desired length
16: Position D to the desired length,
 Position D^d to the desired length
17: Retract L to the desired length
18: **end if**

6.4 Simulations and Parameter Optimisation

The developed control methods were initially tested with a series of simulations, by means of which the controller parameters were optimised with the interior point algorithm [13] in MATLAB. The methods given in Section 6.2 were used to model the needle steering. Eight point-wise virtual FBG sets with 14 mm separation were modelled, and white Gaussian noise was added to the calculated curvature values to imitate the FBG measurement noise. An error measure, the absolute difference between the PBN tip position and the ground truth, was defined to quantify the performance, as follows:

$$e_{pos} = \|\boldsymbol{\gamma}_{tip} - \boldsymbol{\gamma}_{gt}\| \tag{6.14}$$

where $\boldsymbol{\gamma}_{tip}$ is the reconstructed PBN tip position, and $\boldsymbol{\gamma}_{gt}$ is the ground truth of the tip position. The 3D reference path used in the simulations consists of 3 parts, and it is given in figure 6.5 on the next page and Table 6.1. The results of the simulations using linear ESO and nonlinear ESO are given in figure 6.5 on the following page, figure 6.6 on the next page, and Table 6.3, which were conducted using the finalised controller parameters given in Table 6.2. When optimising the parameters, the step navigation length, m, was constrained with $m \geq 5$ mm to achieve a reasonable insertion duration. In the simulations, the initial position of the PBN was 1.5 mm off-path in both x and y directions.

With regards to the simulation results (figure 6.5 on the following page, figure 6.6 on the next page, Table 6.3), no recognisable difference was seen between the performances of the controllers with nonlinear ESO and linear ESO. The convergence to the path, in both cases, was achieved after approximately 20 mm navigation, and the error stayed below 0.5 mm along the rest of the path.

Finally, when compared to the sliding-mode LLC presented in [104], the settling time was lowered in this study by keeping the steady state error in the acceptable margin.

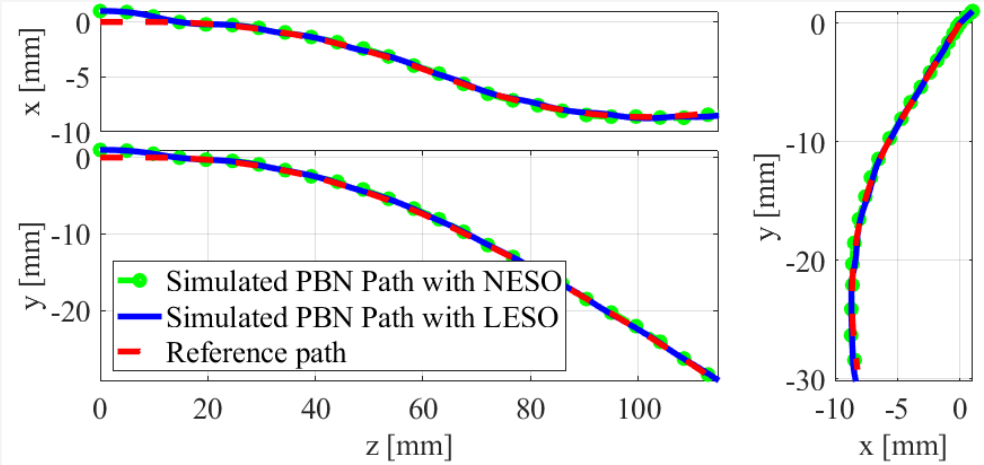

Figure 6.5: Path planning simulation results with initial perturbation of 1 mm in x and y directions, and illustration of the 120-mm 3D path used in the simulations and experiments

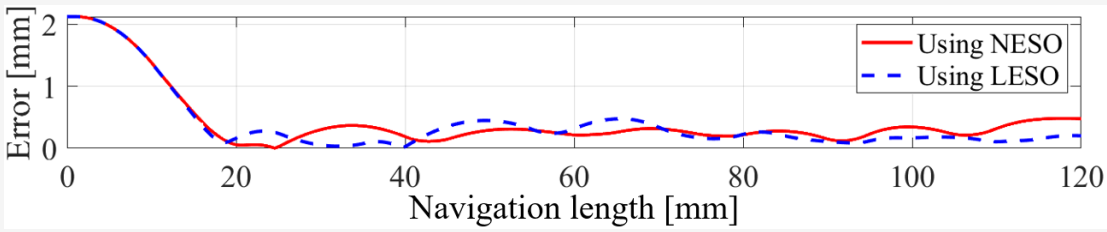

Figure 6.6: Absolute position error, e_{pos}, of simulated PBN paths with initial perturbation of 1.5 mm in x and y directions

Table 6.1: The 3 parts of the desired path - The bending plane orientation is with respect to the tip frame's $\boldsymbol{N}_1$ axis

	Length [mm]	Curvature [1/m]	Bending Plane Orientation [°]
Section 1	10	Constant: 0	0
Section 2	55	Constant: 6.67	15
Section 3	55	Constant: 5	105

Table 6.2: Controller Parameters for Simulations

NLGL - LADRC

r	k_p	$\boldsymbol{Q}$	h	o_{max}	ω_o	m
5 mm	2.48	$\boldsymbol{I}$	0.076 s	30 mm	1.32	5 mm

NLGL - NADRC

r	k_p	$\boldsymbol{Q}$	h	α_1	α_2	δ	m	β_1^N	o_{max}
4 mm	3.4	$\boldsymbol{I}$	0.11 s	0.7	0.45	0.56	5 mm	1.74	30 mm

Table 6.3: Path-Following Simulation Results (without initial perturbation) - Absolute position error, e_{pos}, over 120 mm insertion length [mm]: Mean: $\bar{e}_{pos}$, Standard Deviation: $\sigma_{e_{pos}}$, Maximum: $e_{pos,max}$, Target error: $e_{pos,target}$

	$\bar{e}_{pos}$	$\sigma_{e_{pos}}$	$e_{pos,max}$	$e_{pos,target}$
NLGL - LADRC:	0.17	0.11	0.42	0.16
NLGL - NADRC:	0.26	0.13	0.54	0.32

6.5 Experimental Evaluation

In this section, details about the experimental methods are provided. In addition to the path-following experiments, target-hitting experiments, where the virtual target moves, were also conducted to assess the proposed control method's performance in the case where target migration occurs as a result of tissue movement.

In total, 6 *ex vivo* and 12 *in vitro* path-following, and 6 *in vitro* target-hitting experiments were conducted. The *Ex vivo* tests were performed in sheep brains that were placed in a tissue phantom, as seen in figure 6.7 on page 148. The *ex vivo* tissue was purchased from a local butcher, and several of the brains were used to create enough volume for steering. On the other hand, a gelatine phantom produced from from 7% by weight bovine gelatine, an approximation for human brain [33], was used as a soft-tissue stimulant for the *in vitro* tests.

The navigation speeds, ν_{all} and ν_s, were selected as 1 mm/s and 5.5 mm/s respectively, as recommended in [70] for neurosurgery. All the parameters used in the experiments are given in Table 6.4.

Table 6.4: Controller Parameters for Experiments

	r	k_p	$\boldsymbol{Q}$	h	o_{max}	ω_o	m	η_s	η_{all}	α_1	α_2	δ	β_1^N
NLGL - LADRC	5 mm	0.5	$\boldsymbol{I}$	0.076 s	30 mm	1.32	5 mm	5.5 m/s	1 m/s	-	-	-	-
NLGL - NADRC	5 mm	0.7	$\boldsymbol{I}$	0.11 s	30 mm	-	5 mm	5.5 m/s	1 m/s	0.7	0.45	0.56	1.74

The experiments were considered completed when the distance between the target and the plane that is orthogonal to the tip-fixed axis $\boldsymbol{T}$ became 0. The following subsections explain the setup and the experiments, which are summarised in Table 6.5.

6.5.1 Setup

In the experiments, a clinically-sized (2.5 mm in diameter), medical-grade 4-segment PBN instrumented with 4 MCFs was used. The FBGs used in this work had a 12 mm lead-out length, and the complete setup is given in Chapter 3.

Table 6.5: The specifications of triplex experiment groups

	Controller	Initial Perturbation	Tissue Type	Exp. Type
Exp. 1-2-3	NLGL & NADRC	x: 1.5 mm y: 1.5 mm	Phantom	Path Following
Exp. 4-5-6	NLGL & LADRC	x: 1.5 mm y: 1.5 mm	Phantom	Path Following
Exp. 7-8-9	NLGL & NADRC	-	Phantom	Path Following
Exp. 10-11-12	NLGL & LADRC	-	Phantom	Path Following
Exp. 13-14-15	NLGL & NADRC	-	*Ex vivo*	Path Following
Exp. 16-17-18	NLGL & LADRC	-	*Ex vivo*	Path Following
Exp. 19-20-21	NLGL & NADRC	-	Phantom	Target Hitting
Exp. 22-23-24	NLGL & LADRC	-	Phantom	Target Hitting

The software for actuation, and path following were developed in-house using MATLAB 2019b (MathWorks Inc). The experiments were conducted with a sampling frequency of 50 Hz. The overall experimental setup is shown in figure 6.7 on the next page.

After each experiment, the PBN was removed and placed at a different entry point to prevent a new experiment from being effected by a previous experiment's track.

In order to make the tasks more complex, the initial pose in target-hitting experiments and the bending angles of the reference path in path-following experiments were not aligned with any of the 8 principal directions of the PBN (figure 6.9 on page 149) in which steering can be achieved relatively simply by one or two segments moving forward of the others [12].

Since the only source of information about the needle tip pose is from the FBG-based sensing, it is assumed here to be the true measurement. Therefore, in the experiments, the desired paths

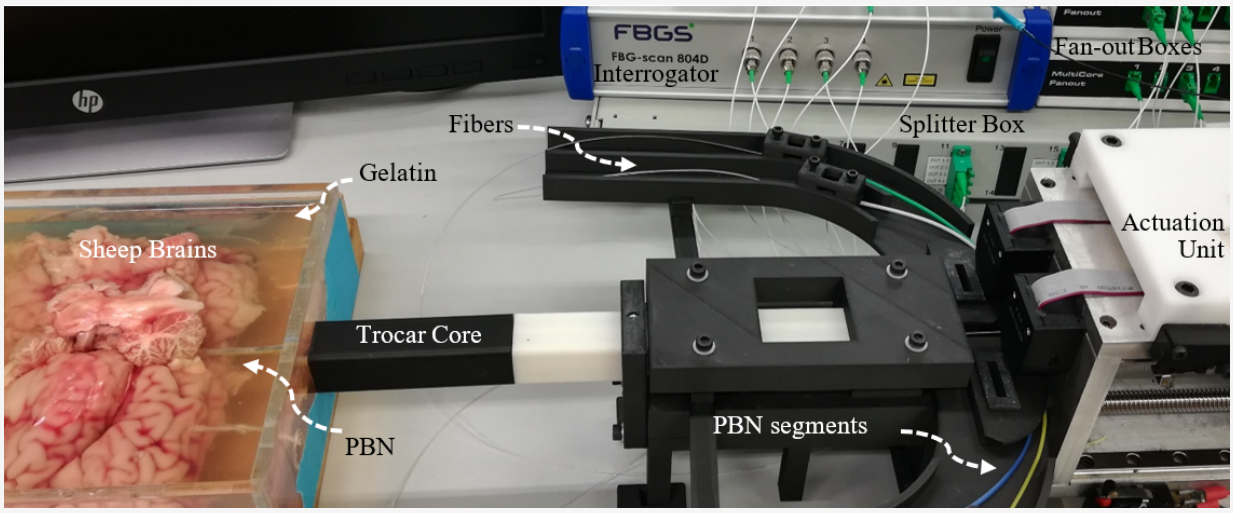

Figure 6.7: The overall *ex vivo* test setup used for path-following control experiments

and the target paths are fixed in space as opposed to being relative to the tissue.

6.5.2 Path-following Experiments

In the path-following experiments, the same 3D path used in the simulations was used as the reference path, and the experiment scenarios are illustrated in figure 6.8 on the next page. In 12 of the path-following experiments, the PBN was pushed along, and tangent to the path whereas it was off-path in the others, to assess the performance of the controller for a range of operating conditions. In all the experiments, the PBN was inserted to a depth of 120 mm, longer than the MCF length possessing the FBGs, which is 103 mm.

6.5.3 Target-hitting experiments

The virtual target started to move from a point that is 110 mm away from the PBN's starting point, in an arbitrary direction and by an amount equal to one fifth of the PBN tip's movement in the z axis at each step. It was assumed that there is no obstacle in the tissue. Also, since there is no path to follow, the location of the target was assigned to the NLGL's pseudo-target point, $\boldsymbol{p}_{s,t}$, at each time step. When the experiments started, the initial orientation of the PBN was set to be towards the target, and the targets were moved in the x-y plane. The initial orientation of the tip frame with respect to the world frame is shown in figure 6.9.

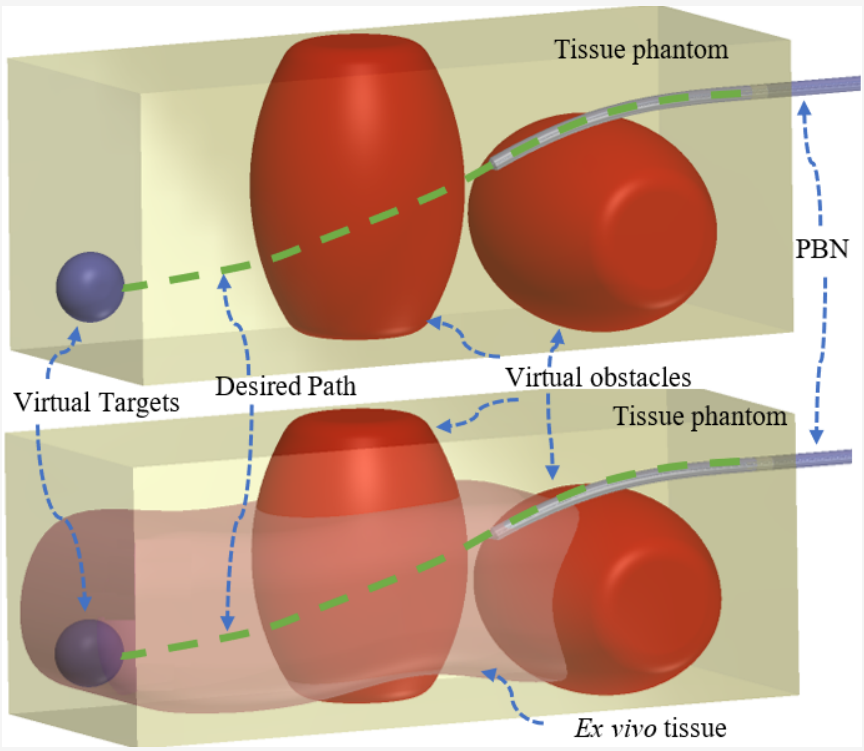

Figure 6.8: Path-Following Experiments : *In vitro* (top) and *ex vivo* (bottom) - The virtual obstacles are included in this figure for illustration purposes, and they are not used in this study

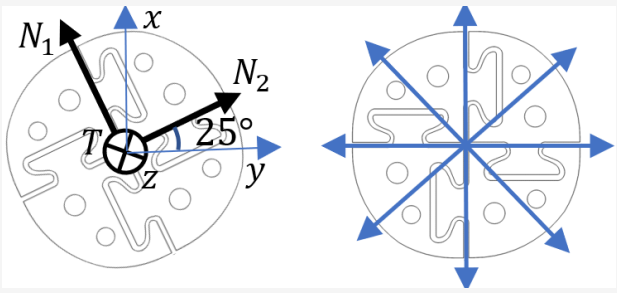

Figure 6.9: Left: The initial orientation of the tip frame with respect to the world reference frame used in the target-hitting experiments. Right: 8 principal steering directions of PBNs.

6.6 Results and Discussion

The insertion paths and target motions from the six target-hitting experiments are presented in figure 6.10 on the following page, showing that the control algorithm guided the needle effectively towards the moving targets. The absolute position errors during the path-following experiments are shown in figure 6.11 on page 152. It is seen that the controller manages to overcome the disturbances, including the ones caused by the transition from gelatine to tissue (at around 30 mm insertion length, for experiments 13 and 16). However, the maximum errors were obtained in *ex vivo* trials, as expected, because of the varying mechanical properties of the heterogeneous tissue.

For illustration purposes, the individual segment movements during experiment 9 and 11, obtained from the encoders of the actuation unit, are shown in figure 6.12 on page 152 and figure 6.13 on page 152. These figures illustrate that the LLC effectively manipulated the individual segments to track the curvature commands from the HLC. As shown, from time to time the difference between the minimum and maximum encoder values can reach 30 mm (the maximum allowable relative offset between segment tips), pushing the system to its limits.

The desired curvatures generated by the HLC, alongside the estimated curvatures, are shown in figure 6.14 on page 153 and figure 6.15 on page 153. It is apparent that the tracking is achieved with a lag, which is mainly due to the lead-out length. Thus it is expected that better results could be obtained with a shorter lead-out length.

The reference and measured trajectories are shown in figure 6.16 on page 153 and figure 6.17 on page 154, which show that the control law is able to track the reference path.

Lastly, the experimental results are summarised in Table 6.6. The results of target-hitting experiments (Exp 19-24) were calculated with the last PBN tip position data. Without considering the error of the shape sensing method used in this study, the mean tracking error for sheep brain is 2.87 mm in the case where 4 MCFs and 8 FBG sets were used. Although there is no consensus on accuracy requirement in the literature, an error below 3 mm is considered

acceptable for tumour volume larger than 0.5 ml [108]. Also, the results are comparable with the results obtained in [105], where planar curvature tracking of PBNs was validated experimentally and 3.3 ±1.42 mm mean targeting position error was obtained with an adaptive controller. However, the error results in this study are above the average targeting error of 1.33 mm given in [94], which reviews 8 fully-autonomous 3D path-following studies without a PBN and an optical fibre-based localisation. The main reasons for this discrepancy include: (i) tendon driven effect, which resulted in a disturbance on the tip curvature of the PBN; (ii) the lag caused by the lead-out length; (iii) the residual error resulting from the limited response speed of the ADRC to varying disturbances. In particular, the tendon driven effect is due to the friction between fibres and the PBN lumens.

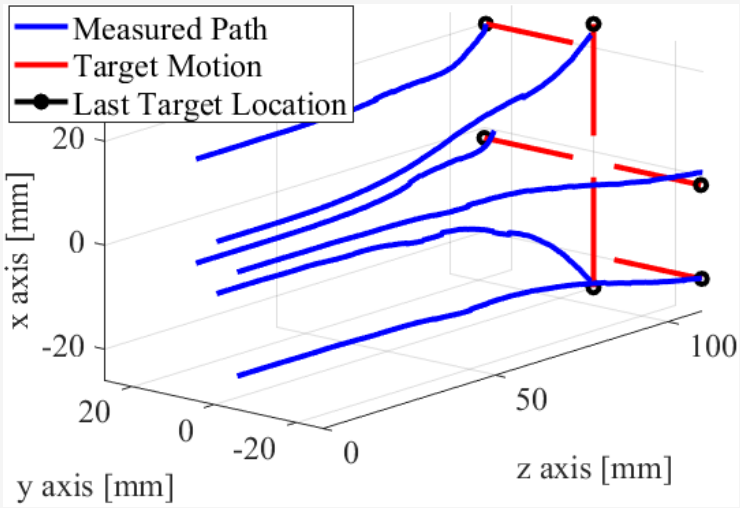

Figure 6.10: The insertion paths and target motions from the 6 target-hitting experiments.

When compared to the simulation studies in [103] and [104], which are the only 3D PBN path-following studies in the literature, one of the key differences in this work is the timing of the PBN tip programming. In [103] and [104], the PBN tip is proposed to be programmed while the overall PBN advancement continues moving. In ours, the PBN advances after the completion of the offset programming process at each step. It is postulated that the approach in these studies might result in significant overshoot in the case of bending angle discontinuities because of the PBN moving forward before the offsets are suitably programmed. Conversely, it was showed that the algorithm presented in this thesis can follow a path with a significant bending angle

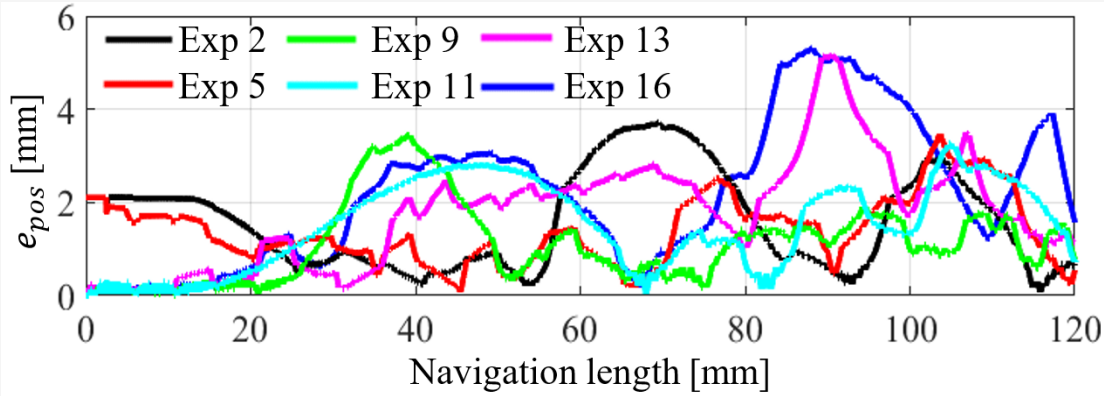

Figure 6.11: The absolute position error results of one of the experiments from each triplex experiment group. The selected experiments are the ones for which the mean error is closest to that of their experiment group.

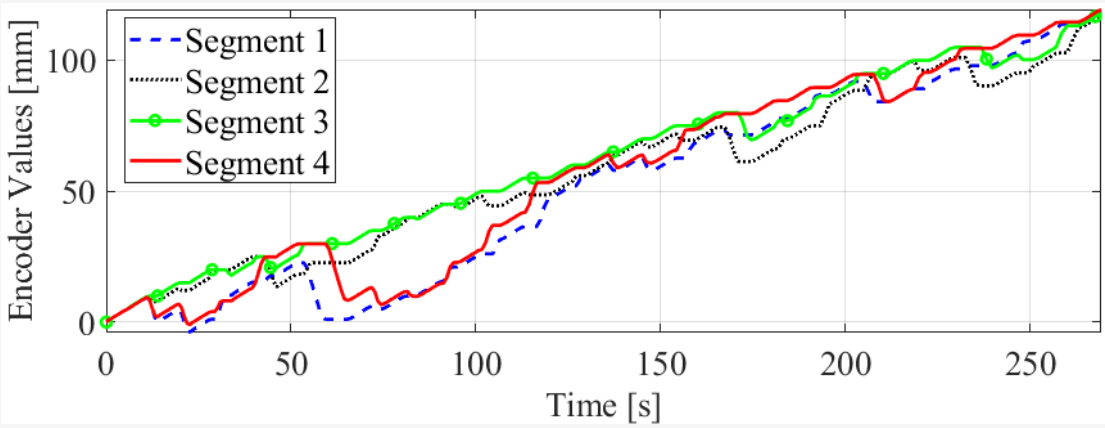

Figure 6.12: Movements of individual segments during experiment 9.

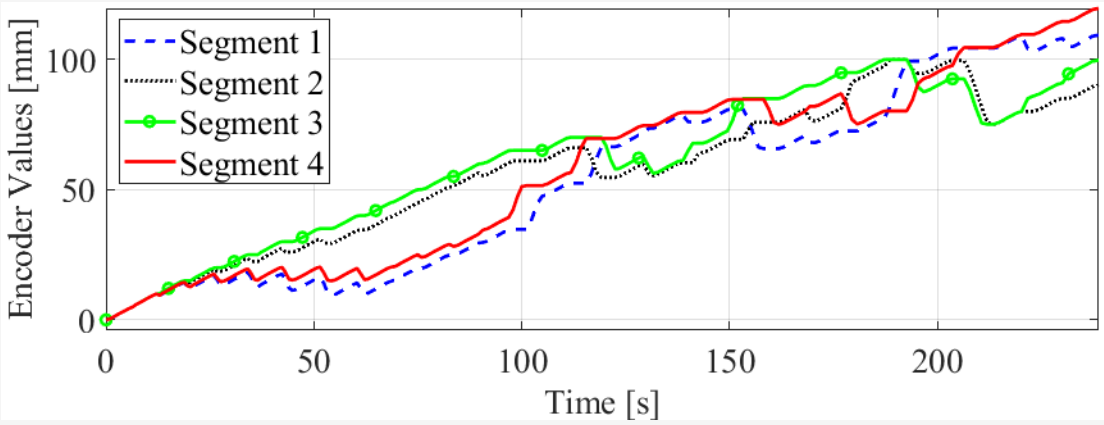

Figure 6.13: Movements of individual segments during experiment 11.

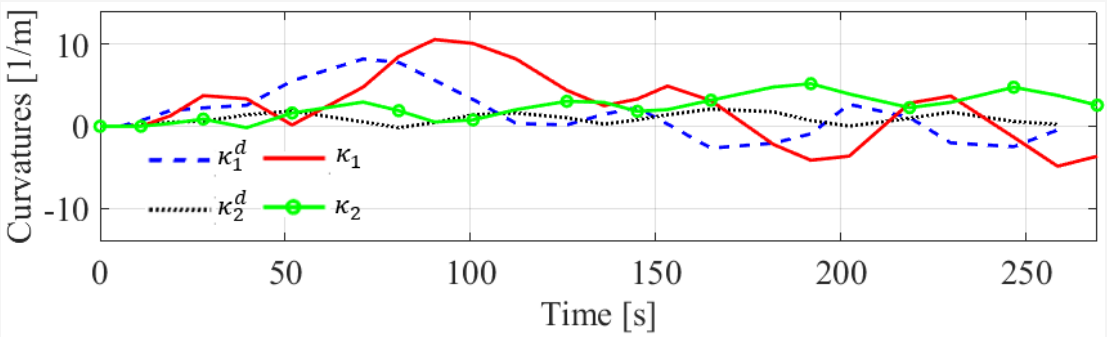

Figure 6.14: Desired curvature pair (the output of the HLC) and estimated curvature pair for experiment 9.

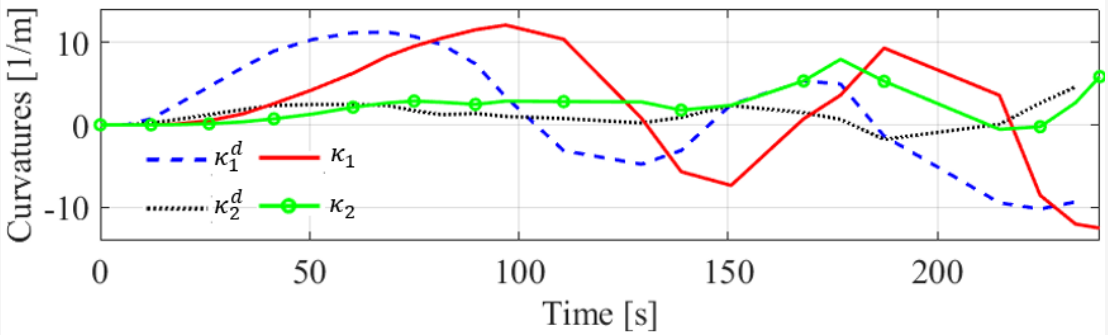

Figure 6.15: Desired curvature pair (the output of the HLC) and estimated curvature pair for experiment 11.

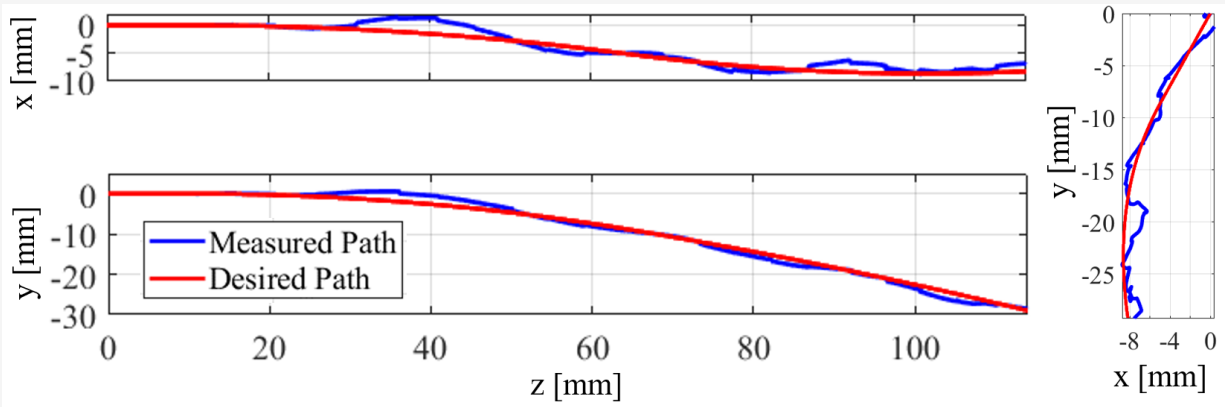

Figure 6.16: The reference path and the reconstructed path for experiment 9.

discontinuity (90°). In addition to this, the algorithm proposed for the PBN tip programming ensured the PBN's permissibility conditions to be observed at all times, thus resulting in the PBN acting as a single body.

In the experiments, unexpected lateral movements (up to 1 mm) of the PBN tip during PBN

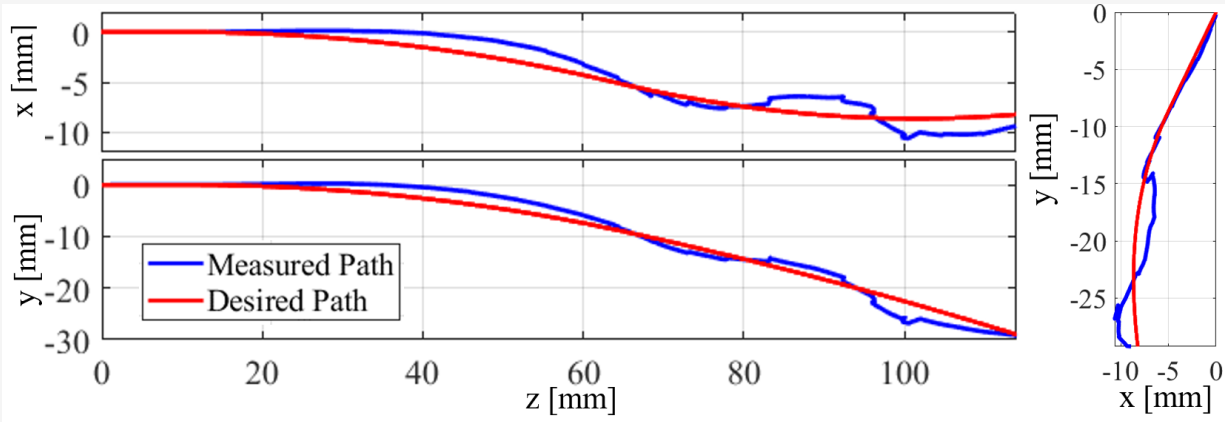

Figure 6.17: The reference path and the reconstructed path for experiment 11.

Table 6.6: Path-following Control Experimental Results - Absolute position error [mm], e_{pos}, over 120 mm insertion length of each triplex experiment group: Mean: $\bar{e}_{pos}$, Standard Deviation: $\sigma_{e_{pos}}$, Maximum: $e_{pos,max}$, Mean target error : $\bar{e}_{pos,target}$.

	Controller	Initial Perturbation	Tissue Type	Exp. Type	$\bar{e}_{pos}$	$\sigma_{e_{pos}}$	$e_{pos,max}$	$\bar{e}_{pos,target}$
Exp 1-2-3	NLGL & NADRC	x: 1.5 mm y: 1.5 mm	Phantom	Path Following	1.79	1.02	4.25	1.93
Exp 4-5-6	NLGL & LADRC	x: 1.5 mm y: 1.5 mm	Phantom	Path Following	1.6	0.72	3.87	2.49
Exp 7-8-9	NLGL & NADRC	-	Phantom	Path Following	1.32	0.85	3.96	1.75
Exp 10-11-12	NLGL & LADRC	-	Phantom	Path Following	1.70	0.93	3.61	2.62
Exp 13-14-15	NLGL & NADRC	-	*Ex vivo*	Path Following	1.98	1.15	5.28	2.83
Exp 16-17-18	NLGL & LADRC	-	*Ex vivo*	Path Following	2.37	1.54	5.84	2.91
Exp 19-20-21	NLGL & NADRC	-	Phantom	Target Hitting	-	-	6.56	3.12
Exp 22-23-24	NLGL & LADRC	-	Phantom	Target Hitting	-	-	5.28	2.5

tip programming were detected. When a non-LS advances, while its tip approaches the tip of the LS, it pushes the LS laterally to create space in the tissue for itself. Conversely, when a segment is retracted away from the LS, the latter bounces back to the centre of the channel that

was previously created by the segments at the PBN tip. This behaviour arises as a combination of these two reasons: (i) the non-zero friction between segments, (ii) the flexibility of the tissue and the needle. In fact, this effect could be beneficial in practice since it inherently results in an angular movement of the heading direction towards the reference path. In order to account for this effect, which was not taken into consideration during simulations, the value of the controller gain, k_p, was decreased manually for the experiments. In addition, another unexpected behaviour was seen during the *ex vivo* trials: when penetrating into different tissue layers, sometimes, the PBN partially buckled before the penetration, which caused transient disturbances in the tip curvature.

Similar to the simulation results, no considerable difference between LADRC and NADRC was detected in the experiments. In summary, LADRC is preferable in this case due to its simpler implementation.

6.7 Conclusion

In this work, path-following control methods for steerable needles using FBG-inscribed MCFs were investigated. It was shown that the steerable needle localisation needed for autonomous insertions can be achieved with MCFs via experimental validation of the path-following controller. To the best of the author's knowledge, this is the first steerable-needle path-following study utilising MCFs with FBGs. It was also shown that the reference path can be followed at an insertion length longer than the needle length possessing FBGs without the need for extrapolation thanks to the novel FBG-based shape reconstruction method presented in Chapter 5.

The NLGL has been used for guidance along the desired path since it guarantees a smooth convergence in line-of-sight path following. At the lower level, because of the high unpredictability of tissue-needle interactions, an ADRC-based control method was proposed because of its extreme tolerance to uncertainties, and robustness against external disturbances. With the elimination of the total disturbance, the MIMO plant was reduced to a single integration system, and only a simple linear proportional controller was used. Also, it was shown experimentally, for the first time, that PBNs are suitable for autonomous 3D path-following applications. In addition, an algorithm for PBN tip programming by observing PBN permissibility conditions was proposed. Lastly, the methods were experimentally tested both with a phantom tissue and an *ex vivo* brain tissue, and 1.79 mm mean and 6.56 mm maximum absolute position errors were obtained.

Chapter 7

Conclusion and Future Work

7.1 Main Conclusions and Summary of the Thesis Achievements

This thesis tackled the problem of three dimensional (3D) motion control of Programmable Bevel Tip Steerable Needles (PBNs) instrumented with proprioceptive sensors. Two novel methods for the pose estimation of PBNs, employing either four 5-Degree of Freedom (DoF) Electromagnetic (EM) sensors or optical fibres with Fibre Bragg Gratings (FBGs), were presented, along with experimental results demonstrating clinically acceptable tracking accuracy. The thesis objectives were laid out in Chapter 1.2. The Objective 1 was addressed in Chapter 4, in which the EM-based tip pose reconstruction method was presented, and in Chapter 5, in which the Objective 2 was also addressed, and the FBG-based method to reconstruct the tip pose as well as the entire needle shape was given.

Obtaining not only the position but the full pose is of vital importance for the PBN to be able to steer to a desired direction, as the PBN tip is programmed according to the desired steering direction and the current pose. Given that the smallest EM sensor on the market is just as large as the lumen diameter of the PBN segments but is only 5-DoF, the reconstruction method presented in Chapter 4 addressed the gap of reliable 6-DoF pose feedback of PBNs with EM sensors. The PBN tip was estimated as the midpoint between the Leading Segment (LS) tip and the Diagonal Segment (DS) tip's projection at the PBN tip. On the other hand, the rotational coordinates were determined by creating the basis axes of the PBN tip frame using the weighted segment couples to increase the contribution of the LS.

The proposed FBG-based shape sensing algorithm, which was developed based on the follow-the-leader assumption, allowed needle-shape reconstruction, even in the presence of only one FBG set. Other FBG sets were also integrated via the presented Kalman Filter (KF)-based fusion method, which enabled updating the needle's shape when a curvature change was detected along the needle. This approach removed the limit in which the reconstruction could only be made for the region covered with FBG sets. The FBG theory was also outlined, and the shape reconstruction methods from the literature were summarised with an emphasis on their dependency on interpolation methods, the need for which was eliminated by the proposed method. In addition, the effect of inflection points with respect to the FBG set locations were discussed with a simulation study.

Both of the reconstruction approaches dynamically fused the sensory information obtained from the proprioceptive sensors located at each of the PBN segments, which led to higher accuracy when compared to the case in which only one sensor was used to localise the needle. These methods are the first in this regard, *i.e.* they fuse the sensory information from each of the PBN segments. These methods do not require line of sight and are capable of reconstructing the full pose of the PBN tip regardless of the PBN tip configuration, i.e. the offset configuration of PBN segments. In the case of EM-based reconstruction, the tip pose of the PBN was calculated using the tip pose information of the individual segments, whereas in the case of FBG-based reconstruction, the curvature vectors along the entire path created by the PBN tip were needed for the same calculation. This requirement in FBG-based shape reconstruction methods results in reconstruction drift due to error accumulation, which does not occur in EM-based sensing. However, it has its own drawbacks, such as decreased accuracy occurring away from the centre of the EM field and not being Magnetic resonance imaging (MRI) compatible. The validation tests of the FBG-based reconstruction method were conducted *in vitro* and *ex vivo* to see the effect of tissue movements on the reconstruction performance, as the curvature changes were detected and considered by the KF-based fusion. However, the EM-based reconstruction method was only validated with 3D printed guides due to the absence of concerns such as the ones with FBG-based reconstruction. Both of these approaches were able to deal with the discrepancy

between the distal and proximal segment offsets caused by the curvilinear navigation of the PBN. While the zero-torsion assumption was made for the entire PBN in the FBG-based shape reconstruction method, the same assumption was only made for the tip of the needle in the EM-based method. The reason why it was not necessary to make such an assumption for the rest of the needle in the EM-based algorithm was that the tip pose reconstruction did not depend on the shape of the section without sensors. The torsion assumptions made in both of the reconstruction methods were considered acceptable based on [124].

The tracking and shape sensing algorithms presented in this thesis are of vital importance for closed-loop path-following controllers. To this end, the automated path-following control methods of PBNs instrumented with optical fibres were also investigated, and a novel path-following controller was given in Chapter 6. The Objectives 3 and 4, which were the main objectives of this thesis, were addressed in this chapter. The performance of the developed full 3D PBN motion controller, which was based on a combination of Nonlinear Guidance Law (NLGL) and Active Disturbance Rejection Control (ADRC), was validated first through simulations, with which the controller parameters were also tuned. Then, two types of experiments, namely target hitting and path following, were conducted with zero and non-zero initial perturbations. Finally, a discussion including a comparison with results from the literature was given. This thesis is the first experimental study to include the automated 3D path-following of PBNs. Moreover, it is the first study investigating path-following controllers for steerable needles with FBGs in Multi-core Fibres (MCFs). A novel method for PBN tip programming was also proposed in this study, and the methods were tested with both *in vitro* and *ex vivo* experiments.

7.2 Limitations

The primary limitations and discussions about the presented methods are laid out as follows:

EM Pose Estimation for PBNs

A EM sensors are not always suitable to be used in clinical settings due to the uniformity of the EM field being subjected to ferromagnetic objects. However, the algorithm is not dependent on the EM sensors, and other sensing modalities mentioned in Chapter 2.3 that provide the same DoF information could be preferred.

B The proposed algorithm was tested only *in vitro*, and it needs to be tested in more realistic environments, such as *ex vivo* and *in vivo* tissues, to better evaluate the performance.

C This algorithm assumes a constant bending angle between DS tip and LS tip. Although this assumption does not limit the variety of curves achievable by the PBN, it is an additional factor needed to be taken into account for the PBN's tip programming during navigation.

KF-Based, Dynamic 3D Shape Reconstruction for Steerable Needles with FBGs in MCFs

A To minimise the tendon driven effect, the fibres, which were not located on the neutral axes of the segments, were fixed to the segments from only segment bases. Such a fixation might not have been sufficient to prevent relative motion between segments and fibres under strain, and thus, it could have degraded the reconstruction accuracy. This could have been prevented by fixing the fibres to the neutral axes of the segments through the entire length. However, they should also be able to be removed easily for repeated use.

B The torsion that the PBN was exposed to could not be detected, and therefore, was not taken into account. It is expected that better results could be obtained by accounting for the torsion, which can be estimated using an appropriate fibre configuration, such as helically-wrapped fibres.

C The algorithm needs to be tested *in vivo* to see its performance in the presence of heartbeat and respiration, which could cause additional tissue movements and target migration. Additionally, the methods presented in this study should be accompanied with suitable means to detect the target migration and update the path accordingly.

D Because of its low stiffness, the brain tissue used for the experiments might not have sufficiently restricted the lateral movements of the PBN. There is an expectation that there will be better results if less compliant tissue is used, such as liver tissue, as this would allow the needle to have better support in follow-the-leader-type navigation, as a result of the fact that liver tissue has greater stiffness.

E The fibres used in this study were inscribed with the Draw Tower Gratings (DTG) method, which resulted in relatively low refractivity. Better results could be obtained using fibres produced by means of a method ensuring better refractivity.

3D Path-Following Control for Steerable Needles with FBGs in MCFs

A The lead-out length at the fibre tips lagged the feedback and increased the reaction time of the controller. The performance could be improved using fibres with shorter lead-out lengths

B The tendon-driven effect caused by the MCFs placed away from the neutral axes of the segments is thought to have resulted in a disturbance on the PBN navigation and could be prevented by fixing the fibres through the neutral axes of the segments.

C The residual error that resulted from the limited response speed of the ADRC was another limitation. It is often the case that employing an observer leaves a residual error,

since disturbance compensation is not instantaneous even when it is exact. However, in this thesis, the compensation was considered complete under the assumption of slow-varying disturbances. This was considered as an acceptable assumption, as the tissue was not expected to move abruptly with respect to the needle.

7.3 Future Work

By fusing the proposed FBG-based shape reconstruction method with the conventional methods requiring interpolation, the drawbacks of both approaches could be eliminated. This combination would be effective in cases of relatively fast tissue movements. Moreover, the developed algorithms should be tested *in vivo* for more convincing validation. For better estimation of the PBN shape, the information about the torsion that the needle is exposed to would be beneficial.

To have a completely automated system, a path planning algorithm should also be combined with the methods given in this thesis. In order to detect target migration due to tissue movements to update the path accordingly, the target could be observed via medical imaging methods, such as Ultrasound (US)-based methods. Additionally, the developed path-following controller's performance could be improved by updating the controller parameters adaptively according to tissue mechanical properties, such as stiffness, which could be estimated online via axial force measurement using MCFs. The axial force measurement could also be used for both an emergency stop, by detecting the obstacles, such as vessels, in front of the needle, and detecting the target tissue layer to increase targeting accuracy.

It would be beneficial to re-conduct the experiments using fibres with shorter lead-out lengths and with a PBN of which the fibres are fixed along the neutral axes of the segments, which would eliminate the tendon-driven effect and fibre-segment relative movements.

Furthermore, control methods ensuring a constant PBN tip speed should be investigated for smoother navigation. The effect of sample rate and insertion speed on the performance of the FBG-based shape sensing algorithm could also be investigated to select their optimal values.

Especially for PBNs, the curvature vectors along individual segments are of particular importance in terms of fault detection in the case of segment separation, which is the case in which the interlocking mechanism fails, and the segments come apart [37]. Detection of such a failure

is key to the future medical certification of a product based on this technology and could be possible with FBG sets that cover the entire PBN length.

References

[1] Abayazid, M., Kemp, M., and Misra, S. "3D flexible needle steering in soft-tissue phantoms using Fiber Bragg Grating sensors". In: *Proceedings - IEEE International Conference on Robotics and Automation* (2013), pp. 5843–5849. ISSN: 10504729. DOI: 10.1109/ICRA.2013.6631418.

[2] Abayazid, M., Moreira, P., Shahriari, N., Patil, S., Alterovitz, R., and Misra, S. "Ultrasound-guided three-dimensional needle steering in biological tissue with curved surfaces". In: *Medical Engineering and Physics* 37.1 (2015), pp. 145–150. ISSN: 18734030. DOI: 10.1016/j.medengphy.2014.10.005.

[3] Abolhassani, N., Patel, R., and Moallem, M. "Needle insertion into soft tissue: A survey". In: *Medical Engineering and Physics* 29.4 (2007), pp. 413–431. ISSN: 13504533. DOI: 10.1016/j.medengphy.2006.07.003.

[4] Askins, C. G., Miller, G. A., and Friebele, E. J. "Bend and twist sensing in a multi-core optical fiber". In: *Conference Proceedings - Lasers and Electro-Optics Society Annual Meeting-LEOS*. 2008, pp. 109–110. ISBN: 9781424419326. DOI: 10.1109/LEOS.2008.4688512.

[5] Assa, A. and Janabi-Sharifi, F. "A Kalman filter-based framework for enhanced sensor fusion". In: *IEEE Sensors Journal* 15.6 (2015), pp. 3281–3292. ISSN: 1530437X. DOI: 10.1109/JSEN.2014.2388153.

[6] Bak, J. B., Landas, S. K., and Haas, G. P. "Characterization of Prostate Cancer Missed by Sextant Biopsy". In: *Clinical Prostate Cancer* 2.2 (2003), pp. 115–118. ISSN: 15400352. DOI: 10.3816/CGC.2003.n.019.

[7] Bernardes, M. C., Adorno, B. V., Poignet, P., and Borges, G. A. "Robot-assisted automatic insertion of steerable needles with closed-loop imaging feedback and intraoperative

trajectory replanning". In: *Mechatronics* 23.6 (2013), pp. 630–645. ISSN: 09574158. DOI: 10.1016/j.mechatronics.2013.06.004.

[8] Bishop, R. L. "There is More than One Way to Frame a Curve". In: *The American Mathematical Monthly* (1975). ISSN: 00029890. DOI: 10.2307/2319846.

[9] Bui, V. K., Park, S., Park, J. O., and Ko, S. Y. "A novel curvature-controllable steerable needle for percutaneous intervention". In: *Proceedings of the Institution of Mechanical Engineers, Part H: Journal of Engineering in Medicine* 230.8 (2016), pp. 727–738. ISSN: 20413033. DOI: 10.1177/0954411916648988.

[10] Burdette, E. C., Rucker, D. C., Prakash, P., Diederich, C. J., Croom, J. M., Clarke, C., Stolka, P., Juang, T., Boctor, E. M., and Webster III, R. J. "The ACUSITT ultrasonic ablator: the first steerable needle with an integrated interventional tool". In: *Medical Imaging 2010: Ultrasonic Imaging, Tomography, and Therapy*. March 2010. San Diego, California, 2010. ISBN: 9780819480309. DOI: 10.1117/12.845972.

[11] Burgner-Kahrs, J., Rucker, D. C., and Choset, H. "Continuum Robots for Medical Applications: A Survey". In: *IEEE Transactions on Robotics* 31.6 (2015), pp. 1261–1280. ISSN: 15523098. DOI: 10.1109/TRO.2015.2489500.

[12] Burrows, C., Secoli, R., and Rodriguez Y Baena, F. "Experimental characterisation of a biologically inspired 3D steering needle". In: *International Conference on Control, Automation and Systems*. Gwangju, Korea, 2013, pp. 1252–1257. ISBN: 9788993215052. DOI: 10.1109/ICCAS.2013.6704141.

[13] Byrd, R. H., Gilbert, J. C., and Nocedal, J. "A trust region method based on interior point techniques for nonlinear programming". In: *Mathematical Programming, Series B* 89.1 (2000), pp. 149–185. ISSN: 00255610. DOI: 10.1007/PL00011391.

[14] Byrd, R. H., Hribar, M. E., and Nocedal, J. "An interior point algorithm for large-scale nonlinear programming". In: *SIAM Journal on Optimization* 9.4 (1999), pp. 877–900. ISSN: 10526234. DOI: 10.1137/S1052623497325107.

[15] Cerkvenik, U., Van De Straat, B., Gussekloo, S. W., and Van Leeuwen, J. L. "Mechanisms of ovipositor insertion and steering of a parasitic wasp". In: *Proceedings of the*

National Academy of Sciences of the United States of America. Vol. 114. 37. 2017, E7822–E7831. DOI: 10.1073/pnas.1706162114.

[16] Chitalia, Y., Deaton, N. J., Jeong, S., Rahman, N., and Desai, J. P. "Towards FBG-Based Shape Sensing for Micro-Scale and Meso-Scale Continuum Robots with Large Deflection". In: *IEEE Robotics and Automation Letters* 5.2 (2020), pp. 1712–1719. ISSN: 23773766. DOI: 10.1109/LRA.2020.2969934.

[17] Chugh, S. S., Chan, R. C., Johnson, S. B., and Packer, D. L. "Catheter tip orientation affects radiofrequency ablation lesion size in the canine left ventricle". In: *PACE - Pacing and Clinical Electrophysiology* 22.3 (1999), pp. 413–420. ISSN: 01478389. DOI: 10.1111/j.1540-8159.1999.tb00469.x.

[18] Cui, J., Zhao, S., Yang, C., and Tan, J. "Parallel transport frame for fiber shape sensing". In: *IEEE Photonics Journal* 10.1 (2018), pp. 1–12. ISSN: 19430655. DOI: 10.1109/JPHOT.2017.2782736.

[19] Cui, Z., Donder, A., and Rodriguez y Baena, F. "Nonlinear Trajectory Following Control for a Bio-Inspired Steerable Needle". In: *Submitted to IEEE International Conference on Robotics and Automation (ICRA) (Under Review)*.

[20] Denasi, A., Khan, F., Boskma, K. J., Kaya, M., Hennersperger, C., Gobl, R., Tirindelli, M., Navab, N., and Misra, S. "An Observer-Based Fusion Method Using Multicore Optical Shape Sensors and Ultrasound Images for Magnetically-Actuated Catheters". In: *IEEE International Conference on Robotics and Automation*. Brisbane, Australia, 2018, pp. 50–57. ISBN: 9781538630815. DOI: 10.1109/ICRA.2018.8462695.

[21] DiMaio, S. P. and Salcudean, S. E. "Needle steering and model-based trajectory planning". In: *International Conference on Medical Image Computing and Computer-Assisted Intervention*. Vol. 2878. 2003, pp. 33–40. DOI: 10.1007/978-3-540-39899-8{_}5.

[22] DiMaio, S. P., Samset, E., Fischer, G., Iordachita, I., Fichtinger, G., Jolesz, F., and Tempany, C. "Dynamic MRI Scan Plane Control for Passive Tracking of Instruments and Devices". In: *Medical Image Computing and Computer-Assisted Intervention - MICCAI*. 2007.

[23] Dimaio, S. P. and Salcudean, S. E. "Needle steering and motion planning in soft tissues". In: *IEEE Transactions on Biomedical Engineering* 52.6 (2005), pp. 965–974. ISSN: 00189294. DOI: 10.1109/TBME.2005.846734.

[24] Donder, A. and Konukseven, E. I. "Contour Tracking by Hybrid Force/Velocity Controlled Grinding: Comparison of Controllers ADRC -PID". In: *Proceedings of the World Congress on Engineering and Computer Science*. San Francisco, USA, 2017.

[25] Donder, A. and Rodriguez y Baena, F. "Kalman Filter-Based, Dynamic 3-D Shape Reconstruction for Steerable Needles with Fiber Bragg Gratings in Multi-Core Fibers". In: *Accepted to IEEE Transactions on Robotics* (2021).

[26] Donder, A. and Rodriguez y Baena, F. "3-D Path Following Control of Steerable Needles with Fiber Bragg Gratings in Multi-Core Fibers". In: *Submitted to IEEE Transactions on Robotics (Under Review)* ().

[27] Ee, W. W. G., Lau, W. L. J., Yeo, W., Von Bing, Y., and Yue, W. M. "Does minimally invasive surgery have a lower risk of surgical site infections compared with open spinal surgery?" In: *Clinical Orthopaedics and Related Research* 472.6 (2014), pp. 1718–1724. ISSN: 15281132. DOI: 10.1007/s11999-013-3158-5.

[28] Elmenreich, W. "An introduction to sensor fusion". In: *Austria: Vienna University Of Technology* February (2002), pp. 1–28. ISSN: 0952-813X.

[29] Favaro, A., Secoli, R., Baena, F. R. Y., and Momi, E. D. "Model-Based Robust Pose Estimation for a Multi-Segment, Programmable Bevel-Tip Steerable Needle". In: *IEEE Robotics and Automation Letters* 5.4 (2020), pp. 6780–6787. ISSN: 23773766. DOI: 10.1109/LRA.2020.3018406.

[30] *FBGS - DTG® Technique.*

[31] Fichtinger, G., DeWeese, T. L., Patriciu, A., Tanacs, A., Mazilu, D., Anderson, J. H., Masamune, K., Taylor, R. H., and Stoianovici, D. "System for robotically assisted prostate biopsy and therapy with intraoperative CT guidance". In: *Academic Radiology* 9.1 (2002), pp. 60–74. ISSN: 10766332. DOI: 10.1016/S1076-6332(03)80297-0.

[32] Fornage, B. D. "Sonographically guided needle biopsy of nonpalpable breast lesions". In: *Journal of Clinical Ultrasound* 27.7 (1999), pp. 385–398. ISSN: 00912751. DOI: 10.1002/(SICI)1097-0096(199909)27:7⟨385::AID-JCU5⟩3.0.CO;2-O.

[33] Franceschini, G. "The Mechanics of Human Brain Tissue". In: *Modelling, Preservation and Control of Materials and Structures. University of Trento, Trento, Italy* (2006).

[34] Franz, A. M., Haidegger, T., Birkfellner, W., Cleary, K., Peters, T. M., and Maier-Hein, L. "Electromagnetic tracking in medicine - A review of technology, validation, and applications". In: *IEEE Transactions on Medical Imaging* 33.8 (2014), pp. 1702–1725. ISSN: 1558254X. DOI: 10.1109/TMI.2014.2321777.

[35] Frasson, L., Ferroni, F., Ko, S. Y., Dogangil, G., and Rodriguez y Baena, F. "Experimental evaluation of a novel steerable probe with a programmable bevel tip inspired by nature". In: *Journal of Robotic Surgery* 6.3 (2012), pp. 189–197. ISSN: 18632483. DOI: 10.1007/s11701-011-0277-4.

[36] Frasson, L., Ko, S. Y., Turner, A., Parittotokkaporn, T., Vincent, J. F., and Rodriguez Y Baena, F. "STING: A soft-tissue intervention and neurosurgical guide to access deep brain lesions through curved trajectories". In: *Proceedings of the Institution of Mechanical Engineers, Part H: Journal of Engineering in Medicine* 224.6 (2009), pp. 775–788. ISSN: 09544119. DOI: 10.1243/09544119JEIM663.

[37] Frasson, L., Neubert, J., Reina, S., Oldfield, M., Davies, B. L., and Rodriguez y Baena, F. "Development and validation of a numerical model for cross-section optimization of a multi-part probe for soft tissue intervention". In: *32nd Annual International Conference of the IEEE Engineering in Medicine and Biology Society*. Buenos Aires, Argentina: IEEE, 2010, pp. 3202–3205. ISBN: 9781424441235. DOI: 10.1109/IEMBS.2010.5627409.

[38] Galloway, K. C., Chen, Y., Templeton, E., Rife, B., Godage, I. S., and Barth, E. J. "Fiber Optic Shape Sensing for Soft Robotics". In: *Soft Robotics* 6.5 (2019), pp. 671–684. ISSN: 21695180. DOI: 10.1089/soro.2018.0131.

[39] Gao, Z. "Scaling and bandwidth-parameterization based controller tuning". In: *Proceedings of the American Control Conference, 2006*. Vol. 6. 2006, pp. 4989–4996. ISBN: 0-7803-7896-2. DOI: 10.1109/ACC.2003.1242516.

[40] Gao, Z. "Active disturbance rejection control: A paradigm shift in feedback control system design". In: *Proceedings of the American Control Conference*. 2006, pp. 2399–2405. ISBN: 1424402107. DOI: 10.1109/ACC.2006.1656579.

[41] Ghani, K. R., Pilcher, J., Patel, U., Rowland, D., Nassiri, D., and Anson, K. "Three-dimensional ultrasound reconstruction of the pelvicaliceal system: An in-vitro study". In: *World Journal of Urology* 26.5 (2008), pp. 493–498. ISSN: 07244983. DOI: 10.1007/s00345-008-0276-x.

[42] Glozman, D. and Shoham, M. "Image-Guided Robotic Flexible Needle Steering". In: *IEEE Transactions on Robotics* 23.3 (2007), pp. 459–467.

[43] Han, J. "From PID to active disturbance rejection control". In: *IEEE Transactions on Industrial Electronics* 56.3 (2009), pp. 900–906. ISSN: 02780046. DOI: 10.1109/TIE.2008.2011621.

[44] Hanson, A. J. and Ma, H. "Quaternion Frame Approach to Streamline Visualization". In: *IEEE Transactions on Visualization and Computer Graphics* 1.2 (1995), pp. 164–174. ISSN: 10772626. DOI: 10.1109/2945.468403.

[45] Henken, K., Van Gerwen, D., Dankelman, J., and Van Den Dobbelsteen, J. "Accuracy of needle position measurements using fiber Bragg gratings". In: *Minimally Invasive Therapy and Allied Tech.* 21.6 (2012), pp. 408–414. ISSN: 13645706. DOI: 10.3109/13645706.2012.666251.

[46] Henken, K. R., Dankelman, J., Dobbelsteen, J. J. V. D., Cheng, L. K., and Heiden, M. S. V. D. "Error Analysis of FBG-Based Shape Sensors for Medical Needle Tracking". In: *IEEE/ASME Transactions on Mechatronics* 19.5 (2014), pp. 1523–1531. ISSN: 10834435. DOI: 10.1109/TMECH.2013.2287764.

[47] Hibbeler, R. C. *Mechanics of Materials*. 8th ed. Upper Saddle River, NJ, USA: Pearson Prentice Hall, 2011.

[48] Hill, K. O. and Meltz, G. "Fiber Bragg grating technology fundamentals and overview". In: *Journal of Lightwave Technology* 15.8 (1997), pp. 1263–1276. ISSN: 07338724. DOI: 10.1109/50.618320.

[49] Jäckle, S., Eixmann, T., Schulz-Hildebrandt, H., Hüttmann, G., and Pätz, T. "Fiber optical shape sensing of flexible instruments for endovascular navigation". In: *International Journal of Computer Assisted Radiology and Surgery* 14.12 (2019), pp. 2137–2145. ISSN: 18616429. DOI: 10.1007/s11548-019-02059-0.

[50] Jiang, B., Gao, W., Kacher, D., Nevo, E., Fetics, B., Lee, T. C., and Jayender, J. "Kalman filter-based EM-optical sensor fusion for needle deflection estimation". In: *International Journal of Computer Assisted Radiology and Surgery* 13.4 (2018), pp. 573–583. ISSN: 18616429. DOI: 10.1007/s11548-018-1708-8.

[51] Kaminer, I., Pascoal, A., Xargay, E., Hovakimyan, N., Cao, C., and Dobrokhodov, V. "Path Following for Unmanned Aerial Vehicles Using L1 Adaptive Augmentation of Commercial Autopilots". In: *Journal of Guidance, Control, and Dynamics* 33.2 (2010), pp. 550–564. ISSN: 0731-5090. DOI: 10.2514/1.42056.

[52] Kapitanyuk, Y. A., Proskurnikov, A. V., and Cao, M. "A Guiding Vector-Field Algorithm for Path-Following Control of Nonholonomic Mobile Robots". In: *IEEE Transactions on Control Systems Technology* 26.4 (2018), pp. 1372–1385. ISSN: 10636536. DOI: 10.1109/TCST.2017.2705059.

[53] Khan, F., Denasi, A., Barrera, D., Madrigal, J., Sales, S., and Misra, S. "Multi-core Optical Fibers with Bragg Gratings as Shape Sensor for Flexible Medical Instruments". In: *IEEE Sensors Journal* (2019). ISSN: 1530-437X. DOI: 10.1109/JSEN.2019.2905010.

[54] Khan, F., Donder, A., Galvan, S., Rodriguez y Baena, F., and Misra, S. "Pose Measurement of Flexible Medical Instruments using Fiber Bragg Gratings in Multi-Core Fiber". In: *IEEE Sensors J.* 20.18 (2020).

[55] Ko, S. Y., Davies, B. L., and Rodriguez y Baena, F. "Two-dimensional needle steering with a "programmable bevel" inspired by nature: Modeling preliminaries". In: *IEEE/RSJ International Conference on Intelligent Robots and Systems*. Taipei, Taiwan, 2010, pp. 2319–2324. ISBN: 9781424466757. DOI: 10.1109/IROS.2010.5650859.

[56] Ko, S. Y., Frasson, L., and Rodriguez y Baena, F. "Closed-loop planar motion control of a steerable probe with a "programmable bevel" inspired by nature". In: *IEEE Transactions on Robotics* 27.5 (2011), pp. 970–983. ISSN: 15523098. DOI: 10.1109/TRO.2011.2159411.

[57] Ko, S. Y. and Rodriguez y Baena, F. "Trajectory following for a flexible probe with state/input constraints: An approach based on model predictive control". In: *Robotics and Autonomous Systems* 60.4 (2012), pp. 509–521. ISSN: 09218890. DOI: 10.1016/j.robot.2011.11.011.

[58] Ko, S. Y. and Rodriguez y Baena, F. "Toward a miniaturized needle steering system with path planning for obstacle avoidance". In: *IEEE Transactions on Biomedical Eng* 60.4 (2013), pp. 910–917. ISSN: 00189294. DOI: 10.1109/TBME.2012.2227741.

[59] Langer, J. and Singer, D. A. "Lagrangian aspects of the Kirchhoff elastic rod". In: *SIAM Review* 38.4 (1996), pp. 605–618. ISSN: 00361445. DOI: 10.1137/S0036144593253290.

[60] Latifinavid, M., Donder, A., and Konukseven, E. i. "High-performance parallel hexapod-robotic light abrasive grinding using real-time tool deflection compensation and constant resultant force control". In: *International Journal of Advanced Manufacturing Technology* 96.9-12 (2018), pp. 3403–3416. ISSN: 14333015. DOI: 10.1007/s00170-018-1838-8.

[61] Leibinger, A., Oldfield, M. J., and Rodriguez y Baena, F. "Minimally disruptive needle insertion: a biologically inspired solution". In: *Interface Focus* 6.3 (2016), p. 20150107. ISSN: 2042-8898. DOI: 10.1098/rsfs.2015.0107.

[62] Li, J., Qi, X., Xia, Y., and Gao, Z. "On asymptotic stability for nonlinear ADRC based control system with application to the ball-beam problem". In: *Proceedings of the American Control Conference* 2016-July (2016), pp. 4725–4730. ISSN: 07431619. DOI: 10.1109/ACC.2016.7526100.

[63] Li, M., Li, G., Gonenc, B., Duan, X., and Iordachita, I. "Towards human-controlled, real-time shape sensing based flexible needle steering for MRI-guided percutaneous therapies". In: *The international journal of medical robotics and computer assisted surgery* 13 (2017). DOI: 10.1002/rcs.

[64] Li, P., Jiang, S., Liang, D., Yang, Z., Yu, Y., and Wang, W. "Modeling of path planning and needle steering with path tracking in anatomical soft tissues for minimally invasive surgery". In: *Medical Engineering and Physics* 41 (2017), pp. 35–45. ISSN: 18734030. DOI: 10.1016/j.medengphy.2017.01.006.

[65] Luca, A. D., Oriolo, G., and Samson, C. *Feedback Control of a Nonholonomic Car-like Robot*. 1998, pp. 172–253. ISBN: 3540762191. DOI: 10.1016/0094-114x(86)90035-2.

[66] Luenberger, D. G. "An Introduction to Observers". In: *IEEE Transactions on Automatic Control* 16.6 (1971), pp. 596–602. ISSN: 15582523. DOI: 10.1109/TAC.1971.1099826.

[67] Lundervold, A. S. and Lundervold, A. "An overview of deep learning in medical imaging focusing on MRI". In: *Journal of Medical Physics* 29.2 (2019), pp. 102–127. ISSN: 18764436. DOI: 10.1016/j.zemedi.2018.11.002.

[68] Majewicz, A., Siegel, J. J., Stanley, A. A., and Okamura, A. M. "Design and evaluation of duty-cycling steering algorithms for robotically-driven steerable needles". In: *Proceedings - IEEE International Conference on Robotics and Automation* (2014), pp. 5883–5888. ISSN: 10504729. DOI: 10.1109/ICRA.2014.6907725.

[69] Matheson, E., Secoli, R., Burrows, C., Leibinger, A., and Rodriguez y Baena, F. "Cyclic Motion Control for Programmable Bevel-Tip Needles to Reduce Tissue Deformation". In: *Journal of Medical Robotics Research* 04.01 (2013). ISSN: 2424-905X. DOI: 10.1142/s2424905x18420011.

[70] Matheson, E., Watts, T., Secoli, R., and Rodriguez y Baena, F. "Cyclic Motion Control for Programmable Bevel-Tip Needle 3D Steering: A Simulation Study". In: *IEEE Int Conference on Robotics and Biomimetics, ROBIO 2018*. Kuala Lumpur, Malaysia: IEEE, 2018, pp. 444–449. ISBN: 9781728103761. DOI: 10.1109/ROBIO.2018.8665117.

[71] Matheson, E., Secoli, R., Galvan, S., and Baena, F. R. Y. "Human-Robot Visual Interface for 3D Steering of a Flexible, Bioinspired Needle for Neurosurgery". In: *IEEE International Conference on Intelligent Robots and Systems*. 2019, pp. 5426–5431. ISBN: 9781728140049. DOI: 10.1109/IROS40897.2019.8967604.

[72] Misra, S., Reed, K. B., Douglas, A. S., Ramesh, K. T., and Okamura, A. M. "Needle-tissue interaction forces for bevel-tip steerable needles". In: *2nd Biennial IEEE/RAS-EMBS International Conference on Biomedical Robotics and Biomechatronics, BioRob 2008*. IEEE, 2008, pp. 224–231. ISBN: 9781424428830. DOI: 10.1109/BIOROB.2008.4762872.

[73] Monet, F., Sefati, S., Lorre, P., Poiffaut, A., Kadoury, S., Armand, M., Iordachita, I., and Kashyap, R. "High-Resolution Optical Fiber Shape Sensing of Continuum Robots: A Comparative Study ". In: *Proceedings - IEEE International Conference on Robotics and Automation*. 2020, pp. 8877–8883. ISBN: 9781728173955. DOI: 10.1109/ICRA40945.2020.9197454.

[74] Moon, H., Jeong, J., Kang, S., Kim, K., Song, Y. W., and Kim, J. "Fiber-Bragg-grating-based ultrathin shape sensors displaying single-channel sweeping for minimally invasive surgery". In: *Optics and Lasers in Engineering* 59 (2014), pp. 50–55. ISSN: 01438166. DOI: 10.1016/j.optlaseng.2014.03.005.

[75] Moore, J. P. and Rogge, M. D. "Shape sensing using multi-core fiber optic cable and parametric curve solutions". In: *Optics Express* 20.3 (2012), p. 2967. ISSN: 1094-4087. DOI: 10.1364/oe.20.002967.

[76] Okazawa, S., Ebrahimi, R., Chuang, J., Salcudean, S. E., and Rohling, R. "Hand-held steerable needle device". In: *IEEE/ASME Transactions on Mechatronics* 10.3 (2005), pp. 285–296. ISSN: 10834435. DOI: 10.1109/TMECH.2005.848300.

[77] Oldfield, M., Dini, D., Giordano, G., and Rodriguez y Baena, F. "Detailed finite element modelling of deep needle insertions into a soft tissue phantom using a cohesive approach". In: *Computer Methods in Biomechanics and Biomedical Engineering* 16.5 (2013), pp. 530–543. ISSN: 10255842. DOI: 10.1080/10255842.2011.628448.

[78] Oldfield, M. J., Leibinger, A., Seah, T. E. T., and Rodriguez y Baena, F. "Method to Reduce Target Motion Through Needle–Tissue Interactions". In: *Annals of Biomedical Engineering* 43.11 (2015), pp. 2794–2803. ISSN: 15739686. DOI: 10.1007/s10439-015-1329-0.

[79] Paloschi, D., Bronnikov, K. A., Korganbayev, S., Wolf, A. A., Dostovalov, A., and Saccomandi, P. "3D Shape Sensing with Multicore Optical Fibers: Transformation Matrices Versus Frenet-Serret Equations for Real-Time Application". In: *IEEE Sensors Journal* 21.4 (2021), pp. 4599–4609. ISSN: 15581748. DOI: 10.1109/JSEN.2020.3032480.

[80] Park, S., Deyst, J., and How, J. P. "Performance and lyapunov stability of a nonlinear path-following guidance method". In: *Journal of Guidance, Control, and Dynamics* 30.6 (2007), pp. 1718–1728. ISSN: 15333884. DOI: 10.2514/1.28957.

[81] Park, Y. L., Elayaperumal, S., Daniel, B., Ryu, S. C., Shin, M., Savall, J., Black, R. J., Moslehi, B., and Cutkosky, M. R. "Real-time estimation of 3-D needle shape and deflection for MRI-guided interventions". In: *IEEE/ASME Transactions on Mechatronics* 15.6 (2010), pp. 906–915. ISSN: 10834435. DOI: 10.1109/TMECH.2010.2080360.

[82] Patil, S., Van den, J., and Alterovitz, B. R. "Motion Planning Under Uncertainty In Highly Deformable Environments". In: *Robotics science and systems: online proceedings* (2011).

[83] Pauer, H., Ledermann, C., Tuschmann, W., and Woern, H. "Non-linear compensation of production inaccuracies and material drift by adjusting the sensor data fusion algorithms for shape sensing based on FBG-optical fibers". In: *Processing of 2014 International Conference on Multisensor Fusion and Information Integration for Intelligent Systems, MFI 2014*. IEEE, 2014, pp. 1–5. ISBN: 9781479967322. DOI: 10.1109/MFI.2014.6997688.

[84] Poddler, T. K., Clark, D. P., Sherman, J., Fuller, D., Messing, E. M., Rubens, D. J., Strang, J. G., Zhang, Y. D., O'Dell, W., Ng, W. S., et al. "Effects of Tip Geometry of Surgical Needles: An Assessment of Force and Deflection". In: *The 3rd European Medical and Biological Engineering Conference*. Prague, Czech Republic, 2005. ISBN: 9781627480758.

[85] Polygerinos, P., Zbyszewski, D., Schaeffter, T., Razavi, R., Seneviratne, L. D., and Althoefer, K. "MRI-compatible fiber-optic force sensors for catheterization procedures". In: *IEEE Sensors Journal* 10.10 (2010), pp. 1598–1608. ISSN: 1530437X. DOI: 10.1109/JSEN.2010.2043732.

[86] Prausnitz, M. R. and Langer, R. "Transdermal drug delivery". In: *Nature Biotechnology* 26.11 (2008), pp. 1261–1268. ISSN: 10870156. DOI: 10.1038/nbt.1504.

[87] Raton, B. *Modern Differential Geometry of Curves and Surfaces with Mathematica*. Florida, USA: Chapman & Hall/CRC, 2006.

[88] Reichl, T., Gardiazabal, J., and Navab, N. "Electromagnetic servoing - A new tracking paradigm". In: *IEEE Transactions on Medical Imaging* 32.8 (2013), pp. 1526–1535. ISSN: 02780062. DOI: 10.1109/TMI.2013.2259636.

[89] Ribeiro, T. T. and Conceição, A. G. "Nonlinear Model Predictive Visual Path Following Control to Autonomous Mobile Robots". In: *Journal of Intelligent and Robotic Systems: Theory and Applications* 95.2 (2019), pp. 731–743. ISSN: 15730409. DOI: 10.1007/s10846-018-0896-3.

[90] Robinson, R. D. "Reliable Machine Learning for Medical Imaging Data through Automated Quality Control and Data Harmonization". In: (July 2020).

[91] Roesthuis, R. J., Van De Berg, N. J., Van Den Dobbelsteen, J. J., and Misra, S. "Modeling and steering of a novel actuated-tip needle through a soft-tissue simulant using Fiber Bragg Grating sensors". In: *IEEE International Conference on Robotics and Automation, ICRA*. Vol. 2015-June. June. 2015, pp. 2283–2289. ISBN: 10504729. DOI: 10.1109/ICRA.2015.7139502.

[92] Roesthuis, R. J., Kemp, M., Van Den Dobbelsteen, J. J., and Misra, S. "Three-dimensional needle shape reconstruction using an array of fiber Bragg grating sensors". In: *IEEE/ASME Transactions on Mechatronics* 19.4 (2014), pp. 1115–1126. ISSN: 10834435. DOI: 10.1109/TMECH.2013.2269836.

[93] Rossa, C., Fong, J., Usmani, N., Sloboda, R., and Tavakoli, M. "Multiactuator Haptic Feedback on the Wrist for Needle Steering Guidance in Brachytherapy". In: *IEEE Robotics and Automation Letters* 1.2 (2016), pp. 852–859. ISSN: 23773766. DOI: 10.1109/LRA.2016.2528295.

[94] Rossa, C. and Tavakoli, M. "Issues in closed-loop needle steering". In: *Control Engineering Practice* 62.January (2017), pp. 55–69. ISSN: 09670661. DOI: 10.1016/j.conengprac.2017.03.004.

[95] Rossi, S., Buskarini, E., Garbagnati, F., Di Stasi, M., Quaretti, P., Rago, M., Zangrandi, A., Andreola, S., Silverman, D., and Buscarini, L. "Percutaneous Treatment of Small Hepatic Tumors by an Expandable RF Needle Electrode". In: *American Journal of Roentgenology* April (1998), pp. 1015–1022.

[96] Rubio, Y., Picos, K., Orozco-Rosas, U., Sepúlveda, C., Ballinas, E., Montiel, O., Castillo, O., and Sepúlveda, R. "Path following fuzzy system for a nonholonomic mobile robot based on frontal camera information". In: *Studies in Computational Intelligence* 749 (2018), pp. 223–240. ISSN: 1860949X. DOI: 10.1007/978-3-319-71008-2{_}18.

[97] Rucker, D. C., Das, J., Gilbert, H. B., Swaney, P. J., Miga, M. I., Sarkar, N., and Webster, R. J. "Sliding mode control of steerable needles". In: *IEEE Transactions on Robotics* 29.5 (2013), pp. 1289–1299. ISSN: 15523098. DOI: 10.1109/TRO.2013.2271098.

[98] Ryu, S. C. and Dupont, P. E. "FBG-based shape sensing tubes for continuum robots". In: *Proceedings - IEEE International Conference on Robotics and Automation*. Hong Kong, China, 2014, pp. 3531–3537. ISBN: 9781479936847. DOI: 10.1109/ICRA.2014.6907368.

[99] Sadjadi, H., Hashtrudi-Zaad, K., and Fichtinger, G. "Fusion of electromagnetic trackers to improve needle deflection estimation: Simulation study". In: *IEEE Transactions on Biomedical Engineering* 60.10 (2013), pp. 2706–2715. ISSN: 00189294. DOI: 10.1109/TBME.2013.2262658.

[100] Scali, M., Pusch, T. P., Breedveld, P., and Dodou, D. "Needle-like instruments for steering through solid organs: A review of the scientific and patent literature". In: *Proceedings of the Institution of Mechanical Engineers, Part H: Journal of Engineering in Medicine* 231.3 (2017), pp. 250–265. ISSN: 20413033. DOI: 10.1177/0954411916672149.

[101] Schwein, A., Kramer, B., Chinnadurai, P., Walker, S., O'Malley, M., Lumsden, A., and Bismuth, J. "Flexible robotics with electromagnetic tracking improves safety and efficiency during in vitro endovascular navigation". In: *Journal of Vascular Surgery* 65.2 (2017), pp. 530–537. ISSN: 10976809. DOI: 10.1016/j.jvs.2016.01.045.

[102] Sears, P. and Dupont, P. "A steerable needle technology using curved concentric tubes". In: *IEEE International Conference on Intelligent Robots and Systems*. Beijing, China, 2006, pp. 2850–2856. ISBN: 142440259X. DOI: 10.1109/IROS.2006.282072.

[103] Secoli, R. and Rodriguez y Baena, F. "Closed-loop 3D motion modeling and control of a steerable needle for soft tissue surgery". In: *IEEE International Conference on Robotics and Automation*. 3. Karlsruhe, Germany, 2013, pp. 5831–5836. ISBN: 9781467356411. DOI: 10.1109/ICRA.2013.6631416.

[104] Secoli, R. and Rodriguez y Baena, F. "Adaptive path-following control for bio-inspired steerable needles". In: *6th IEEE RAS/EMBS Int. Conf. on Biomedical Robotics and Biomechatronics*. UTown, Singapore, 2016. ISBN: 9781509032877. DOI: 10.1109/BIOROB.2016.7523603.

[105] Secoli, R. and Rodriguez y Baena, F. "Experimental Validation of Curvature Tracking with a Programmable Bevel-Tip Steerable Needle". In: *Inter. Symposium on Medical Robotics (ISMR)*. 2018. ISBN: 9781538625125.

[106] Secoli, R., Matheson, E., Pinzi, M., Galvan, S., Watts, T., Donder, A., and Rodriguez y Baena, F. "A Modular Robotic Platform for Precision Neurosurgery with a PBN". In: *Submitted to IEEE Transactions on Robotics (Under Review)* ().

[107] Sefati, S., Hegeman, R., Alambeigi, F., Iordachita, I., and Armand, M. "FBG-Based Position Estimation of Highly Deformable Continuum Manipulators: Model-Dependent vs. Data-Driven Approaches". In: *2019 International Symposium on Medical Robotics, ISMR 2019*. IEEE, 2019, pp. 1–6. ISBN: 9781538678251. DOI: 10.1109/ISMR.2019.8710179.

[108] Seifabadi, R., Cho, N. B. J., Song, S.-E., Tokuda, J., Hata, N., Tempany, C., Fichtinger, G., and Iordachita, I. "Accuracy study of a robotic system for MRI-guided prostate needle placement". In: *Int J Med Robotics Comput Assist Surg* 9 (2012), pp. 305–316. DOI: 10.1002/rcs.

[109] Seifabadi, R., Gomez, E. E., Aalamifar, F., Fichtinger, G., and Iordachita, I. "Real-time tracking of a bevel-tip needle with varying insertion depth: Toward teleoperated MRI-guided needle steering". In: *IEEE International Conference on Intelligent Robots and Systems*. Tokyo, Japan, 2013, pp. 469–476. ISBN: 9781467363587. DOI: 10.1109/IROS.2013.6696393.

[110] Selig, J. M. "Characterisation of Frenet-Serret and Bishop motions with applications to needle steering". In: *Robotica* 31.6 (2013), pp. 981–992. ISSN: 02635747. DOI: 10.1017/S026357471300026X.

[111] Shahriari, N., Hekman, E., Oudkerk, M., and Misra, S. "Design and evaluation of a computed tomography (CT)-compatible needle insertion device using an electromag-

netic tracking system and CT images". In: *International Journal of Computer Assisted Radiology and Surgery* 10 (2015), pp. 1845–1852. ISSN: 1861-6410. DOI: 10.1007/s11548-015-1176-3.

[112] Shahriari, N., Roesthuis, R. J., Van De Berg, N. J., Van Den Dobbelsteen, J. J., and Misra, S. "Steering an actuated-tip needle in biological tissue: Fusing FBG-sensor data and ultrasound images". In: *Proceedings - IEEE International Conference on Robotics and Automation*. Vol. 2016. Stockholm, Sweden: IEEE, 2016. ISBN: 9781467380263. DOI: 10.1109/ICRA.2016.7487644.

[113] Shi, C., Luo, X., Qi, P., Li, T., Song, S., Najdovski, Z., Fukuda, T., and Ren, H. "Shape Sensing Techniques for Continuum Robots in Minimally Invasive Surgery: A Survey". In: *IEEE Transactions on Biomedical Engineering* 64.8 (2017), pp. 1665–1678. ISSN: 0018-9294. DOI: 10.1109/tbme.2016.2622361.

[114] Simon, D. *Optimal state estimation: Kalman, H, and nonlinear approaches*. 2006. ISBN: 9780470045343. DOI: 10.1002/0470045345.

[115] Smith, W. L., Surry, K. J., Mills, G. R., Downey, D. B., and Fenster, A. "Three-dimensional ultrasound-guided core needle breast biopsy". In: *Ultrasound in Medicine and Biology* 27.8 (2001), pp. 1025–1034. ISSN: 03015629. DOI: 10.1016/S0301-5629(01)00396-9.

[116] Sujit, P. B., Saripalli, S., and Sousa, J. B. "Unmanned aerial vehicle path following: A survey and analysis of algorithms for fixed-wing unmanned aerial vehicles". In: *IEEE Control Sys. Mag.* 34.1 (2014), pp. 42–59. ISSN: 1066033X. DOI: 10.1109/MCS.2013.2287568.

[117] Taffoni, F., Formica, D., Saccomandi, P., Di Pino, G., and Schena, E. "Optical fiber-based MR-compatible sensors for medical applications: An overview". In: *Sensors* 13.10 (2013), pp. 14105–14120. ISSN: 14248220. DOI: 10.3390/s131014105.

[118] Terzano, M., Dini, D., Rodriguez y Baena, F., Spagnoli, A., and Oldfield, M. "An adaptive finite element model for steerable needles". In: *Biomechanics and Modeling in Mechanobiology* 19.5 (2020), pp. 1809–1825. ISSN: 16177940. DOI: 10.1007/s10237-020-01310-x.

[119] Van De Berg, N. J., Van Gerwen, D. J., Dankelman, J., and Van Den Dobbelsteen, J. J. "Design Choices in Needle Steering - A Review". In: *IEEE/ASME Transactions on Mechatronics* 20.5 (2015), pp. 2172–2183. ISSN: 10834435. DOI: 10.1109/TMECH.2014.2365999.

[120] Virdyawan, V., Secoli, R., Matheson, E., Pinzi, M., Watts, T., Galvan, S., and Rodriguez y Baena, F. "Supervisory-Control Robots". In: *Neurosurgical Robotics, Neuromethods*. Ed. by Marcus, H. J. and Payne, C. J. Vol. 162. Springer Science+Business Media, LLC, part of Springer Nature 2021, 2021. Chap. 2, pp. 35–47. ISBN: 9781071609934.

[121] Vitiello, V., Lee, S. L., Cundy, T. P., and Yang, G. Z. "Emerging robotic platforms for minimally invasive surgery". In: *IEEE Reviews in Biomedical Engineering* 6 (2013), pp. 111–126. ISSN: 19373333. DOI: 10.1109/RBME.2012.2236311.

[122] Wan, G., Wei, Z., Gardi, L., Downey, D. B., and Fenster, A. "Brachytherapy needle deflection evaluation and correction". In: *Medical Physics* 32.4 (2005), pp. 902–909. ISSN: 00942405. DOI: 10.1118/1.1871372.

[123] Wang, R., Wang, S., Wang, Y., Tang, C., and Tan, M. "Three-Dimensional Helical Path Following of an Underwater Biomimetic Vehicle-Manipulator System". In: *IEEE Journal of Oceanic Engineering* 43.2 (2018), pp. 391–401. ISSN: 03649059. DOI: 10.1109/JOE.2017.2762498.

[124] Watts, T., Secoli, R., and Rodriguez y Baena, F. "A Mechanics-Based Model for 3-D Steering of Programmable Bevel-Tip Needles". In: *IEEE Transactions on Robotics* 35.2 (2018), pp. 371–386. DOI: 10.1109/TRO.2018.2879584.

[125] Webster, R. J., Kim, J. S., Cowan, N. J., Chirikjian, G., and Okamura, A. M. "Nonholonomic modeling of needle steering". In: *The International Journal of Robotics Research* 25 (2006), pp. 509–525. ISSN: 16107438. DOI: 10.1007/11552246{_}4.

[126] Xu, B. and Ko, S. Y. "3D Feedback control using fuzzy logic for a curvature-controllable steerable bevel-tip needle". In: *Mechatronics* 68.April (2020). ISSN: 09574158. DOI: 10.1016/j.mechatronics.2020.102368.

[127] Xu, R., Yurkewich, A., and Patel, R. V. "Curvature, Torsion, and Force Sensing in Continuum Robots Using Helically Wrapped FBG Sensors". In: *IEEE Robotics and*

Automation Letters 1.2 (2016), pp. 1052–1059. ISSN: 23773766. DOI: 10.1109/LRA.2016.2530867.

[128] Yime, E. *Commanding Maxon Motors EPOS2 Motor Controller from MATLAB*. MATLAB Central File Exchange, 2015.

[129] Zhang, Y., Chen, Z., Zhang, X., Sun, Q., and Sun, M. "A novel control scheme for quadrotor UAV based upon active disturbance rejection control". In: *Aerospace Science and Technology* 79 (2018), pp. 601–609. ISSN: 12709638. DOI: 10.1016/j.ast.2018.06.017.

[130] Zhao, Y., Shen, Y., Bernard, A., Cachard, C., and Liebgott, H. "Evaluation and comparison of current biopsy needle localization and tracking methods using 3D ultrasound". In: *Ultrasonics* 73 (2017), pp. 206–220. ISSN: 0041624X. DOI: 10.1016/j.ultras.2016.09.006.

Appendix - Linear Active Disturbance Rejection Control (LADRC) Stability Analysis

In this section a stability analysis for the LADRC, given in Chapter 6, is presented.

The state equations are given as follows:

$$\begin{aligned} \dot{\boldsymbol{x}}_1 &= b_0\, \boldsymbol{u} + \boldsymbol{x}_2 \\ \dot{\boldsymbol{x}}_2 &= \dot{\boldsymbol{f}} \end{aligned} \tag{7.1}$$

where $\boldsymbol{x}_1 = \boldsymbol{c}_t$, and $\boldsymbol{f} = \dot{\boldsymbol{\omega}}_t$.

In state space matrix form:

$$\begin{aligned} \dot{\boldsymbol{x}} &= \boldsymbol{A}\boldsymbol{x} + \boldsymbol{B}\boldsymbol{u} + \boldsymbol{E}\boldsymbol{f} \\ \boldsymbol{y} &= \boldsymbol{C}\boldsymbol{x}_1 \end{aligned} \tag{7.2}$$

where

$$\dot{\boldsymbol{x}} = \begin{bmatrix} \dot{\boldsymbol{x}}_1 \\ \dot{\boldsymbol{x}}_2 \end{bmatrix}, \quad \boldsymbol{A} = \begin{bmatrix} \boldsymbol{0} & \boldsymbol{I} \\ \boldsymbol{0} & \boldsymbol{0} \end{bmatrix}, \quad \boldsymbol{B} = \begin{bmatrix} b_0\boldsymbol{I} \\ \boldsymbol{0} \end{bmatrix}$$

$$\boldsymbol{x} = \begin{bmatrix} \boldsymbol{x}_1 \\ \boldsymbol{x}_2 \end{bmatrix}, \quad \boldsymbol{C} = \begin{bmatrix} \boldsymbol{I} & \boldsymbol{0} \end{bmatrix}, \quad \boldsymbol{E} = \begin{bmatrix} \boldsymbol{0} \\ \boldsymbol{I} \end{bmatrix}$$

with $\boldsymbol{0}$ being 2×2 matrix including zeros.

Linear ESO:

$$\begin{aligned}\dot{\boldsymbol{\zeta}} &= \boldsymbol{A}\boldsymbol{\zeta} + \boldsymbol{B}\boldsymbol{u} + \boldsymbol{L}(\boldsymbol{y} - \hat{\boldsymbol{y}}) \\ \hat{\boldsymbol{y}} &= \boldsymbol{C}\boldsymbol{\zeta}_1\end{aligned} \tag{7.3}$$

where $\dot{\boldsymbol{\zeta}} = \begin{bmatrix}\dot{\boldsymbol{\zeta}}_1 & \dot{\boldsymbol{\zeta}}_2\end{bmatrix}^T$, $\boldsymbol{\zeta} = \begin{bmatrix}\boldsymbol{\zeta}_1 & \boldsymbol{\zeta}_2\end{bmatrix}^T$, and $\boldsymbol{L} = \begin{bmatrix}\beta_1\boldsymbol{I} & \beta_2\boldsymbol{I}\end{bmatrix}^T$

For stability analysis, a method proposed in [39] is adopted here for the Multi-Input and Multi-Output (MIMO) plant. Defining the errors, $\boldsymbol{e}_1 = \boldsymbol{x}_1 - \boldsymbol{\zeta}_1$ and $e_2 = \boldsymbol{x}_2 - \boldsymbol{\zeta}_2$, and the error dynamics is given as follows:

$$\dot{\boldsymbol{e}} = \boldsymbol{A}\boldsymbol{e} - \boldsymbol{L}\boldsymbol{C}\boldsymbol{e} + \boldsymbol{E}\boldsymbol{f} \tag{7.4}$$

where $\dot{\boldsymbol{e}} = \begin{bmatrix}\dot{\boldsymbol{e}}_1 & \dot{\boldsymbol{e}}_2\end{bmatrix}^T$, and $\boldsymbol{e} = \begin{bmatrix}\boldsymbol{e}_1 & \boldsymbol{e}_2\end{bmatrix}^T$.

Rearranging (7.4):

$$\dot{\boldsymbol{e}} = \boldsymbol{A}_e\boldsymbol{e} + \boldsymbol{E}\boldsymbol{f} \tag{7.5}$$

where $\boldsymbol{A}_e = \boldsymbol{A} - \boldsymbol{L}\boldsymbol{C}$

Therefore, the characteristic polynomial of $\boldsymbol{A}_e$ is given as follows:

$$\begin{aligned}\lambda_c(s) &= |s\boldsymbol{I}^{4\times4} - \boldsymbol{A}_e| \\ &= (s^2 + \beta_1 s + \beta_2)^2\end{aligned} \tag{7.6}$$

When the roots of this polynomial are on the left half-plane and h is bounded, the Extended State Observer (ESO) is Bounded-Input Bounded-Output (BIBO) stable.

The closed-loop LADRC is represented by the state space matrix form as follows:

$$\begin{bmatrix} \dot{\boldsymbol{x}} \\ \dot{\boldsymbol{\zeta}} \end{bmatrix} = \begin{bmatrix} \boldsymbol{A} & \boldsymbol{BF} \\ \boldsymbol{LC} & \boldsymbol{A} - \boldsymbol{LC} + \boldsymbol{BF} \end{bmatrix} \begin{bmatrix} \boldsymbol{x} \\ \boldsymbol{\zeta} \end{bmatrix} + \begin{bmatrix} \boldsymbol{B} & \boldsymbol{E} \\ \boldsymbol{B} & \boldsymbol{0} \end{bmatrix} \begin{bmatrix} \boldsymbol{c}^d \\ \dot{\boldsymbol{f}}\boldsymbol{I} \end{bmatrix} \tag{7.7}$$

where $\boldsymbol{F} = (1/b_0) \begin{bmatrix} -k_p\boldsymbol{I} & -\boldsymbol{I} \end{bmatrix}$.

Then, the roots of the characteristic polynomial are given as $-k_p \cup \{\text{roots of (7.6)}\}$. Assuming that $\dot{\boldsymbol{f}}$ is bounded, and given that the reference $\boldsymbol{c}^d$ is bounded, the system is BIBO stable if all the roots are on the left half-plane.

Obtained Permissions

The obtained permissions are attached to the end of the thesis as seen as of next page.

Design Choices in Needle Steering—A Review

Author: Nick J. van de Berg

Publication: IEEE/ASME Transactions on Mechatronics

Publisher: IEEE

Date: Oct. 2015

Thesis / Dissertation Reuse

The IEEE does not require individuals working on a thesis to obtain a formal reuse license, however, you may print out this statement to be used as a permission grant:

Requirements to be followed when using any portion (e.g., figure, graph, table, or textual material) of an IEEE copyrighted paper in a thesis:

1) In the case of textual material (e.g., using short quotes or referring to the work within these papers) users must give full credit to the original source (author, paper, publication) followed by the IEEE copyright line © 2011 IEEE.
2) In the case of illustrations or tabular material, we require that the copyright line © [Year of original publication] IEEE appear prominently with each reprinted figure and/or table.
3) If a substantial portion of the original paper is to be used, and if you are not the senior author, also obtain the senior author's approval.

Requirements to be followed when using an entire IEEE copyrighted paper in a thesis:

1) The following IEEE copyright/ credit notice should be placed prominently in the references: © [year of original publication] IEEE. Reprinted, with permission, from [author names, paper title, IEEE publication title, and month/year of publication]
2) Only the accepted version of an IEEE copyrighted paper can be used when posting the paper or your thesis on-line.
3) In placing the thesis on the author's university website, please display the following message in a prominent place on the website: In reference to IEEE copyrighted material which is used with permission in this thesis, the IEEE does not endorse any of [university/educational entity's name goes here]'s products or services. Internal or personal use of this material is permitted. If interested in reprinting/republishing IEEE copyrighted material for advertising or promotional purposes or for creating new collective works for resale or redistribution, please go to http://www.ieee.org/publications_standards/publications/rights/rights_link.htm to learn how to obtain a License from RightsLink.

If applicable, University Microfilms and/or ProQuest Library, or the Archives of Canada may supply single copies of the dissertation.

BACK CLOSE WINDOW

SPRINGER NATURE LICENSE
TERMS AND CONDITIONS

Oct 03, 2021

This Agreement between Mr. Abdulhamit Donder ("You") and Springer Nature ("Springer Nature") consists of your license details and the terms and conditions provided by Springer Nature and Copyright Clearance Center.

License Number	5161410310687
License date	Oct 03, 2021
Licensed Content Publisher	Springer Nature
Licensed Content Publication	Springer eBook
Licensed Content Title	Needle Steering and Model-Based Trajectory Planning
Licensed Content Author	S. P. DiMaio, S. E. Salcudean
Licensed Content Date	Jan 1, 2003
Type of Use	Thesis/Dissertation
Requestor type	academic/university or research institute
Format	electronic
Portion	figures/tables/illustrations
Number of figures/tables/illustrations	1
Will you be translating?	no
Circulation/distribution	50000 or greater

Author of this Springer Nature content	no
Title	Full 3D Motion Control for Programmable Bevel Tip Steerable Needles
Institution name	Imperial College London
Expected presentation date	Jan 2022
Portions	Figure 4
Requestor Location	Mr. Abdulhamit Donder Flat 24 Nansen Village, 21 Woodside Aven London, N12 8AQ United Kingdom Attn: Mr. Abdulhamit Donder
Total	0.00 USD

Terms and Conditions

Springer Nature Customer Service Centre GmbH
Terms and Conditions

This agreement sets out the terms and conditions of the licence (the **Licence**) between you and **Springer Nature Customer Service Centre GmbH** (the **Licensor**). By clicking 'accept' and completing the transaction for the material (**Licensed Material**), you also confirm your acceptance of these terms and conditions.

1. Grant of License

1. 1. The Licensor grants you a personal, non-exclusive, non-transferable, world-wide licence to reproduce the Licensed Material for the purpose specified in your order only. Licences are granted for the specific use requested in the order and for no other use, subject to the conditions below.

1. 2. The Licensor warrants that it has, to the best of its knowledge, the rights to license reuse of the Licensed Material. However, you should ensure that the material you are requesting is original to the Licensor and does not carry the copyright of another entity (as credited in the published version).

1. 3. If the credit line on any part of the material you have requested indicates that it was reprinted or adapted with permission from another source, then you should also seek permission from that source to reuse the material.

2. Scope of Licence

2. 1. You may only use the Licensed Content in the manner and to the extent permitted by these Ts&Cs and any applicable laws.

2. 2. A separate licence may be required for any additional use of the Licensed Material, e.g. where a licence has been purchased for print only use, separate permission must be obtained for electronic re-use. Similarly, a licence is only valid in the language selected and does not apply for editions in other languages unless additional translation rights have been granted separately in the licence. Any content owned by third parties are expressly excluded from the licence.

2. 3. Similarly, rights for additional components such as custom editions and derivatives require additional permission and may be subject to an additional fee. Please apply to Journalpermissions@springernature.com/bookpermissions@springernature.com for these rights.

2. 4. Where permission has been granted **free of charge** for material in print, permission may also be granted for any electronic version of that work, provided that the material is incidental to your work as a whole and that the electronic version is essentially equivalent to, or substitutes for, the print version.

2. 5. An alternative scope of licence may apply to signatories of the STM Permissions Guidelines, as amended from time to time.

3. Duration of Licence

3. 1. A licence for is valid from the date of purchase ('Licence Date') at the end of the relevant period in the below table:

Scope of Licence	Duration of Licence
Post on a website	12 months
Presentations	12 months
Books and journals	Lifetime of the edition in the language purchased

4. Acknowledgement

4. 1. The Licensor's permission must be acknowledged next to the Licenced Material in print. In electronic form, this acknowledgement must be visible at the same time as the figures/tables/illustrations or abstract, and must be hyperlinked to the journal/book's homepage. Our required acknowledgement format is in the Appendix below.

5. Restrictions on use

5. 1. Use of the Licensed Material may be permitted for incidental promotional use and minor editing privileges e.g. minor adaptations of single figures, changes of format, colour and/or style where the adaptation is credited as set out in Appendix 1 below. Any other changes including but not limited to, cropping, adapting, omitting material that affect the meaning, intention or moral rights of the author are strictly prohibited.

5. 2. You must not use any Licensed Material as part of any design or trademark.

5. 3. Licensed Material may be used in Open Access Publications (OAP) before publication by Springer Nature, but any Licensed Material must be removed from OAP sites prior to final publication.

6. Ownership of Rights

6. 1. Licensed Material remains the property of either Licensor or the relevant third party and any rights not explicitly granted herein are expressly reserved.

7. Warranty

IN NO EVENT SHALL LICENSOR BE LIABLE TO YOU OR ANY OTHER PARTY OR ANY OTHER PERSON OR FOR ANY SPECIAL, CONSEQUENTIAL, INCIDENTAL OR INDIRECT DAMAGES, HOWEVER CAUSED, ARISING OUT OF OR IN CONNECTION WITH THE DOWNLOADING, VIEWING OR USE OF THE MATERIALS REGARDLESS OF THE FORM OF ACTION, WHETHER FOR BREACH OF CONTRACT, BREACH OF WARRANTY, TORT, NEGLIGENCE, INFRINGEMENT OR OTHERWISE (INCLUDING, WITHOUT LIMITATION, DAMAGES BASED ON LOSS OF PROFITS, DATA, FILES, USE, BUSINESS OPPORTUNITY OR CLAIMS OF THIRD PARTIES), AND
WHETHER OR NOT THE PARTY HAS BEEN ADVISED OF THE POSSIBILITY OF SUCH DAMAGES. THIS LIMITATION SHALL APPLY NOTWITHSTANDING ANY FAILURE OF ESSENTIAL PURPOSE OF ANY LIMITED REMEDY PROVIDED HEREIN.

8. Limitations

8. 1. ***BOOKS ONLY:***Where **'reuse in a dissertation/thesis'** has been selected the following terms apply: Print rights of the final author's accepted manuscript (for clarity, NOT the published version) for up to 100 copies, electronic rights for use only on a personal website or institutional repository as defined by the Sherpa guideline (www.sherpa.ac.uk/romeo/).

8. 2. For content reuse requests that qualify for permission under the STM Permissions Guidelines, which may be updated from time to time, the STM Permissions Guidelines supersede the terms and conditions contained in this licence.

9. Termination and Cancellation

9. 1. Licences will expire after the period shown in Clause 3 (above).

9. 2. Licensee reserves the right to terminate the Licence in the event that payment is not received in full or if there has been a breach of this agreement by you.

Appendix 1 — Acknowledgements:

For Journal Content:
Reprinted by permission from [**the Licensor**]: [**Journal Publisher** (e.g.

Nature/Springer/Palgrave)] [**JOURNAL NAME**] [**REFERENCE CITATION** (Article name, Author(s) Name), [**COPYRIGHT**] (year of publication)

For **Advance Online Publication papers:**
Reprinted by permission from [**the Licensor**]: [**Journal Publisher** (e.g. Nature/Springer/Palgrave)] [**JOURNAL NAME**] [**REFERENCE CITATION** (Article name, Author(s) Name), [**COPYRIGHT**] (year of publication), advance online publication, day month year (doi: 10.1038/sj.[JOURNAL ACRONYM].)

For Adaptations/Translations:
Adapted/Translated by permission from [**the Licensor**]: [**Journal Publisher** (e.g. Nature/Springer/Palgrave)] [**JOURNAL NAME**] [**REFERENCE CITATION** (Article name, Author(s) Name), [**COPYRIGHT**] (year of publication)

Note: For any republication from the British Journal of Cancer, the following credit line style applies:

Reprinted/adapted/translated by permission from [**the Licensor**]: on behalf of Cancer Research UK: : [**Journal Publisher** (e.g. Nature/Springer/Palgrave)] [**JOURNAL NAME**] [**REFERENCE CITATION** (Article name, Author(s) Name), [**COPYRIGHT]** (year of publication)

For **Advance Online Publication** papers:
Reprinted by permission from The [**the Licensor**]: on behalf of Cancer Research UK: [**Journal Publisher** (e.g. Nature/Springer/Palgrave)] [**JOURNAL NAME**] [**REFERENCE CITATION** (Article name, Author(s) Name), [**COPYRIGHT**] (year of publication), advance online publication, day month year (doi: 10.1038/sj.[JOURNAL ACRONYM])

For Book content:
Reprinted/adapted by permission from [**the Licensor**]: [**Book Publisher** (e.g. Palgrave Macmillan, Springer etc) [**Book Title**] by [**Book author**(s)] [**COPYRIGHT**] (year of publication)

Other Conditions:

Version 1.3

Questions? customercare@copyright.com or +1-855-239-3415 (toll free in the US) or +1-978-646-2777.

ELSEVIER LICENSE
TERMS AND CONDITIONS

Oct 03, 2021

This Agreement between Mr. Abdulhamit Donder ("You") and Elsevier ("Elsevier") consists of your license details and the terms and conditions provided by Elsevier and Copyright Clearance Center.

License Number	5161401331018
License date	Oct 03, 2021
Licensed Content Publisher	Elsevier
Licensed Content Publication	Academic Radiology
Licensed Content Title	System for Robotically Assisted Prostate Biopsy and Therapy with Intraoperative CT Guidance
Licensed Content Author	Gabor Fichtinger,Theodore L DeWeese,Alexandru Patriciu,Attila Tanacs,Dumitru Mazilu,James H Anderson,Ken Masamune,Russell H Taylor,Dan Stoianovici
Licensed Content Date	Jan 1, 2002
Licensed Content Volume	9
Licensed Content Issue	1
Licensed Content Pages	15
Start Page	60
End Page	74
Type of Use	reuse in a thesis/dissertation

Portion	figures/tables/illustrations
Number of figures/tables/illustrations	1
Format	electronic
Are you the author of this Elsevier article?	No
Will you be translating?	No
Title	Full 3D Motion Control for Programmable Bevel Tip Steerable Needles
Institution name	Imperial College London
Expected presentation date	Jan 2022
Portions	Figure 7
Requestor Location	Mr. Abdulhamit Donder Room 708, Mechanical Engineering Dept. Imperial College London South Kensington Campus London, SW7 2AZ United Kingdom Attn: Mr. Abdulhamit Donder
Publisher Tax ID	GB 494 6272 12
Total	0.00 USD
Terms and Conditions	

INTRODUCTION

1. The publisher for this copyrighted material is Elsevier. By clicking "accept" in connection with completing this licensing transaction, you agree that the following terms and conditions apply to this transaction (along with the Billing and Payment terms and conditions established by Copyright Clearance Center, Inc. ("CCC"), at the time that you opened your Rightslink account and that are available at any time at http://myaccount.copyright.com).

GENERAL TERMS

2. Elsevier hereby grants you permission to reproduce the aforementioned material subject to the terms and conditions indicated.

3. Acknowledgement: If any part of the material to be used (for example, figures) has appeared in our publication with credit or acknowledgement to another source, permission must also be sought from that source. If such permission is not obtained then that material may not be included in your publication/copies. Suitable acknowledgement to the source must be made, either as a footnote or in a reference list at the end of your publication, as follows:

"Reprinted from Publication title, Vol /edition number, Author(s), Title of article / title of chapter, Pages No., Copyright (Year), with permission from Elsevier [OR APPLICABLE SOCIETY COPYRIGHT OWNER]." Also Lancet special credit - "Reprinted from The Lancet, Vol. number, Author(s), Title of article, Pages No., Copyright (Year), with permission from Elsevier."

4. Reproduction of this material is confined to the purpose and/or media for which permission is hereby given.

5. Altering/Modifying Material: Not Permitted. However figures and illustrations may be altered/adapted minimally to serve your work. Any other abbreviations, additions, deletions and/or any other alterations shall be made only with prior written authorization of Elsevier Ltd. (Please contact Elsevier's permissions helpdesk here). No modifications can be made to any Lancet figures/tables and they must be reproduced in full.

6. If the permission fee for the requested use of our material is waived in this instance, please be advised that your future requests for Elsevier materials may attract a fee.

7. Reservation of Rights: Publisher reserves all rights not specifically granted in the combination of (i) the license details provided by you and accepted in the course of this licensing transaction, (ii) these terms and conditions and (iii) CCC's Billing and Payment terms and conditions.

8. License Contingent Upon Payment: While you may exercise the rights licensed immediately upon issuance of the license at the end of the licensing process for the transaction, provided that you have disclosed complete and accurate details of your proposed use, no license is finally effective unless and until full payment is received from you (either by publisher or by CCC) as provided in CCC's Billing and Payment terms and conditions. If full payment is not received on a timely basis, then any license preliminarily granted shall be deemed automatically revoked and shall be void as if never granted. Further, in the event that you breach any of these terms and conditions or any of CCC's Billing and Payment terms and conditions, the license is automatically revoked and shall be void as if never granted. Use of materials as described in a revoked license, as well as any use of the materials beyond the scope of an unrevoked license, may constitute copyright infringement and publisher reserves the right to take any and all action to protect its copyright in the materials.

9. Warranties: Publisher makes no representations or warranties with respect to the licensed material.

10. Indemnity: You hereby indemnify and agree to hold harmless publisher and CCC, and their respective officers, directors, employees and agents, from and against any and all claims arising out of your use of the licensed material other than as specifically authorized pursuant to this license.

11. No Transfer of License: This license is personal to you and may not be sublicensed, assigned, or transferred by you to any other person without publisher's written permission.

12. No Amendment Except in Writing: This license may not be amended except in a writing signed by both parties (or, in the case of publisher, by CCC on publisher's behalf).

13. Objection to Contrary Terms: Publisher hereby objects to any terms contained in any purchase order, acknowledgment, check endorsement or other writing prepared by you, which terms are inconsistent with these terms and conditions or CCC's Billing and Payment terms and conditions. These terms and conditions, together with CCC's Billing and Payment terms and conditions (which are incorporated herein), comprise the entire agreement between you and publisher (and CCC) concerning this licensing transaction. In the event of any conflict between your obligations established by these terms and conditions and those established by CCC's Billing and Payment terms and conditions, these terms and conditions shall control.

14. Revocation: Elsevier or Copyright Clearance Center may deny the permissions described in this License at their sole discretion, for any reason or no reason, with a full refund payable to you. Notice of such denial will be made using the contact information provided by you. Failure to receive such notice will not alter or invalidate the denial. In no event will Elsevier or Copyright Clearance Center be responsible or liable for any costs, expenses or damage incurred by you as a result of a denial of your permission request, other than a refund of the amount(s) paid by you to Elsevier and/or Copyright Clearance Center for denied permissions.

LIMITED LICENSE

The following terms and conditions apply only to specific license types:

15. **Translation**: This permission is granted for non-exclusive world **English** rights only unless your license was granted for translation rights. If you licensed translation rights you may only translate this content into the languages you requested. A professional translator must perform all translations and reproduce the content word for word preserving the integrity of the article.

16. **Posting licensed content on any Website**: The following terms and conditions apply as follows: Licensing material from an Elsevier journal: All content posted to the web site must maintain the copyright information line on the bottom of each image; A hyper-text must be included to the Homepage of the journal from which you are licensing at http://www.sciencedirect.com/science/journal/xxxxx or the Elsevier homepage for books at http://www.elsevier.com; Central Storage: This license does not include permission for a scanned version of the material to be stored in a central repository such as that provided by Heron/XanEdu.

Licensing material from an Elsevier book: A hyper-text link must be included to the Elsevier homepage at http://www.elsevier.com . All content posted to the web site must maintain the copyright information line on the bottom of each image.

Posting licensed content on Electronic reserve: In addition to the above the following clauses are applicable: The web site must be password-protected and made available only to bona fide students registered on a relevant course. This permission is granted for 1 year only. You may obtain a new license for future website posting.

17. **For journal authors:** the following clauses are applicable in addition to the above:

Preprints:

A preprint is an author's own write-up of research results and analysis, it has not been peer-reviewed, nor has it had any other value added to it by a publisher (such as formatting, copyright, technical enhancement etc.).

Authors can share their preprints anywhere at any time. Preprints should not be added to or enhanced in any way in order to appear more like, or to substitute for, the final versions of articles however authors can update their preprints on arXiv or RePEc with their Accepted Author Manuscript (see below).

If accepted for publication, we encourage authors to link from the preprint to their formal publication via its DOI. Millions of researchers have access to the formal publications on ScienceDirect, and so links will help users to find, access, cite and use the best available version. Please note that Cell Press, The Lancet and some society-owned have different preprint policies. Information on these policies is available on the journal homepage.

Accepted Author Manuscripts: An accepted author manuscript is the manuscript of an article that has been accepted for publication and which typically includes author-incorporated changes suggested during submission, peer review and editor-author communications.

Authors can share their accepted author manuscript:

- immediately
    - via their non-commercial person homepage or blog
    - by updating a preprint in arXiv or RePEc with the accepted manuscript
    - via their research institute or institutional repository for internal institutional uses or as part of an invitation-only research collaboration work-group
    - directly by providing copies to their students or to research collaborators for their personal use
    - for private scholarly sharing as part of an invitation-only work group on commercial sites with which Elsevier has an agreement
- After the embargo period
    - via non-commercial hosting platforms such as their institutional repository
    - via commercial sites with which Elsevier has an agreement

In all cases accepted manuscripts should:

- link to the formal publication via its DOI
- bear a CC-BY-NC-ND license - this is easy to do
- if aggregated with other manuscripts, for example in a repository or other site, be shared in alignment with our hosting policy not be added to or enhanced in any way to appear more like, or to substitute for, the published journal article.

Published journal article (JPA): A published journal article (PJA) is the definitive final record of published research that appears or will appear in the journal and embodies all value-adding publishing activities including peer review co-ordination, copy-editing, formatting, (if relevant) pagination and online enrichment.

Policies for sharing publishing journal articles differ for subscription and gold open access articles:

Subscription Articles: If you are an author, please share a link to your article rather than the full-text. Millions of researchers have access to the formal publications on ScienceDirect, and so links will help your users to find, access, cite, and use the best available version.

Theses and dissertations which contain embedded PJAs as part of the formal submission can be posted publicly by the awarding institution with DOI links back to the formal publications on ScienceDirect.

If you are affiliated with a library that subscribes to ScienceDirect you have additional private sharing rights for others' research accessed under that agreement. This includes use for classroom teaching and internal training at the institution (including use in course packs and courseware programs), and inclusion of the article for grant funding purposes.

Gold Open Access Articles: May be shared according to the author-selected end-user license and should contain a CrossMark logo, the end user license, and a DOI link to the formal publication on ScienceDirect.

Please refer to Elsevier's posting policy for further information.

18. **For book authors** the following clauses are applicable in addition to the above: Authors are permitted to place a brief summary of their work online only. You are not allowed to download and post the published electronic version of your chapter, nor may you scan the printed edition to create an electronic version. **Posting to a repository:** Authors are permitted to post a summary of their chapter only in their institution's repository.

19. **Thesis/Dissertation**: If your license is for use in a thesis/dissertation your thesis may be submitted to your institution in either print or electronic form. Should your thesis be published commercially, please reapply for permission. These requirements include permission for the Library and Archives of Canada to supply single copies, on demand, of the complete thesis and include permission for Proquest/UMI to supply single copies, on demand, of the complete thesis. Should your thesis be published commercially, please reapply for permission. Theses and dissertations which contain embedded PJAs as part of the formal submission can be posted publicly by the awarding institution with DOI links back to the formal publications on ScienceDirect.

Elsevier Open Access Terms and Conditions

You can publish open access with Elsevier in hundreds of open access journals or in nearly 2000 established subscription journals that support open access publishing. Permitted third party re-use of these open access articles is defined by the author's choice of Creative Commons user license. See our open access license policy for more information.

Terms & Conditions applicable to all Open Access articles published with Elsevier:

Any reuse of the article must not represent the author as endorsing the adaptation of the article nor should the article be modified in such a way as to damage the author's honour or reputation. If any changes have been made, such changes must be clearly indicated.

The author(s) must be appropriately credited and we ask that you include the end user license and a DOI link to the formal publication on ScienceDirect.

If any part of the material to be used (for example, figures) has appeared in our publication with credit or acknowledgement to another source it is the responsibility of the user to ensure their reuse complies with the terms and conditions determined by the rights holder.

Additional Terms & Conditions applicable to each Creative Commons user license:

CC BY: The CC-BY license allows users to copy, to create extracts, abstracts and new works from the Article, to alter and revise the Article and to make commercial use of the Article (including reuse and/or resale of the Article by commercial entities), provided the user gives appropriate credit (with a link to the formal publication through the relevant DOI), provides a link to the license, indicates if changes were made and the licensor is not represented as endorsing the use made of the work. The full details of the license are available at http://creativecommons.org/licenses/by/4.0.

CC BY NC SA: The CC BY-NC-SA license allows users to copy, to create extracts, abstracts and new works from the Article, to alter and revise the Article, provided this is not done for commercial purposes, and that the user gives appropriate credit (with a link to the formal publication through the relevant DOI), provides a link to the license, indicates if changes were made and the licensor is not represented as endorsing the use made of the